HZDR-067

VOR 1.000.000 JAHREN
Homo erectus

VOR 250.000 JAHREN
Neandertaler

VOR 150.000 JAHREN
Homo sapiens sapiens

VOR 40.000 JAHREN
Älteste Höhlenmalerei Europas

Ende der letzten Kaltzeit
VOR 12.000 JAHREN

Beginn der Schriftkultur
VOR 5.000 JAHREN

Zeitwende
0

1206
erste urkundliche Erwähnung
von Dresden

1694
August der Starke
Kurfürst von Sachsen

1896
Entdeckung der Radioaktivität

Radioaktivität wieder
auf natürlichem Niveau
1.000.000

Morlocks und Eloi bevölkern die Erde
(nach dem Roman „The Time Machine")
802.701

100.000
Plutonium (Pu-239) ist zerfallen

Pu

Am

Americium (Am-241) ist zerfallen
5.500

2.364
USS Enterprise D startet

2.200
Cäsium (Cs-137) ist zerfallen

Cs

Anzahl der AKWs weltweit: ~450
2015

Wiedervereinigung
1990

Erstes Kernkraftwerk
in Deutschland
1960

ANNUAL REPORT 2015

INSTITUTE OF RESOURCE ECOLOGY

HZDR

HELMHOLTZ
ZENTRUM DRESDEN
ROSSENDORF

Annual Report 2015

Institute of Resource Ecology

Editor:
Prof. Dr. Thorsten Stumpf

Executive editors:
Dr. Harald Foerstendorf
Dr. Frank Bok
Dr. Anke Richter

HZDR

HELMHOLTZ
ZENTRUM DRESDEN
ROSSENDORF

Impressum

Contact

Helmholtz-Zentrum Dresden-Rossendorf e.V.
Institute of Resource Ecology

Postal Address	*Address for visitors*
P.O. Box 51 01 19	Bautzner Landstraße 400
D-01314 Dresden	D-01328 Dresden
Germany	Germany

Phone: +49 (0) 351 260 3210
Fax: +49 (0) 351 260 3553
e-mail: contact.resourceecology@hzdr.de
http://www.hzdr.de/FWO

This report is also available at http://www.hzdr.de/FWO

Cover picture

A 'Flock of Happenings' – initiated by the artist Florian Dombois – took place around the Postplatz, Dresden, on May 30th, 2015. Under the title "Inverse", forth and backward running time in natural sciences was investigated by scientists from the Institute of Resource Ecology who developed a 200 meter 'time rope' reflecting a time period of one million years projecting into the past as well as into the future. This fixed period will be necessary to store high level radioactive waste until its activity has reached the natural level (for more details see p. 86).

Cover picture created by H. Foerstendorf using a photo taken by Florian Dombois
(Photo "1960" by Sebastian Suchanek).

Preface

THE INSTITUTE OF RESOURCE ECOLOGY (IRE) is one of the eight institutes of the Helmholtz-Zentrum Dresden-Rossendorf (HZDR). The research activities are mainly integrated into the program "Nuclear Waste Management, Safety and Radiation Research (NUSAFE)" of the Helmholtz Association (HGF) and focused on the topics "Safety of Nuclear Waste Disposal" and "Safety Research for Nuclear Reactors".

Additionally, various activities have been started investigating chemical and environmental aspects of processing and recycling of strategic metals, namely rare earth elements. These activities are located in the HGF program "Energy Efficiency, Materials and Resources (EMR)". Thus, all scientific work of the IRE belongs to the research field "Energy" of the HGF.

The research objective is the protection of humans and the environment from hazards caused by pollutants resulting from technical processes that produce energy and raw materials. Treating technology and ecology as a unity is the major scientific challenge in assuring the safety of technical processes and gaining their public acceptance. We investigate the ecological risks ensued by radioactive and non-radioactive metals in the context of nuclear waste disposal, the production of energy in nuclear power plants and in processes along the value chain of metalliferous raw materials. A common goal is to generate better understanding about the dominating processes essential for metal mobilization and immobilization on the molecular level by using advanced spectroscopic methods. This in turn enables us to assess the macroscopic phenomena, including models, codes and data for predictive calculations, which determine the transport and distribution of contaminants in the environment.

The extraordinary broadness of research topics and activities is illustrated below by some selected highlights:

In 2015, the institute inherited the Materials Science Hutch of the Rossendorf Beamline. Therefore, twice the amount of precious beamtime is now available for nuclear waste research. In addition, the second hutch offers the possibility to expand the portfolio of techniques to improve our knowledge about the (bio-geo-) chemistry of radionuclides. A heavy-duty 6-circle goniometer was adapted to be used for surface-sensitive X-ray scattering techniques like Crystal Truncation Rod (CTR) and Resonant Anomalous X-Ray Reflectivity (RAXR) (see p. 27, 28), and first successful tests were made towards the establishment of a Johann-type emission spectrometer for high-resolution X-ray Absorption Near Edge Structure (XANES), X-ray Emission Spectrometry (XES), and Resonant Inelastic X-ray Scattering (RIXS) measurements (see p. 23).

Scientifically, work performed at the Rossendorf Beamline covers basic chemistry of actinides (the formation pathway of the U_{38} polyoxo cluster), mineral-water interface reactions (sorption and redox processes of the fission product Tc) as well as solid state chemistry (the structure of phosphates as potential waste forms for long-lived actinides). A DFG project on the interfacial redox reactions of Sn was completed, demonstrating that migration of this fission product is strongly retarded by the corrosion minerals, which form on the surface of waste containers under a wide variety of geochemical conditions; therefore, Sn can be deleted from the list of key risk drivers relevant for nuclear waste repositories (see p. 31).

In the framework of the European project NURESAFE, the HZDR reactor dynamics code DYN3D was coupled with the Computational Fluid Dynamics code TRIO_U, developed at CEA France, in order to replace DYN3D's one-dimensional hydraulic part with a full three-dimensional description of the coolant flow in the reactor core at higher spatial resolution. The availability of this new code system opens now the possibility to study the influence of three-dimensional coolant flow in the reactor core on the progress of hypothetical accidents and helps to reduce too conservative assumptions for such analyses (see p. 62).

The Reactive Transport division develops into the field of reactive transport modelling by aligning simulated results to radiotracer studies on columns obtained in our controlled area. In three different models the ternary interactions of ^{64}Cu with organic ligands (glutamic acid, the microbial siderophore DFOB and the herbicide MCPA) and model substrates (covellite, artificial soil and kaolinite) are investigated in pH dependent studies (see p. 35, 34). Surface complexation modelling by means of PHREEQC and its coupling to COMSOL Multiphysics allows for future interpretation of (3D+t) data sets obtained by GeoPET.

The iron oxydizing microorganism *Gallionella ferruginea* causes precipitation of iron oxyhydrates. At nearly neutral pH and aerobic conditions a high sorption capacity for uranium(VI) and neptunium(V) was detected. However, XANES studies did not reveal a reduction to uranium(IV) or neptunium(IV).

In order to understand heavy metal binding to bacterial surfaces, calorimetric experiments have been performed that demonstrate the cation-specific stability of oligomeric states of proteins isolated from bacterial surface layers. Such investigations lay the foundation for the use and optimization of such biomaterials in applications ranging from industrial surface modification to actinide bioremediation exploiting stable self-assembling biomolecular structures (see p. 53).

The division Chemistry of the f-Elements, established in June 2014, focuses on the fundamental research on the physical/chemical properties of actinides. The associated research highlight is the elucidation of colloidal actinide species, demonstrating their remarkable stability under aqueous conditions relevant to nuclear waste repositories. These outcomes would further serve as important information for a reliable safety assessment on nuclear waste repositories and geological disposal.

Time-resolved laser-induced fluorescence spectroscopy of both Eu(III) and Cm(III) revealed the local environment of such trivalent heavy metals in monazites. Nearly ideal solid solutions could be identified pointing at very favourable long-term stability. These scarcely soluble phosphate materials are currently intensively discussed to incorporate and thus immobilize radionuclides. They can be applied for the conditioning of waste matrices and may also be a component of the geotechnical barrier in the surrounding of a deep geological waste repository (see p. 15).

Beside these highlights, we obtained many other new scientific results in the past year, which are presented in this annual report. Furthermore,

65 original papers were published in peer-reviewed international scientific journals. In the year 2015, more than 130 scientists, technicians, and students working on their Ph.D., diploma, master, or bachelor thesis, were employed at the Institute of Resource Ecology. Thereof, 26 Ph.D. students worked at the institute in 2015. Promotion of young scientists is an important requirement to ensure the competence and further scientific excellence in future times.

About the research at IRE in the field of nuclear waste disposal, a film was produced in 2015. The English version is attached in form of a CD. Hopefully, you will enjoy this kind overview.

I would like to thank the visitors, German and international ones, for their interest in our research and for their participation in the institute seminars. We would also like to thank our scientific collaborators and the visiting scientists for coming to Dresden/Rossendorf in 2015 to share their knowledge and experience with us. We will continue to strongly encourage the collaborations and visits by scientists in the future. Special thanks are due to the executive board of the HZDR, the Ministry of Science and Arts of the Free State Saxony (SMWK), the Federal Ministry of Education and Research (BMBF), the Federal Ministry of Economics and Energy (BMWi), the Deutsche Forschungsgemeinschaft (DFG), the European Commission, and other organizations for their support.

Prof. Dr. Thorsten Stumpf
Director of the
Institute of Resource Ecology

Contents

PART III: DEVELOPING THERMODYNAMIC DATABASES

PART IV: LONG-LIVED RADIONUCLIDES IN BIOLOGICAL SYSTEMS

PART V: NUCLEAR REACTOR SAFETY RESEARCH

PUBLICATIONS

SCIENTIFIC ACTIVITIES

PERSONNEL

ACKNOWLEDGEMENTS

INDEX OF AUTHORS

The Chemistry of

LONG-LIVED RADIONUCLIDES

.

Spectroscopic studies on the interaction of europium(III) and curium(III) with components of the human mucosa

C. Wilke, A. Barkleit

To evaluate the health risks of lanthanides (Ln) and radiotoxic actinides (An) in case of ingestion accidents etc., investigations into the chemical reactions of these metals in the human gastrointestinal tract are necessary. Our previous study revealed that mucin, an important part of the protective mucosa layer in the digestive system, shows a strong interaction with Eu(III). Based on these results, the present study focuses on the components of this glycoprotein and identified N-acetylneuraminic acid (NANA) as the dominant binding carbohydrate of mucin. TRLFS measurements suggest the formation of a 1 : 1 complex with log β of 3.2 ± 0.1 for Eu(III) and 3.3 ± 0.1 for Cm(III), respectively.

Ln and An have no essential roles in human biochemistry. However, through different processes such as nuclear accidents, these heavy metals could be potentially released into the environment where they could be further incorporated eventually into the human gastrointestinal tract through oral ingestion. The digestive system is covered by a thick, visco-elastic mucosa membrane, which is a protective barrier to pathogens and toxic substances. The protective response in mucosa relies largely on the glycoprotein mucin. Mucin is a large glycoprotein, which is highly glycosylated consisting of ~80% carbohydrates primarily N-acetylgalactosamine (GalNac), N-acetylglucosamine (GlcNac), fucose, galactose and N-acetylneuraminic acid (NANA) [1]. A previous spectroscopic screening identified mucin as an important binding partner with Eu(III) [2]. Based on this previous results, the present study focuses on this protein and its components to investigate its binding behavior with Eu(III) and Cm(III) as representatives of Ln(III) and An(III), respectively.

EXPERIMENTAL. The carbohydrates listed above were dissolved and mixed with Eu(III) or Cm(III) solution to give a metal : ligand ratio of 1 : 100 at pH 7. Another sample containing 1 mg/mL mucin was also prepared. TRLFS measurements of the prepared samples were carried out at room temperature [3] as functions of carbohydrate concentration and pH. For the concentration variation series, pH was fixed at 4.5 and the carbohydrate concentration was varied from 0.02 to 10 mM (1 : 2 to 1 : 1000 metal-to-ligand ratio). For the pH variation series, the carbohydrate concentration was fixed at 1 mM and the pH was varied from 2 to 10. The metal concentration in both series was 1×10^{-5} M and 3×10^{-7} M for Eu(III) and Cm(III), respectively. A solution of 2.5 M NaCl was used to adjust the ionic strength at 0.1 M.

RESULTS. Figure 1 shows the TRLFS spectra of Eu(III) with a carbohydrate or mucin, indicating that all the tested carbohydrates show a complex formation with Eu(III), but with a minor strength compared to mucin. The results also suggest that, among the tested carbohydrates, NANA shows the strongest interaction with Eu(III). Therefore, further experiments focused on this carbohydrate. Figure 2 shows the TRLFS results for the concentration variation series of Eu(III) (left) and Cm(III) (right). Both results exhibit the same increasing trend in luminescence intensity as an increase in NANA concentration. The stability constants
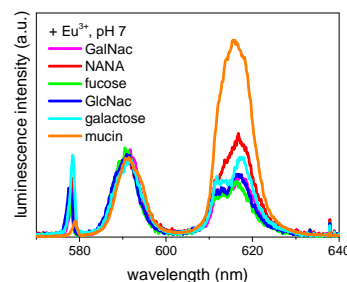
Fig. 1: Luminescence spectra of Eu(III) (1×10^{-5} M) with selected carbohydrates and mucin at room temperature.
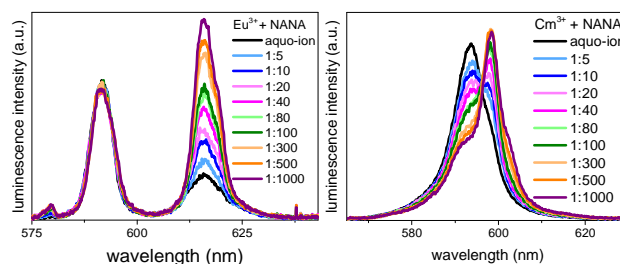
Fig. 2: Luminescence spectra of Eu(III) (1×10^{-5} M, left) and Cm(III) (3×10^{-7} M, right) as a function of NANA concentration at room temperature, pH = 4.5.
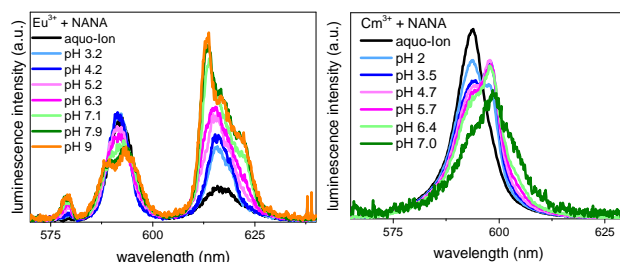
Fig. 3: Luminescence spectra of Eu(III) (1×10^{-5} M, left) and Cm(III) (3×10^{-7} M, right) as a function of pH at room temperature. NANA concentration was fixed at 10^{-3} M.

(log β) were calculated to be 3.2 ± 0.1 and 3.3 ± 0.1 for Eu(III) and Cm(III), respectively, assuming a 1 : 1 stoichiometry.

Figure 3 shows the TRLFS results for the pH variation series. The results for Eu(III) (left) showed a gradual increase in complex formation with increasing pH until pH 7, where a remarkable change in intensity of the F_2 peak is observed. The luminescence spectra for Cm(III) (right) indicated a red shift as an increase of pH with a slight peak splitting above pH = 5. The decrease in peak intensity above pH = 7 suggests the hydrolysis of Cm(III).

[1] Bansil, R. et al. (2006) *Curr. Opin. Colloid Intferface Sci.* **11**, 164–170.
[2] Wilke, C. et al. (2015) this report, p.12.
[3] Moll, H. et al. (2007) *BioMetals* **21**, 219–228.

A spectroscopic screening of the chemical speciation of europium(III) in gastro-intestinal tract: the intestine

C. Wilke, A. Barkleit

To evaluate the health risks of lanthanides (Ln) and radiotoxic actinides (An), investigations into the chemical reactions of these metals in the human gastrointestinal tract are necessary. In order to identify the dominant binding partners (i.e. counter ions and/or ligands) of An/Ln in the gastrointestinal tract, a spectroscopic screening was performed by Time-Resolved Laser-induced Fluorescence Spectroscopy (TRLFS) using artificial digestive juices containing Eu(III), a representative of Ln(III) and An(III). In the intestine, Eu(III) show a strong complexation especially with organic substances of the pancreatic and bile juice like the protein mucin.

In general, Ln and An have no essential roles in human biochemistry. However, through different processes such as nuclear accidents, these heavy metals could be potentially released into the environment where they could be incorporated into the food chain and eventually into the human body through oral ingestion. Because of the chemical toxicity and radiotoxicity of An, it is important to understand their chemical and biological behavior *in vivo*. This study focuses particularly on the biochemical behavior of An/Ln in the gastrointestinal tract. As an initial step, the first spectroscopic screening was performed to find possible binding partners of An(III)/Ln(III) in the gastrointestinal system. The body fluids of mouth and stomach (saliva and gastric juice) have been already investigated [1]. Hence, this report focuses on the intestine containing the pancreatic and bile juice.

EXPERIMENTAL. The *in vitro* digestion model used in this study was developed by Oomen *et al.* [1]. This is the basis of an international unified bioaccessibility protocol [2]. Based on the human physiology, this gastrointestinal model simulates the mouth, stomach and small intestine. The compositions of the investigated digestive juices are summarized in Tab. 1. An aqueous solution of 1×10^{-5} M EuCl$_3$·6H$_2$O was mixed with either a single constituent or different mixtures of pancreatic and bile juice. TRLFS measurements of the prepared samples were carried out at room (25 °C) and body temperatures (37 °C).

Tab. 1: Composition of the synthetic pancreatic and bile juice [1, 2].

	Pancreatic Juice	Bile Juice
Inorganic substances	234.0 mM NaCl	180 mM NaCl
	133.5 mM NaHCO$_3$	137.7 mM NaHCO$_3$
	15.1 mM KCl	10.1 mM KCl
	1.4 mM CaCl$_2$	1.5 mM CaCl$_2$
	1.2 mM KH$_2$PO$_4$	
	0.5 mM MgCl$_2$	
Organic substances	3.3 mM urea	8.3 mM urea
Proteins	3 mg/mL mucin	6 mg/mL bile
	3 mg/mL pancreatin	1.8 mg/mL BSA
	1 mg/mL BSA	
	0.5 mg/mL lipase	
pH	7.4 ± 0.2	8.0 ± 0.2

RESULTS. *Pancreatic juice:* The results for the pancreastic juice are shown in Fig. 1. These results suggest that, although carbonate, phosphate and calcium are the major inorganic binding partners of Eu(III), the organic substances, especially proteins, show a stronger complexation toward Eu(III) than the inorganic substances. To identify dominant organic binding partners with Eu(III), additional TRLFS measurements were performed with different protein mixtures. As shown in Fig. 1 (right), the resultant TRLFS spectra are all comparable except the mixture without mucin which shows a significant decrease in luminescence intensity at around 613 nm. This suggests that the protein mucin has a strong influence on complexation with Eu(III).
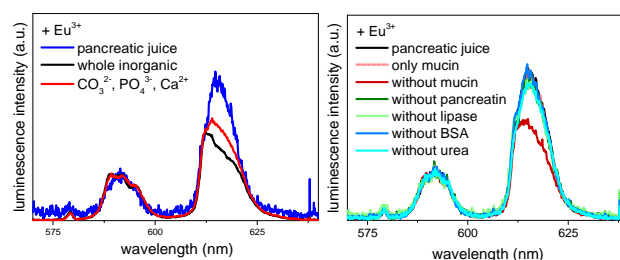
Fig. 1: Luminescence spectra of Eu(III) in different mixtures of the synthetic pancreatic juice with inorganic components (left) and proteins/urea (right) at pH 7.4 and at room temperature.

Bile juice: Figure 2 shows the luminescence spectra of Eu(III) with inorganic (left) and organic substances (right) of the bile juice, suggesting that carbonate, BSA and bile are the major contributors to the Eu(III) complexation. Because of the chemical complexity of bile consisting of bile salts, alcohols, heavy metals, metabolic products etc. [3], no specific binding partner could be identified at this stage.
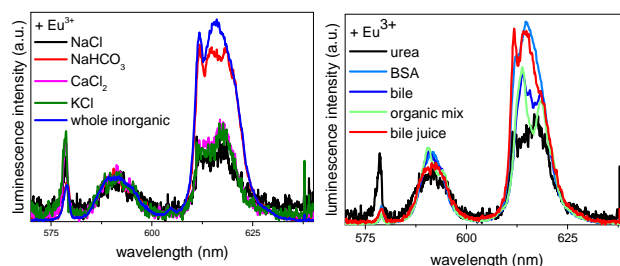
Fig. 2: Luminescence spectra of Eu(III) with compounds of the synthetic bile juice at pH 8.0 and at room temperature with inorganic (left) and organic (right) compounds.

[1] Wilke, C. et al. (2015) *Report HZDR-059*, p.16.
[2] Oomen, A. G. et al. (2003) *Arch. Environ. Contam. Toxicol.* **44**, 281–287.
[3] Wragg, J. et al. (2009) British Geological Survey Open Report.
[4] Hofmann, A. F. (1994) in: *Physiology of the Gastrointestinal tract*, p.1555–1571, Raven Press.

Interaction of europium and curium with alpha-amylase

A. Barkleit, A. Heller[1]

[1]Institute for Zoology, Molecular Cell Physiology and Endocrinology, Technische Universität Dresden, Dresden, Germany

Time-resolved laser-induced fluorescence spectroscopy (TRLFS) revealed that Eu(III) and Cm(III) form two dominant species with the protein α-amylase (Amy): one with the coordination of a single carboxylate group of the protein and the other with three coordinating carboxylate groups.

The protein α-amylase (α-1,4-glucan-4-glucanhydrolase; EC 3.2.1.1.) catalyzes the hydrolysis of the α-1,4-glycosidic linkages of polysaccharides, such as starch or glycogen. It is also one of the major enzymes in salivary and pancreatic secretions of mammals. In case of oral ingestion of radioactive substances the transport and metabolism of the radionuclides could be potentially influenced by the interaction with proteins. The aim of this study is to elucidate the interactions of trivalent actinides (An(III)) and lanthanides (Ln(III)) with α-amylase, one of the major proteins in salivary and pancreatic secretions.

EXPERIMENTAL. Porcine pancreatic α-amylase (Amy, 55 kDa, 50 negatively charged residues (COO^-), 48 positively charged residues (NH_3^+), 1 Ca^{2+} [1]) was purchased from Sigma. The pK_a values of Amy were previously reported [2]. The complex formation with Eu(III) and Cm(III) were determined spectrophotometrically. TRLFS measurements were performed according to the conditions already described [3].

RESULTS. The luminescence spectra of Eu(III) in aqueous solutions of Amy show an increase of the peak intensity associated with the hypersensitive $^5D_0 \rightarrow {}^7F_2$ transition at 610–625 nm with increasing Amy concentration (Fig. 1) or pH. Furthermore, the $^7F_2$ peak was split significantly and the $^7F_1$ peak at 585 – 600 nm became asymmetric with increasing Amy concentration or pH. These spectral changes indicate a strong complex formation between Eu(III) and Amy. The results from time-resolved measurements indicated a bi-exponential decay, suggesting that at least two luminescent species are formed. The luminescence lifetimes lengthened with increasing Amy concentration or pH. This indicates the replacement of water molecules in the first coordination sphere of Eu(III) with the coordinative functional groups of Amy.

The obtained TRLFS data were fitted according to the procedure described in [4] to calculate the conditional stability constants for Eu(III)-Amy complexes. Two independent Eu(III)-Amy species could be identified (Tab. 1). The stability constant for the first Eu(III)-Amy species was calculated to be $\log \beta_{11} = 4.8 \pm 0.4$, suggesting the presence of a "Eu(III) : L = 1 : 1" complex where L is the binding carboxylate group of Amy. The stability constant for the second species was calculated to be $\log \beta_{13} = 12.0 \pm 0.4$, indicating the formation of a "1 : 3" complex. Attempts to fit the data by assuming the "1 : 2" complex did not provide reasonable results.

The spectrophotometric titrations of Cm(III) with Amy revealed that the luminescence spectra of Cm(III) were red-shifted with increasing the Amy concentration (Fig. 2) or the pH. The time-resolved spectra of Cm(III) also indicated a bi-exponential decay, suggesting the presence of at least two independent species in the system. The stability con-
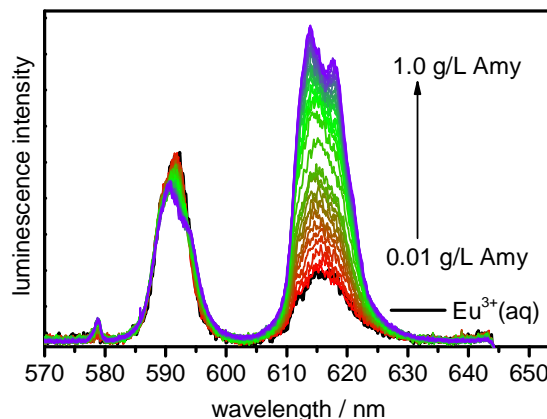
Fig. 1: Spectrophotometric titration of Eu(III) as a function of Amy concentration at pH = 5.5.

Tab. 1: Conditional stability constants of M(III)-Amy complexes at $I = 0.1$ M (NaCl). The $\log \beta^\circ$ values were obtained by extrapolating the $\log \beta^{0.1}$ values to infinite dilution applying SIT.

Species	$\log \beta^{0.1}$	$\log \beta^\bullet$
Eu(Amy-COO)$^{2+}$	4.83 ± 0.43	5.49
Eu(Amy-COO)$_3$	12.04 ± 0.36	13.31
Cm(Amy-COO)$^{2+}$	4.76 ± 0.11	5.42
Cm(Amy-COO)$_3$	12.13 ± 0.12	13.40
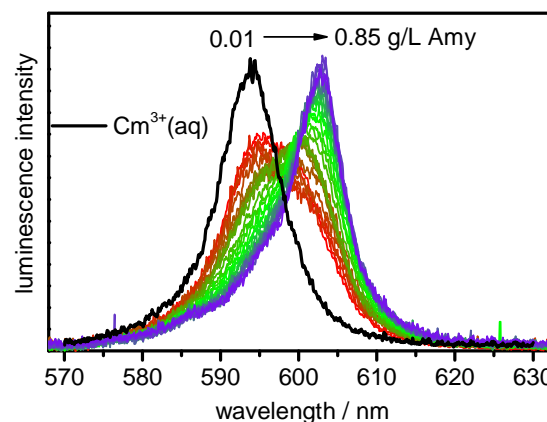
Fig. 2: Spectrophotometric titration of Cm(III) as a function of Amy concentration at pH = 5.5.

stants of the Cm(III)-Amy complexes calculated from the TRLFS spectra were similar to those obtained for the Eu(III)-Amy complexes within the range of error (Tab. 1).

[1] Artimo, P. et al. (2012) *Nucl. Acids Res* **40(W1)**, W597–W603.
[2] Barkleit, A. et al. (2014) *Report HZDR-048*, p. 20.
[3] Heller, A. et al. (2012) *Dalton Trans.* **41**, 13969–13983.
[4] Barkleit, A. et al. (2013) *Inorg. Chim. Acta* **394**, 535–541.

The local structure of Sm and Tb in $Sm_{1-x}Tb_xPO_4$

M. J. Lozano-Rodriguez, J. Heuser,[1] S. Neumeier,[1] A. C. Scheinost

[1]Institute of Energy and Climate Research, Nuclear Waste Management and Reactor Safety (IEK-6), Forschungszentrum Jülich GmbH, Jülich, Germany

Among the phosphates considered as waste forms for long-lived radionuclides, monazite stands out because of its low solubility, slow dissolution rate and high chemical flexibility to incorporate actinide elements such as Am and Cm. EXAFS was carried out to evaluate the local structure of the $Sm_{1-x}Tb_xPO_4$ solid-solution between the Sm endmember with monazite and the Tb endmember with xenotime structure.

EXPERIMENTAL. Solid solutions of $Sm_{1-x}Tb_xPO_4$ with x = 0 –1 were synthesized using wet-chemical precipitation at room temperature similar to [1]. EXAFS measurements were carried out at ROBL (ESRF, Grenoble). Spectra were collected at the Sm L_3 (6716 eV) and Tb L_3 (7514 eV) edges, using a He cryostat (15 K), in fluorescence or transmission mode depending on concentration. The experimental spectra were Fourier-transformed using a Hanning window across 2.0–9.0 $Å^{-1}$ for Tb and Sm. Monazite and xenotime models as reported earlier [2] were used for the data refinement, which was done with WinXAS [3].

RESULTS. Figure 1 shows the Sm L_3 edge spectra of the $Sm_{1-x}Tb_xPO_4$ solid solution samples up to x = 0.8, and for comparison the Tb L_3 edge spectrum of x = 1.00. The samples from x = 0 to x = 0.75 show little changes of the local environment around Sm. Only for x = 0.8 the spectrum changes significantly and becomes more similar to the spectrum of pure $TbPO_4$ with xenotime structure shown on the bottom. In a first step, the spectra were analyzed by ITFA (Iterative Transformation Factor Analysis) [4]. All seven Sm L_3 edge spectra including the Tb L_3 edge spectrum could be reconstructed by two principal components (red lines in Fig. 1), demonstrating that only two different local environments around the Sm(Tb) centers are present, corre-

Tab. 1: Fraction of monazite and xenotime determined by ITFA.

x	Monazite	Xenotime
0.00	1.00	0.00
0.35	0.99	0.01
0.50	0.96	0.04
0.65	0.96	0.04
0.70	0.92	0.08
0.75	0.93	0.07
0.80	0.44	0.56
1.00	0.00	1.00

sponding to the cation centers in monazite and xenotime. Using the spectra of x = 0.00 and x = 1.00 as pure endmembers, the fractions of these two endmembers in the solid solution series could be determined with iterative target test (Tab. 1). In confirmation of the visual observation, the local structure is up to x = 0.75 dominated by monazite, while x = 0.80 is a 50 : 50 mix of both monazite and xenotime local structures.

In a second step, the spectra were analysed by shell fit. Up to x = 0.75, the spectra can be fit with the monazite model, while for x > 0.75, the xenotime model had to be used [2]. The Sm–O bond length remains unchanged up to x = 0.65 at 2.34 Å corresponding to 9-coordinated monazite, and then decreases with x linearly to the bond length of 8-coordinated xenotime, i.e. 2.37 Å (Fig. 2). For the nearest and next-nearest Sm/Tb neighbours (note that Sm and Tb backscattering functions cannot be distinguished by EXAFS), the distances remain unchanged up to x = 0.75 at the values of monazite, and then change abruptly to the distances of monazite.

Fig. 1: Sm-L_3 edge EXAFS spectra for the $Sm_{1-x}Tb_xPO_4$ solid solutions up to x = 0.8, compared to the Tb-L_3 edge spectrum for x = 1.00 (Fourier transform magnitude; k^3-weighted EXAFS as insert). Black lines are the experimental spectra, red lines their reconstruction with two principal components.
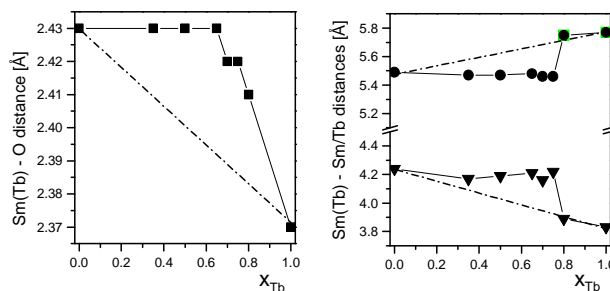
Fig. 2: EXAFS shell fit-determined distances between Sm(Tb) and O (left side) and between Sm(Tb) and nearest and next-nearest (Sm/Tb) neighbors (right side) of the $Sm_{1-x}Tb_xPO_4$ series as a function of x.

CONCLUSIONS. The high flexibility of the monazite structure to host foreign cations is demonstrated by the fact, that monazite remains the dominant phase up to x = 0.75. At x = 0.8, the Sm local environment changes to the xenotime local structure in a rather abrupt step. These results demonstrate that monazite can host a very high percentage of foreign cations, which makes it such a promising candidate for the safe enclosure of long-lived actinides.

[1] Boakye, E. E. et al. (2008) *J. Am. Ceram. Soc.* **91**, 3841–3849.
[2] Ni, Y. et al. (1995) *Am. Mineral.* **80**, 21–26.
[3] Ressler, T. (1998) *J. Synchrotron Radiat.* **5**, 118–122.
[4] Rossberg, A. et al. (2003) *Anal. Bioanal. Chem.* **376**, 631–638.

Eu^{3+} and Cm^{3+} incorporation in hydrated LnPO$_4$·nH$_2$O (Ln = La, Gd) rhabdophane

N. Huittinen, Y. Arinicheva,[1] J. Holthausen,[1] S. Neumeier,[1] T. Stumpf

[1]Forschungszentrum Jülich, Jülich, Germany

Europium and curium incorporation in LaPO$_4$ and GdPO$_4$ rhabdophane was investigated with site-selective TRLFS. The trivalent dopants are incorporated on two distinct low-symmetry sites within the solid structure. Based on recorded lifetime data, "species 1" is associated with 0.7 H$_2$O molecules within the hydrated rhabdophane structure, while "species 2" is substituted for an anhydrous host cation site within the solid.

Rhabdophane phases with the generic formula LnPO$_4$·nH$_2$O are low temperature precursors in the synthesis of monazites (LnPO$_4$) and they can be formed as secondary phases upon dissolution of monazites. Rhabdophane has long been considered to crystallize in the hexagonal crystal structure [1], until a recent re-examination of the structure revealed its crystallization in the monoclinic C2 space group [2]. In the present study Eu^{3+} and Cm^{3+} incorporation in LaPO$_4$ and GdPO$_4$ rhabdophane has been studied using site-selective time resolved laser fluorescence spectroscopy (TRLFS) to shed light on the local environment of the incorporated dopant and the site symmetry of the rhabdophane host.

EXPERIMENTAL. For the synthesis of rhabdophane, La(NO$_3$)$_3$ or Gd(NO$_3$)$_3$ was dissolved in deionized water to a concentration of 0.3–0.5 M. An 85% aqueous solution of H$_3$PO$_4$ was slowly added to the solution, causing precipitation of LnPO$_4$·nH$_2$O doped with 500 ppm Eu^{3+} or 50 ppm Cm^{3+}. The site-selective TRLFS investigations were performed with a pulsed Nd:YAG-pumped tunable dye laser set-up. Excitation spectra, emission spectra and luminescence lifetimes of the rhabdophane phases were collected at cryogenic temperatures (~10 K).

RESULTS. The Eu^{3+} excitation spectrum of GdPO$_4$ rhabdophane reveals the presence of two poorly resolved Eu^{3+} species within the solid structure (Fig. 1). The minor species (species 1) contributes to approximately 30% to the total Eu^{3+} speciation as determined by Gaussian fitting of the collected spectrum.
Emission spectra of the two individual Eu^{3+} species show a maximum 3-fold splitting of the ^{7}F$_1$ band (Fig. 2, top), indicating that Eu^{3+} is incorporated on low symmetry sites, in

Fig. 2: Emission spectra of Eu^{3+} doped GdPO$_4$ rhabdophane (top) and Cm^{3+} doped LaPO$_4$ rhabdophane (bottom).

accordance with the refined monoclinic crystal structure of rhabdophane [2]. By examining Cm^{3+} doped LaPO$_4$ rhabdophane, two clearly separated Cm^{3+} species with emission peak maxima around 600.80 nm and 608.20 nm were obtained (Fig 2, bottom).
The clearly separated Cm^{3+} species allowed for an unambiguous fitting of collected luminescence data (data not shown), with luminescence lifetimes of 475 µs (species 1) and 1750 µs (species 2), respectively. The shorter lifetime corresponds to 0.7 H$_2$O molecules around the Cm^{3+} dopant. This is in perfect agreement with the refined monoclinic LnPO$_4$·0.67H$_2$O rhabdophane structure found in [2]. The longer lifetime of 1750 µs indicates that species 2 is incorporated on a fully dehydrated rhabdophane site. Whether this incorporation occurs on a host lattice site that is not in contact with water molecules in the hydrated rhabdophane structure or in an anhydrous LaPO$_4$ rhabdophane structure formed upon dehydration of LnPO$_4$·0.67H$_2$O [2], however, cannot be deduced from the present data.

[1] Mooney, R. C. L. (1950) *Acta Cryst.* **3**, 337–340.
[2] Mesbah, A. et al. (2014) *Cryst. Growth Des.* **14**, 5090–5098.

Fig. 1: Excitation spectrum of Eu^{3+}doped GdPO$_4$ rhabdophane. Species 1 cies 1 and 2 (dashed blue and green peaks, respectively) were obtained by Gaussian fitting. The black, dashed line represents the sum spectrum of the Gaussian fits.

Synthesis of tetravalent actinide chlorides – Versatile compounds for actinide chemistry

J. März

Anhydrous actinide tetrachlorides (AnCl$_4$) were synthesized under mild conditions to provide versatile compounds for actinide chemistry. They enable a direct access to actinide complexes with organic and inorganic ligands.

Anaerobic conditions expected in nuclear waste repositories could potentially stabilize actinides with lower oxidation states, such as tetravalent (e.g. U(IV) and Np(IV)). Hence, there would be a potential demand for fundamental understanding of the interaction of tetravalent actinides (An(IV)) with organic- and inorganic compounds under anaerobic conditions. In general, anhydrous metal chlorides serve as suitable starting materials for many types of reactions under such conditions. They could also prevent An(IV) from their strong hydrolysis to ensure sufficiently strong complex formation with ligands particularly in organic solvents. Common ways to obtain actinide tetrachlorides, AnCl$_4$, require highly toxic materials such as CCl$_4$ or chlorine gas with harsh conditions and long reaction times [1]. Given the radio- and chemotoxicity of actinides especially trans-uranium (TRU) elements, the synthetic rout must be as simple and safe as possible to produce an adequate amount of AnCl$_4$. This report demonstrates one promising and simple synthetic route to obtain AnCl$_4$ under mild conditions.

GENERAL EXPERIMENTAL NOTES. All preparations and syntheses were performed under N$_2$ atmosphere with a standard Schlenk technique. Solvents used in this study were commercially purchased and used without any further purification.

RESULTS AND DISCUSSION. Lighter actinides such as thorium (Th as ^{232}Th) and uranium (U as ^{238}U) are fairly low radioactive and, hence, they are well suited for optimizing the reaction conditions and for confirming the An(IV) complex formation. Other advantages for Th(IV) are its redox stability and possible use in NMR spectroscopy for structure characterization. A convenient way to obtain anhydrous ThCl$_4$ is shown in Scheme 1. First, the thorium nitrate hydrate is converted to the chloride hydrate. The resultant chloride hydrate is then reacted with a drying agent, trimethylsilyl chloride (Me$_3$SiCl), in dimethoxyethane (DME) resulting in the formation of the precursor complex ThCl$_4$(DME)$_2$. Alternatively, thionyl chloride could be used to remove the hydrate waters, although it requires a longer reaction time [1].

The access to anhydrous U(IV) tetrachloride is easier. The most common starting material of UO$_2$(NO$_3$)$_2$·6H$_2$O can be converted to UCl$_4$ in one step process by using hexachloropropene (C$_3$Cl$_6$) which acts an effective chlorinating, reducing and drying agent simultaneously (Scheme 2) [2].

$$UO_2(NO_3)_2 \cdot 6\,H_2O \xrightarrow[\substack{- C_3Cl_4O \\ - NO_x \\ - Cl_2}]{\substack{C_3Cl_6 \\ 200°C,\ 20h}} UCl_4$$
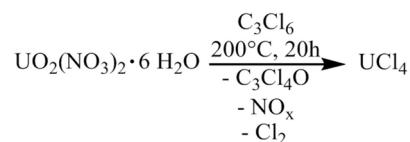
Scheme 2: Synthetic route for UCl$_4$.

In order to exploit the benefits of hexachloropropene for the NpCl$_4$ synthesis, the starting compound, NpO$_2$, is first dissolved and oxidized in a concentrated nitric acid to yield the hydrated neptunium(VI) nitrate, NpO$_2$(NO$_3$)$_2$·nH$_2$O [3]. The second step is then, in the same manner applied to the synthesis of UCl$_4$, the direct conversion to NpCl$_4$ (Scheme 3) [2, 3].

$$NpO_2 + HNO_3 \xrightarrow[]{\substack{H_2O \\ 100°C,\ 4h}} NpO_2(NO_3)_2 \cdot n\,H_2O$$

$$NpO_2(NO_3)_2 \cdot n\,H_2O \xrightarrow[\substack{- C_3Cl_4O \\ - NO_x \\ - Cl_2}]{\substack{C_3Cl_6 \\ 200°C,\ 18h}} NpCl_4$$
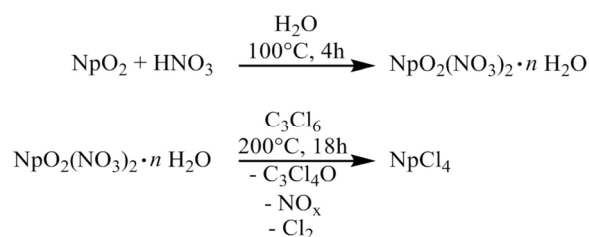
Scheme 3: Synthetic route for NpCl$_4$.

The obtained anhydrous AnCl$_4$ compounds can be employed as effective and versatile precursor materials for, for instance, salt metathesis to synthesize organometallic complexes. A wide range of actinide complexes are planned to be synthesized from the obtained AnCl$_4$ in the institute in the near future.

[1] Cantat, T. et al. (2010) *Chem. Commun.* **46**, 919–921.
[2] Patel, D. (2015) *New J. Chem.* **39**, 7559–7562.
[3] Lindqvist-Reis, P. et al. (2013) *Dalton Trans.* **42**, 15275–15279.

$$Th(NO_3)_4 \cdot 5\,H_2O + HCl\ (12\ M) \xrightarrow[\substack{- NO_x}]{\substack{H_2O \\ 100°C,\ 6h}} ThCl_4 \cdot 4\,H_2O$$

$$ThCl_4 \cdot 4\,H_2O + xs\ Me_3SiCl \xrightarrow[\substack{- HCl \\ - (Me_3Si)_2O}]{\substack{DME \\ 90°C,\ 12h}} ThCl_4(DME)_2$$

Scheme 1: Synthetic route for ThCl$_4$(DME)$_2$.

Formation process of the poly-oxo cluster U$_{38}$

C. Hennig, C. Falaise,[1] C. Volkringer,[1] T. Loiseau[1]

[1]Unité de Catalyse et Chimie du Solide, Université de Lille, Villeneuve d'Ascq, France

Recently, a new poly-oxo cluster with 38 uranium atoms, U$_{38}$O$_{56}$Cl$_{18}$(THF)$_8$(bz)$_{24}$·8THF, (U$_{38}$), has been synthesized [1]. We studied *ex situ* the reaction kinetics of this complex [2].

EXPERIMENTAL. The formation process of the nanocluster U$_{38}$O$_{56}$Cl$_{18}$(THF)$_8$(bz)$_{24}$·8THF, U$_{38}$, was studied by analysing the liquid and solid species of the solvothermal syntheses after different reaction times (0.5–12 h). The reaction was carried out under autogenous pressure at 130 °C, using an initial mixture of UCl$_4$, (100 mg, 0.26 mmol), benzoic acid (Hbz, 500 mg, 4.1 mmol), anhydrous tetrahydrofuran (THF, 4 mL, 49 mmol), and deionized water (30 mL, 1.7 mmol).

RESULTS. The solid products were recovered from the solvent by centrifugation and then analysed with powder XRD (Fig. 1). First crystalline phases appear after 1.5 h, but are after 2.5 h replaced by an amorphous phase. Poorly crystallized uranium dioxide, UO$_2$, forms after 3 h, and remains the prevalent solid up to 7 h. The first Bragg peaks of U$_{38}$ appear after 4 h. The XRD patterns for t = 5, 6, and 7 h indicate a mixture of UO$_2$ and U$_{38}$ with increasing Bragg peak intensities of U$_{38}$ at the expense of those of UO$_2$. After 8 h reaction time only the Bragg peaks of U$_{38}$ remain.
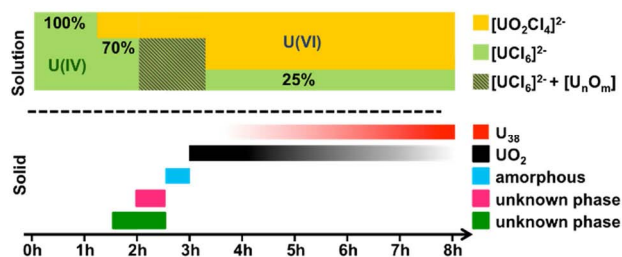
Fig. 1: Schematic representation of solid phases, solution species and the formation of the poly-oxo cluster U$_{38}$ as a function of reaction time.

Whereas only tetravalent uranium was observed in the solid phases, the solution species examined by U L$_3$-edge XANES show a change from pure U(IV) within the first 0.5 h to 75% U(VI) at reaction time > 4 h (Fig. 2). The structure of the initial solution species up to 0.5 h reaction time was determined from EXAFS spectra (Fig. 3) as UCl$_x$(THF)$_y^{4-x}$ with x = 4.6 and y = 3.4. The occurrence of U(VI) at t ≥ 1 h can be identified by EXAFS through the appearance of a peak at $R+\Delta$ ~1.3, resulting from the uranyl ion, UO$_2^{2+}$ (noted O^{yl} in Fig. 3). The peak splitting between U–O und U–Cl (noted O and Cl in Fig. 3) becomes more pronounced with time. The hexavalent uranium species identified by EXAFS data analysis is [(UO$_2$)Cl$_x$(THF)$_y$]$^{2-x}$ with x + y between 4 and 6. At reaction time ≥ 2 h a U–U peak appears with a distance of 3.84 Å, revealing the presence of polynuclear species such as [U$_6$O$_8$] or higher [U$_n$O$_m$] moieties, which co-exist with the monomers in solution. SEM images show that UO$_2$ spheres are embedded in octahedrally shaped U$_{38}$ crystals. This suggests that the UO$_2$ aggregates act as a "reservoir" of tetravalent uranium for the nucleation and crystal growth of the final cluster U$_{38}$ through a dissolution-crystallization process. The growth of U$_{38}$ crystals at the expense of the UO$_2$ is most likely forced
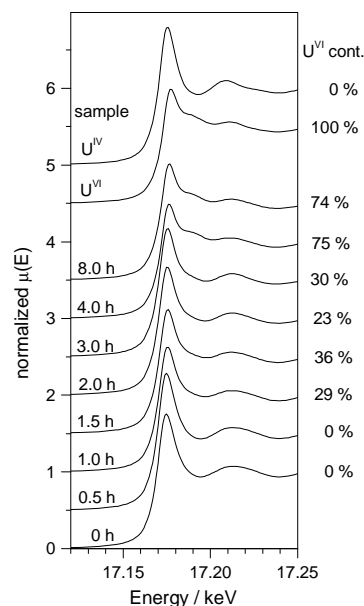
Fig. 2: U L$_3$-XANES spectra of the surnatant solutions. Reference spectra of U(VI) and U(IV) are taken from [3].
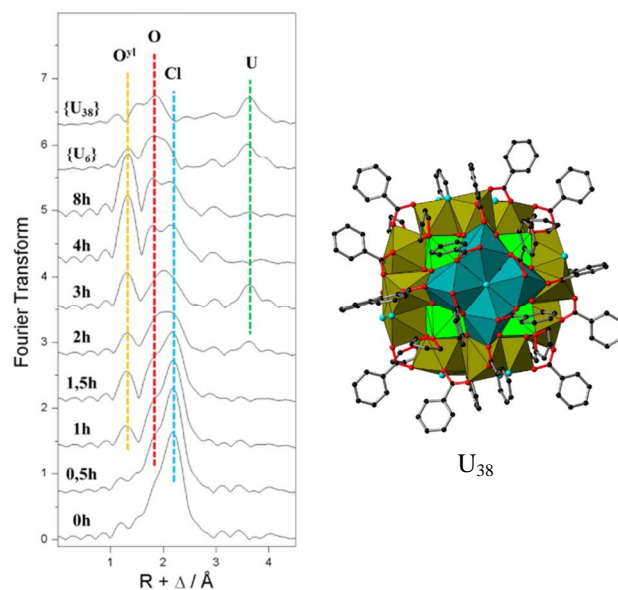
Fig. 3: The nanocluster U$_{38}$O$_{56}$Cl$_{18}$(THF)$_8$(bz)$_{24}$·8THF, U$_{38}$, (right) from [1] and U L$_3$-EXAFS spectra of the supernatant solutions (left). References (top) are the solid compounds U$_{38}$ and U$_6$.

by the liquid-diffusion path of reactive U(IV) solution species. It seems that the formation of U$_{38}$ takes place when the redox balance is shifted from U^{IV}/U^{VI} 70 : 30 to 25 : 75. At t = 3 h, about 15 mol-% of the uranium is precipitated in the form of UO$_2$. The final yield of U$_{38}$ after 12 h is 36%, showing that 64 mol-% of the uranium remains in solution, with about 16 mol-% as tetravalent uranium. It indicates that about half of the tetravalent uranium cations consumed for the formation of U$_{38}$ is derived from the solution, whereas the second half is derived from the dissolution of the UO$_2$ precipitate.

[1] Falaise, C. et al. (2013) *J. Am. Chem. Soc.* **135**, 15678–15681.
[2] Falaise, C. et al. (2015) *Chem. Eur. J.* **135**, 16654–16664.
[3] Hennig, C. et al. (2010) *Dalton Trans.* **39**, 3744–3750.

Uranium interaction with DNA and sugar phosphates

A. Rossberg, S. Tsushima, A. Barkleit, K. Fahmy

We used self-organizing maps (SOM) in order to resolve the molecular structure of U(VI) complexes with DNA and sugar phosphates (SP) in aqueous solution at different pH.

In the past few years strong efforts were undertaken to explain the high carcinogenicity of uranium. Recent findings show that the non-radiological genotoxic effects are more relevant than the radiological effects, hence, the understanding of the chemical U-DNA interaction on the molecular scale is mandatory for the development of possible medical treatments in the future. While up to now no direct structural investigation method like EXAFS was used, electrospray ionization Fourier transform ion cyclotron resonance mass spectrometry (ESI-FTICR-MS) with oligonucleotides points out that the most probable uranium binding site is the phosphodiester backbone [1], in line with ^{1}H NMR investigations [2].

EXPERIMENTAL. Four aqueous solutions were prepared with U(VI) concentrations of 5.0 mM, 2.5 mM, 2.0 mM and 1.0 mM while the U : DNA ratio was 1 : 4, 1 : 4, 1 : 5 and 1 : 5 at pH 6.0, 6.1, 6.2 and at pH 6.3, respectively. Half of the volume of each sample was irradiated with an UV-lamp. U-L_{III} EXAFS spectra were collected for both the irradiated and the non-irradiated samples at 15 K (pH 6.0 & 6.1) and at room temperature (RT) (pH 6.2 & 6.3). In addition, aqueous solutions of U(VI) with glucose-1-phosphate, glucose-6-phosphate, fructose-6-phosphate and fructose-1,6-diphosphate were prepared in the pH range from 2 to 6 with U(VI) and SP concentrations 1 mM to 5 mM and 5 mM to 50 mM, respectively, and measured at RT in fluorescence mode. In total the data comprises 8 DNA and 22 SP samples, the latter serving as references for the U-DNA backbone interaction.

RESULTS. SOM, as a kind of artificial intelligence, enables visualization of high dimensional data spaces on a 2-dimensional grid [3]. We have further developed this method to allow the un-mixing of the spectral mixtures into the fractions and spectra of the components by using all available information (spectra, pH, concentrations, etc.) [4]. Clusters of three components (31, 32, 33) where detected as shown in Fig. 1. The SP (9–30) form various mixtures between all three components (C1, C2, C3), while the DNA samples (1–8) contain mostly C1 and C3. The isolated spectra of the components are shown in Fig. 2. The spectrum of C1 is in agreement with meta-autunite, which has four monodentately coordinated phosphate groups. Therefore, one can conclude that the PO$_4$ groups of the DNA backbone coordinate the U(VI) also in a monodentate mode. The fraction of C1 varies for the SP samples between ~0.25–0.50 and for the DNA samples between ~0.25–0.38, which corresponds to 1–2 and 1–1.5 coordinated phosphate groups, respectively. The presence of 1 : 1 and 1 : 2 U(VI)–SP complexes is in line with speciation calculations [5, 6]. For the 1 : 1 and the 1 : 2 SP and DNA complex the measured average U–O$_{eq}$ distance of 2.39 Å and 2.33 Å confirms a 5- and a 4-fold coordination as observed for U(VI)-hydrate (2.41 Å) and meta-autunite (2.27 Å), hence the 1 : 1 and 1 : 2 complexes are coordinated by four and two H$_2$O/OH molecules, respectively. While the distance of the coordinated
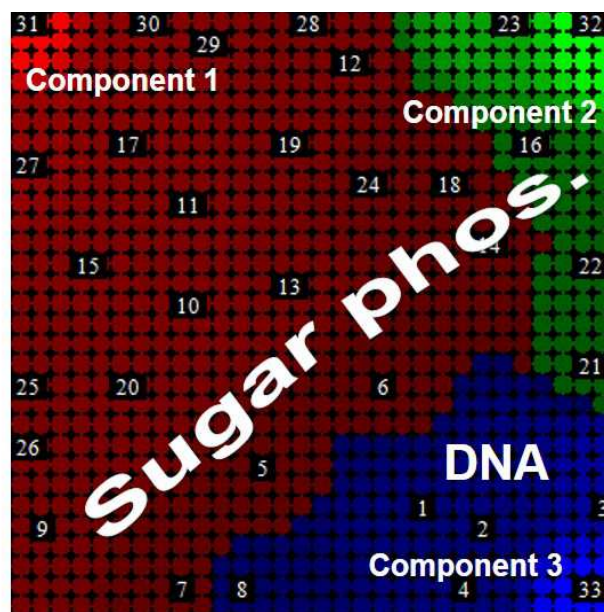
Fig. 1: Clustering of components. The color of a component becomes predominant when the fraction of the component exceeds 1/3. Numbers correspond to the samples (1–30) and to the components (31–33).
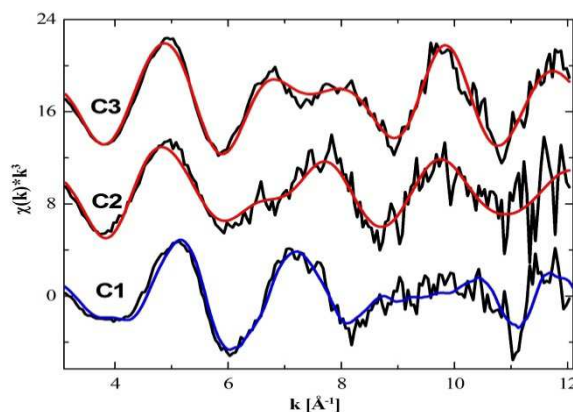
Fig. 2: U L$_{III}$ EXAFS of SOM isolated components (black), meta-autunite (blue), shell fit (red).

PO$_4$ group does not change with the coordination number of the complexes, obviously the different average U–O$_{eq}$ distances result from the coordinated H$_2$O/OH molecules. This explains the appearance of C2 and C3 which represent H$_2$O/OH molecules in a U–O$_{eq}$ distance of 2.47 Å (1 : 1 complex) and 2.38 Å (1 : 2 complex), respectively. In the presence of U(VI) the illumination with UV-light can lead to DNA strand breaks [7, 8], but no spectral changes are observed. If we assume that a DNA strand break would cause spectral changes, then we can conclude that no DNA strand break took place at all or that the break already happened in the presence of U(VI) without UV illumination, which would be in line with [2].

[1] Wu, Q. et al. (1996) *J. Mass Spectrom.* **31**, 669–675.
[2] Yazzi, M. et al. (2003) *Chem. Res. Toxicol.* **16**, 524–530.
[3] Kohonen, T. (1982) *Biol. Cybern.* **43**, 59–69.
[4] Domaschke, K. et al. (2014) *ESANN proceedings,* 277–282.
[5] Koban, A. et al. (2004) *Radiochim. Acta.* **92**, 903–908.
[6] Koban, A. et al. (2003) *Radiochim. Acta.* **91**, 393–396.
[7] Wilson, J. et al. (2015) *J. Appl. Toxicol.* **35**, 338–349.
[8] Nielsen, P. E. et al. (1992) *J. Am. Chem. Soc.* **114**, 4967–4975.

Complexation of a modified calix[4]arene L1 with uranium(VI)

A. Bauer, K. Schmeide

Functionalized calix[4]arenes act as organic extraction agents for metal cations. They can be used in rare earth production to eliminate the radioactive actinides from the ore concentrates and to separate the rare earth elements. For a better understanding of process mechanisms the interaction between modified calix[4]arenes and actinides / lanthanides have to be characterized. This report presents spectroscopic studies on the interaction between a modified calix[4]arene L1 and uranium(VI).

Calixarenes are macrocyclic compounds with a chalice-like structure synthesized by a base induced condensation of para substituted phenols and formaldehyde [1]. The para-substitution forms the so-called upper rim and determines the solubility of the molecule. The hydroxyl groups are at the lower rim and serve either directly as complexation site or can be further functionalized to adjust the selectivity of the calixarene [1].

EXPERIMENTAL. The complexation of U(VI) with a modified calix[4]arene called L1 was examined by UV-vis and luminescence spectroscopy. Acetonitrile was used as solvent due to its photochemical stability and the absence of absorption and fluorescence properties within the excitation wavelength.

12.5 µM L1 in acetonitrile at constant ionic strength (0.01 M NaClO$_4$) was titrated with a 25 µM uranyl nitrate solution. UV-vis spectra in the range of 250–400 nm and 400–700 nm were recorded.

The Job´s Plot was used to determine the reactant stoichiometry [2]. For this, stock solutions of L1 (100 µM) and uranyl nitrate (100 µM) in acetonitrile were used. A series of samples was prepared where the L1 plus uranyl nitrate molar concentration was kept constant while the molar ratio varies. The absorbance was determined at 525 nm.

During titration of 50 µM uranyl nitrate in acetonitrile with 100 µM L1 was applied time-resolved laser fluorescence spectroscopy (TRLFS). The emission spectra were recorded at an excitation wavelength of 266 nm.

RESULTS. The absorption spectrum of L1 shows typical peaks at 280 nm and 320 nm. With increasing uranyl nitrate concentration the peak at 280 nm decreases and is disappeared at equilibrium (Fig. 1). The formed uranyl L1 complex shows absorption maxima at 318 nm and 360 nm. A further peak occurs at 525 nm (not shown). Job´s Plot (Fig. 2) and the titration experiment indicate a 1:2 (UO$_2^{2+}$/L1) complex formation.

The luminescence spectra (Fig. 3) show the emission of uranyl nitrate in acetonitrile at different L1 concentrations. The luminescence spectra show maxima at 467, 486, 507, 529, and 552 nm. With increasing concentration of L1 the luminescence signal is weakened and a shift of emission maxima is observed. The observed luminescence lifetime ranges from 26.2 ± 0.3 µs to 3.34 ± 0.06 µs. An emission maximum of L1 at 465 nm is induced at an excitation wavelength of 360 nm. The formed metal ligand complex shows no emission spectrum. The results indicate the suitability of the modified calix[4]arene for the extraction of U(VI). Further determinations of extraction properties as function of pH, ligand to metal ratio, extraction time and influence of
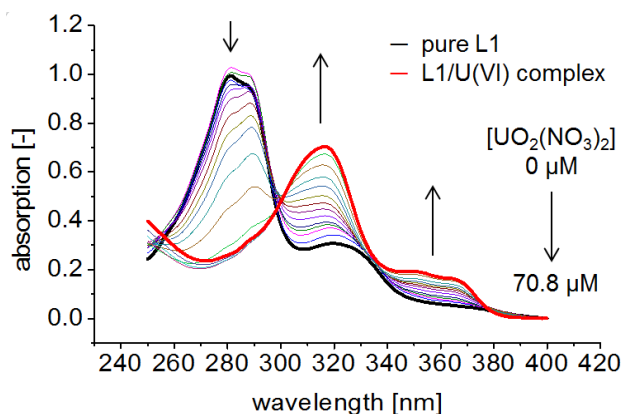
Fig. 1: UV visible spectra of 12.5 µM L1 in acetonitrile at different UO$_2$(NO$_3$)$_2$ concentrations; $I = 0.01$ M NaClO$_4$.
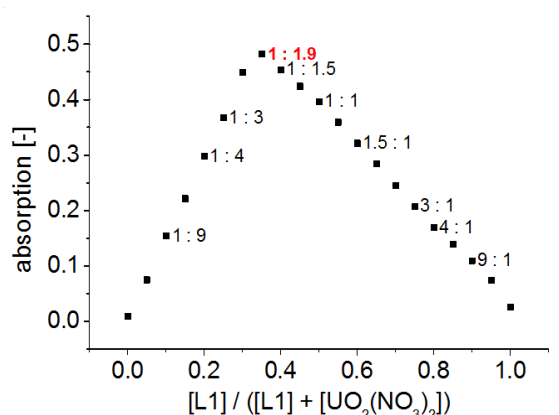
Fig. 2: Job´s Plot for complexation of L1 and UO$_2$(NO$_3$)$_2$ by UV visible spectroscopy; 100 µM stock solution in acetonitrile; $I = 0.01$ M NaClO$_4$.
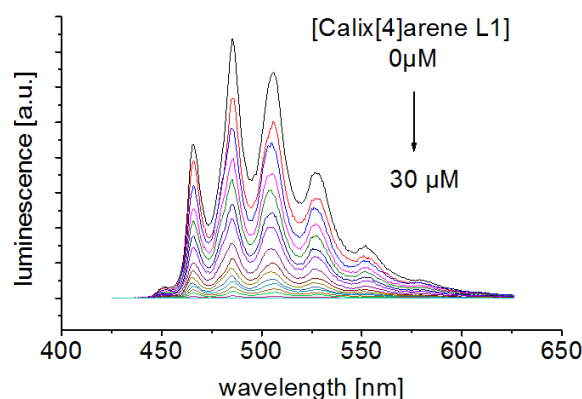
Fig. 3: Luminescence emission spectra of 50 µM UO$_2$(NO$_3$)$_2$ in acetonitrile at different calix[4]arene L1 concentrations $I = 0.01$ M NaClO$_4$.

ions of the matrix are necessary. For a better understanding of the process of complex formation X-ray diffraction analysis, NMR and IR studies are planned.

[1] Mokhtari, B. et al. (2011) *Chromatographia*. **73**, 829–847.
[2] Gil, V. M. S. et al. (1990) *J. Chem. Educ.* **67**, 473-478.

Uranyl(VI) luminescence spectroscopy at elevated temperatures

R. Steudtner, T. Haubitz,[1] C. Franzen, V. Brendler

[1]Brandenburg University of Technology (BTU) Cottbus – Senftenberg, Germany

We studied the influence of temperature and ionic strength on the luminescence characteristics (band position, decay time and intensity) of the free uranyl ion (UO_2^{2+}) in acidic aqueous solution. Under the chosen conditions an increasing temperature reduced both intensity and luminescence decay time of the UO_2^{2+} luminescence, but the individual U(VI) emission bands did not change.

EXPERIMENTAL. Time-resolved laser-induced fluorescence spectroscopy (TRLFS) experiments were performed in 10^{-5} M $UO_2(ClO_4)_2$ solution in 0.01 M $HClO_4$. As a function of ionic strength (0.01, 0.1, 1.0 and 5.0 M) the time-resolved U(VI) luminescence spectra were measured in the temperature range from 275–338 K in 5 K steps. Time-resolved fluorescence spectra were recorded with a Minilite laser (Continuum; excitation wavelength: 266 nm, energy: ~1 mJ) and an intensified CCD camera (Horiba Jobin Yvon IHR 550; delay time: varied, gate time: 2 µs). The cuvettes were cooled and heated with a temperature-controlled cuvette holder (Temperature Control Quantum Northwest) thermostated with a recirculating water bath (Lauda RM6).

RESULTS. The steady state luminescence spectra of the free UO_2^{2+} ion as function of ionic strength (top) and as function of temperature (bottom) are shown in Fig. 1. All luminescence spectra are characterized by the typical five finger structure of the UO_2^{2+} ion. The calculated emission bands of 472.3, 487.5, 510.3, 533.4 and 560.7 $\pm$ 0.5 nm are in excellent agreement with literature values [1].

Changes in temperature and ionic strength induced no spectral changes in the emission band positions, but the luminescence intensity and the luminescence decay time of the UO_2^{2+} emission are strongly influenced. Generally, an increase of luminescence intensity and luminescence decay time is caused by decreasing temperature or increasing ionic strength.

The temperature dependency of the luminescence decay time allows the determination of the activation energy (E_A) by using Arrhenius' law. In the case of luminescence decay, the rate constant k corresponds to the de-excitation constant of the luminescence species, defined as the inverse of its lifetime τ [2]. By plotting the logarithm of luminescence de-

Fig. 2: Arrhenius plot of the temperature dependence of the luminescence lifetime of the free UO_2^{2+} as function of the ionic strength.

cay constants ($\ln k$ / $\ln 1/\tau$) against inverse temperature ($1/T$), the slope of the line is equal to $-E_A/R$ (Fig. 2).

In the temperature range from 275–338 K, the graphically calculated activation energy of the free UO_2^{2+} luminescence decay shows a decrease with increasing ionic strength. In 0.01 M solution we determined a value for E_A of 50.0 ± 0.4 kJ mol^{-1}, which is reduced to 40.5 ± 1.2 kJ mol^{-1} at high ionic strength (5 M). This temperature behavior is in line with literature data on luminescence decay of excited UO_2^{2+} ions [3].

[1] Billard, I. et al. (2003) *Appl. Spectrosc.* **57**, 1027–1038.
[2] Lakowicz, J. R. (2006) *Principles of fluorescence spectroscopy*, Springer, Baltimore.
[3] Allsopp, S. R. et al. (1979) *J. Chem. Soc., Faraday Trans. I* **75**, 342–352.

Fig. 1: Steady state luminescence spectra of the free UO_2^{2+} ion as function of ionic strength at T = 293.15 K (top) and as function of temperature at I = 0.1 M (bottom).

A new technique for UV-vis measurements with metal concentrations in the sub micromolar range: reinvestigation of the uranium(VI)-acetate system

H. Brinkmann, H. Moll, T. Arnold, T. Stumpf

The speciation of uranium(VI) in the presence of acetate was investigated at 50 µM by UV-vis spectroscopy. The calculation of the single component spectra and stability constants of the formed species based on factor analysis succeeded.

To assess the safety and long term performance of deep geological repositories it is necessary to know the fate of actinides in- and outside of the waste bins. This behavior strongly depends on the surrounding conditions like pH and the presence of complexants. Acetate, being one of these complexants, occurs as degradation product of certain organic compounds (e.g. cellulose and bitumen) present in nuclear waste.[1] Additionally it acts as a model compound for more complex structures containing carboxylic groups like humic acids. In this study the uranyl acetate system was reinvestigated with absorption spectroscopy. Contrary to conventional UV-vis experiments, a Liquid Waveguide Capillary Cell (LWCC) was used, allowing measurements at uranium concentrations in the micromolar range due to much longer path lengths.

EXPERIMENTAL. A uranyl perchlorate stock solution (0.1 M) was used to prepare the samples, each with a final concentration of 5×10^{-5} M. The pH was adjusted to 2.8 with a Metrohm double junction electrode, using NaOH and $HClO_4$. The ionic strength was 1 M ($NaClO_4$) and the acetate concentration varied between 0 M and 0.8 M in 50 mM steps.

The absorption was measured between 300 nm and 600 nm with a TIDAS 100 spectrophotometer (J&M Analytik GmbH). A 250 cm LWCC (world precision instruments) was connected via optical fibers. Figure 1 depicts the structure of the LWCC (adapted from [2]).
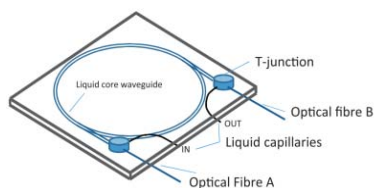
Fig. 2: Scheme of an LWCC.

The inner surface of the capillary is coated with Teflon. An additional quartz layer protects the Teflon and avoids the retention of air bubbles. The aqueous core has a higher refractive index than the Teflon wall. Therefore, the light is confined within the liquid core by total internal reflection at the core-wall interface.

Before the absorption of a sample was measured, the capillary cell was flushed with water and all air bubbles were removed from the system. Afterwards a dark and a reference spectrum were taken, which were subtracted from the sample spectra. The stability constants and single component spectra were calculated based on factor analysis with HypSpec [3].

RESULTS. Figure 2(a) shows a set of 17 spectra as function of the acetate concentration. With increasing acetate concentration up to 0.15 M a systematic increase in absorption combined with a red shift of the main absorption max-
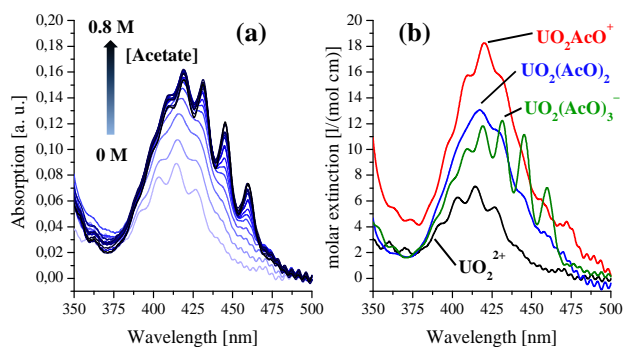
Fig. 1: Set of 17 UV-vis spectra of samples with increasing acetate concentration ([U(VI)] 50 µM, pH 2.8, 1 M $NaClO_4$) (a). Extracted single component spectra of the dominant species (b).

imum at 414 nm was observed. With acetate concentrations above 0.15 M new absorption maxima at 431, 445, and 460 nm occurred. The dependencies found in the absorption spectra could be described by the occurrence of four different uranium(VI) species. The calculated single component spectra of the three uranium-acetate complexes and of the free uranyl ion are depicted in Fig. 2(b). The corresponding spectroscopic parameters and stability constants are summarized in Tab. 1.

Tab. 1: Spectroscopic data and calculated stability constants.

Species	λ_{max} (nm)	$\varepsilon_{\lambda max}$ ($Lmol^{-1}cm^{-1}$)	$\log \beta$
UO_2^{2+}	414.5 [a]	7.1[a]	–
UO_2AcO^+	420.1[a] 418 [4]	18.2[a] 17.8 [4]	2.52 ± 0.04[a] 2.85 ± 0.05 [4] 2.58 ± 0.03[b]
$UO_2(AcO)_2$	417.3[a]	13.1[a]	5.18 ± 0.03[a] 4.37 ± 0.14[b] [5]
$UO_2(AcO)_3^-$	431.5[a]	12.2[a]	7.55 ± 0.07[a] 6.86 ± 0.04[b] [5]

[a]: present work (1 M $NaClO_4$); [b]: 1.05 M $NaClO_4$

To our knowledge, it is the first time that the single component spectra of the 1 : 2 and 1 : 3 complex could be isolated directly from a set of collected spectra using 50 µM UO_2^{2+}. The spectra in Fig. 2(b) are in general agreement with findings of Lucks *et al.* [6]. However, spectroscopic parameters were not discussed and the authors used much higher uranyl concentrations (50 mM). The spectroscopic parameters for the 1 : 1 complex are consistent with those published in [4]. The calculated stability constants for the uranium-acetate complexes are consistent with already published values. This suggests that the use of LWCCs, offers an effective method for UV-vis measurements at low uranyl concentrations.

[1] Abrahamsen, L. et al., (2015), *MIND Review (Deliverable D1.1)*, http://www.mind15.eu/wp-content/uploads/2015/11/MIND-D1.1.pdf.
[2] Pascoa, R.N. et al. (2012) *Anal. Chim. Acta.* **739**, 1–13.
[3] Gans, P. et al. (1996) *Talanta.* **43**, 1739–1753.
[4] Meinrath, G. et al. (2014) *Monatsh. Chem.* **145**, 1689–1696.
[5] Jiang, J. et al. (2002) *J. Chem. Soc., Dalton Trans.*1832–1838.
[6] Lucks, C. et al. (2012) *Inorg. Chem.* **51**, 12288–12300.

Unwilling U–U bonding in $U_2@C_{80}$: cage-driven metal–metal bonds in di-uranium fullerenes

C. Foroutan-Nejad,[1,2] J. Vícha,[2,3] R. Marek,[2] M. Patzschke, M. Straka[1]

[1]Academy of Sciences, Prague, Czech Republic; [2]Masaryk University, Brno, Czech Republic; [3]Tomas Bata University, Zlin, Czech Republic

We computationally characterize the $U_2@C_{80}$ system, which was recently detected experimentally.

Endohedral fullerene complexes have been investigated for a long time. There is only little known about actinide fullerene complexes. A few years ago Akiyama [1] reported a series of actinide fullerenes with Th, Pa, U, Np and Am. There was even evidence for a C_{80} cage containing two uranium atoms. Single actinide fullerenes have been studied also theoretically, but we take a first look at U_2C_{80}.

METHODS. We performed calculations with the Turbomole code and with Gaussian 09. According to our previous experience we employed the def-SVP basis set for all atoms and the SDD pseudopotential (ECP) for uranium. We performed DFT calculations with the BP86 functional. Analysis of the calculated electronic structures was done with MultiWFN, visualizations with VMD. Furthermore, we performed AIM analysis using the AIMALL program suite. One parameter especially proved useful in this respect. We studied the delocalization index δ (DI) [2] between the U atoms. It is defined as:

$$\delta(A \leftrightarrow B) = -2\left[\langle n_A n_B \rangle - \langle n_A \rangle \langle n_B \rangle\right] \qquad (1)$$

where $\langle n_x \rangle$ is the localization index or minimal electron population of the atoms and of the atom pair. Fullerenes with 60, 70, 80, 84 and 90 C were studied. All possible IPR structures were optimized and different spin-states were tried. Also exohedral complexes were investigated.

RESULTS. For U_2C_{80} we found that an electronic septet is lowest in energy. The optimized structure is depicted in Fig. 1. The six other IPR structures lie 10–40 kcal/mol above the minimum. Also the studied triplet to nonet states lie 10–40 kcal/mol above the septet, with the nonet being closest. The enthalpy for the encapsulation reaction is −248.6 kcal/mol. This compares well with previously calculated encapsulation energies for similar lanthanide complexes [3], which were calculated around −256 kcal/mol. Exohedral complexes show much smaller complexation energies and were therefore ruled out.

Interestingly, one can estimate the U–U bond strength computationally with the help of an isodesmic reaction. This yields an interaction energy of around −17 kcal/mol. This is substantially lower than the 70 kcal/mol for free U_2. We can draw two conclusions: There is a strong interaction between the uranium and the cage of about 115 kcal/mol per uranium atom. This interaction also weakens the U–U bond which should make the U–U interaction energy strongly depend on the cage size. The U–U distance of 3.89 Å is longer than in free U_2 (2.43 Å) with a proposed quintuple bond and slightly longer than the sum of empirical single bond radii for U [3] which yields 3.4 Å.

NPA analysis of the system gives a charge for uranium of $q_U = 0.82$. The calculated electron occupation for the encapsulated uranium is $7s^{0.21}5f^{3.54}6d^{0.98}$. This is in agreement with the previously studied lanthanide systems, giving formally M(III) metals. The three unpaired electrons on uranium are mostly located in f-orbitals. MO analysis show that
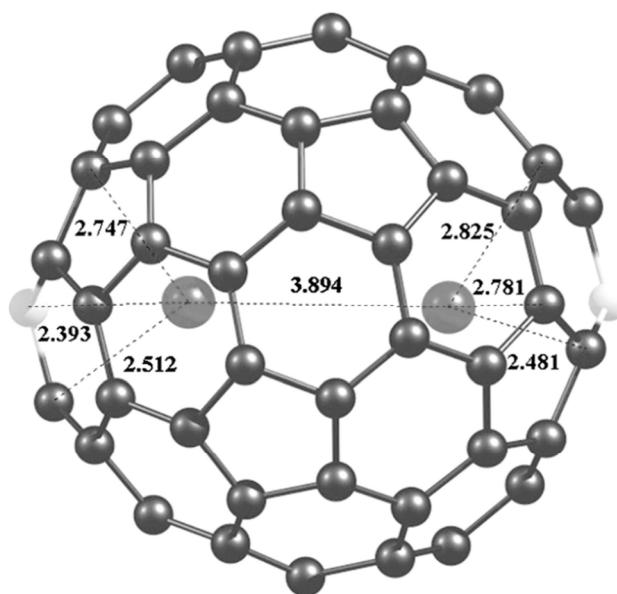
Fig. 1: Calculated Structure of U_2C_{80}.

the six SOMO's form four bonding and two antibonding U–U MO's, yielding a double ferromagnetic bond between the U atoms. The DI gives a value of 1, agreeing with the assessment of a single bond (two single-electron single bonds).

Table 1 shows bond distances, charges and DI for all investigated fullerenes. The DI correlates well with the bond distance, making them a useful indicator even in these electronically complicated systems. The U–U bond gets rapidly weaker in larger fullerenes, indeed it decreases exponentially, as would be expected. An exponential fit of δ vs. r(U–U) gives an exponential factor of −0.98 with $R^2 = 0.98$. These fullerenes present an interesting way to clamp uranium atoms at a certain distance and to investigate them.

Tab. 1: Bond distances, U charges and delocalization indices for the studied U_2C_n systems.

System	r_{U-U} (Å)	q_U NPA	δ_{U-U} (a.u.)
$^7U_2C_{60}$	2.73	0.07	2.1
$^7U_2C_{70}$	3.92	0.41	0.7
$^7U_2C_{80}$	3.89	0.82	1.0
$^7U_2C_{84}$	4.07	0.78	0.7
$^7U_2C_{90}$	6.36	0.74	0.1

[1] Akiyama, K. et al. (2001) in *Nanonetwork Materials: Fullerenes, Nanotubes and Related Systems*, American Institute of Physics, New York, USA.
[2] Foroutan-Nejad, C. et al. (2014) *Chem. Eur. J*, **20**, 10140–10152.
[3] Dolg, M. (2002) *Theor. Chem. Acc.* **108**, 143–149.
[4] Pyykkö, P. (2015) *J. Phys. Chem. A* **119**, 2326–2337.

New X-ray emission spectrometer at the Rossendorf Beamline

K. O. Kvashnina, A. C. Scheinost

A preliminary Johann-type X-ray emission spectrometer has recently been installed and tested at the Rossendorf Beamline (ROBL). The spectrometer consists of a single spherically bent crystal analyzer and an avalanche photodiode detector positioned on the vertical Rowland cycle with 1 m diameter. The instrument has been tested at the Zr-K edge.

The high energy resolution fluorescence detection (HERFD) method, using an X-ray emission spectrometer, allows recording X-ray absorption spectra with substantially better energy resolution and improves the identification of oxidation states [1]. Additionally, the setup provides the possibility to record the valence and core X-ray emission lines with resonant and non-resonant excitations [2,3]. This becomes very important when investigating the ligand orbitals of a selected element and the crystal structure of materials.

EXPERIMENTAL. The X-ray emission spectrometer consists of the crystal analyzer and the detector, which are located together with the sample on the Rowland cycle. The HERFD measurement is then performed by scanning the incident energy across the absorption edge of the selected element at the maximum of the X-ray emission line. We implemented a Johann-type X-ray emission spectrometer at the ROBL (Fig. 1) and tested the setup with a single, spherically bent, crystal analyzer Ge(220). Installation of a multiple crystal analyzer instrument with different Rowland cycle diameters is foreseen in 2016.
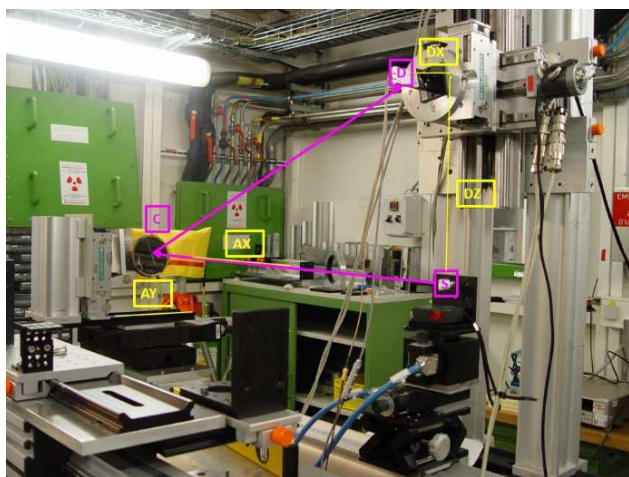
Fig. 1: Photograph of the X-ray emission spectrometer setup in the second experimental hutch of ROBL. The positions of sample (S), crystal (C), and detector (D) are marked by the respective letters in pink.

RESULTS. The Zr K-edge XANES spectra of a Zr foil and of $ZrSiO_4$ powder are shown in Fig. 2. Both samples were measured simultaneously in total fluorescence yield (TFY) and in HERFD modes at the maximum of the Zr $K\alpha_1$ emission line. We did not find any difference in the value of the maximum of the Zr $K\alpha_1$ emission line between different samples. Therefore, the X-ray emission spectrometer was not moved during the HERFD data collection on both samples. The main features in the Zr K-edge XANES correspond to the dipole-allowed transitions from the $1s$ to the $5p$ states. The improved resolution of the HERFD spectra allows identification of the clearly separated pre-edge struc-
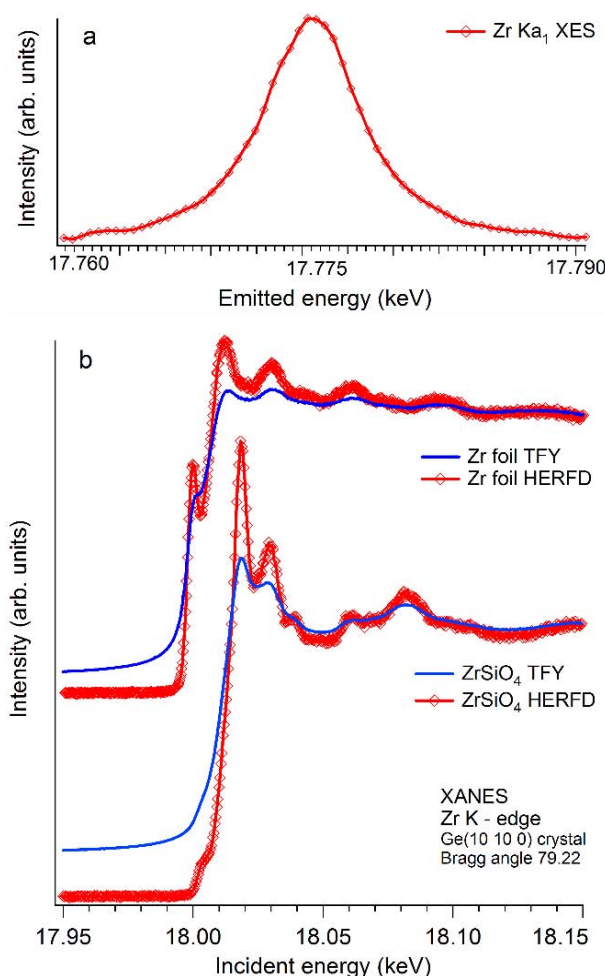
Fig. 2: Zr $K\alpha_1$ X-ray emission spectrum recorded on the Zr foil (a). Zr K-edge XANES spectra of the Zr foil and of $ZrSiO_4$ powder recorded in HERFD (red) and TFY (blue) modes simultaneously (b).

ture in the spectra of both Zr compounds, which arises from the dipole-forbidden but quadrupole-allowed transitions between $1s$ and $4d$ states. The pre-edge features indicate the distortion of the crystal structure of the solids and show the effect of the hybridization between the d, p states of Zr and the unoccupied states of the ligands. The HERFD spectra collected at the ROBL are in a good agreement with the HERFD spectra previously recorded by Wilke and co-authors [4] at the dedicated XES beamline ID26 of ESRF. The spectrometer will be further developed from 2016 on for studying nuclear waste materials and environmental applications [1–3,5].

[1] Kvashnina, K. O. et al. (2013) *Phys. Rev. Lett.* **111**, 253002.
[2] Kvashnina, K. O. et al. (2014) *J. Electron Spectrosc. Relat. Phenom.* **194**, 27–36.
[3] Kvashnina, K. O. et al. (2015) *Anal. Chem.* **87**, 8772–8780.
[4] Wilke, M. et al. (2012) *Earth Planet. Sci. Lett.* **349–350**, 15–25.
[5] Vitova, T. et al. (2010) *Phys. Rev. B* **82**, 235118.

Basic TRLFS data of some lanthanides using a tunable laser system and a red-optimized detection system

A. Heller,[1] A. Barkleit, G. Geipel

[1]Technische Universität Dresden, Institute for Zoology, Molecular Cell Physiology and Endocrinology, Dresden, Germany

Lanthanides are crucial raw materials for modern high-tech products and used in medicine, especially as contrast enhancing agents for magnetic resonance imaging [1]. To study their interactions in the geo- and biosphere, Time-Resolved Laser-Induced Fluorescence Spectroscopy (TRLFS), which is a non-invasive, very sensitive, and versatile state of the art method, is used. Up to now, TRLFS is well established for actinides but only some lanthanides (especially Eu and Tb). To extent this scope, we investigate the basic luminescence properties of all lanthanide elements.

EXPERIMENTAL. Chlorides of Nd, Gd, Tb, Ce, and Ho (all $LnCl_3 \cdot xH_2O$ purchased from Sigma) were dissolved in deionized water at concentrations from 10^{-2} to 10^{-9} M. Ionic strength was not adjusted and the pH of all solutions was 4–5.

Excitation of the Ln^{3+} aqua ions was performed using an injection seeded Nd:YAG pumped OPO laser system (Powerlite 9020 DLS equipped with a Sunlite EX OPO and a FX-1 doubler unit; all purchased from Continuum) with a repetition rate of 20 Hz and a pulse width of < 6 ns. The system is tunable within the wavelength range of 230–1800 nm. Luminescence spectra were recorded at 90° to the excitation beam using a detection system composed of a spectrograph equipped with 300, 900, and 1200 lines/mm gratings and an ICCD camera (Shamrock SR-303i and iStar 340T DH340T-18H-163; both purchased from Andor). Measurement parameters, such as excitation wavelength, slit width, gate width, and delay steps, differ from element to element.

RESULTS. Ce, Nd, Gd, and Tb show distinct luminescence spectra. The single emission spectra of all four Ln^{3+} aqua ions and the luminescence decay curves are depicted in Fig. 1 and 2, respectively. However, so far, no specific luminescence of Ho was detectable although the excitation wavelength was varied over a wide range.

The Ce^{3+} aqua ion exhibits a spectrum with one broad peak centered at approximately 370 nm. Time-resolved measurements yielded mono-exponential decay curves and a
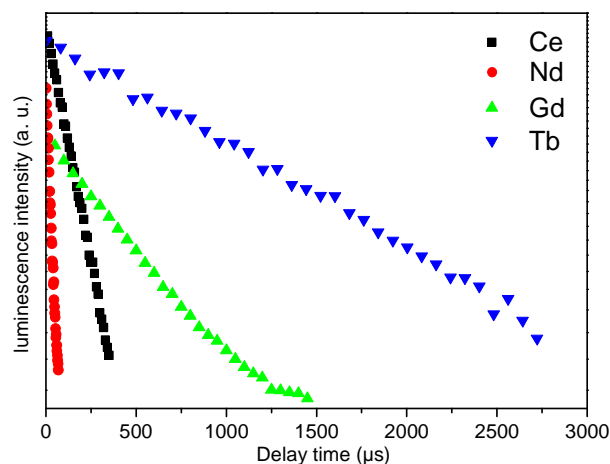
Fig. 2: Single luminescence decay curves of Ce^{3+}, Nd^{3+}, Gd^{3+}, and Tb^{3+} aqua ions.

short luminescence lifetime of 44 ± 2 ns. The luminescence intensity is very strong and the detection limit approximately 10^{-9} M.

Luminescence of the Nd^{3+} aqua ion occurs in the range of 750–950 nm. The emission spectrum exhibits two fine-structured peaks at 796/804 nm and 865/874/890 nm. The decay mode is mono-exponential and the luminescence lifetime of 30 ± 1 ns is very short. The luminescence intensity is weak and the detection limit of the Nd^{3+} aqua ion is as high as 10^{-5} M.

The Gd^{3+} aqua ion exhibits a sharp luminescence peak at 312 nm. Time-resolved measurements yielded bi-exponential decay curves and corresponding luminescence lifetimes of 30–40 µs and 180–220 µs. Reason for this behavior is yet unknown. The luminescence intensity is strong and the detection limit is about 10^{-6} M.

Luminescence of the Tb^{3+} aqua ion occurs in the range of 450–700 nm. The emission spectrum shows four partly split peaks of strong intensity at 491, 546, 582/587, and 621 nm as well as three very weak peaks at 648/655, 670, and 681 nm. The decay mode is mono-exponential and the luminescence lifetime of 423 ± 12 µs is quite long. Luminescence from the strongest peak is still detectable in solutions with 10^{-8} M, which is also the detection limit.

The spectroscopic parameters of Ce, Nd, Gd, and Tb reported here are in very good agreement with sparse literature data [2]. However, the occurrence of Raman bands from water has to be taken into account, when using excitation wavelengths < 400 nm. Interference of these very short-lived bands with the luminescence peaks of the Ln^{3+} aqua ions can be excluded either by choosing the appropriate gate of the spectrograph or by prolonging the delay between laser pulse and luminescence recording.
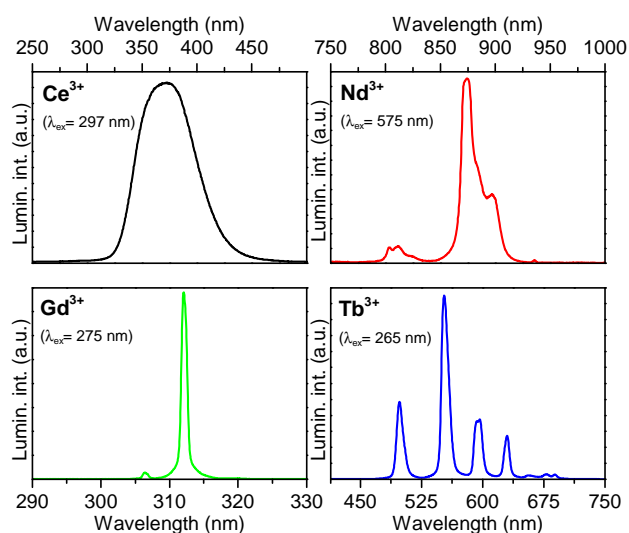
Fig. 1: Single emission spectra of Ce^{3+}, Nd^{3+}, Gd^{3+}, and Tb^{3+} aqua ions.

[1] Elsner, H. (2011) *Commodity Top News* **36**.
[2] Bünzli, J.-C. G. and Piguet, C. (2005) *Chem. Soc. Rev.* **34**, 1048–1077.

Long-Lived Radionuclides & Transport Phenomena in

GEOLOGICAL SYSTEMS

Redox dependent interfacial reactivity of hexavalent radionuclides

S. Hellebrandt, M. Schmidt, K. E. Knope,[1] S. S. Lee,[1] A. J. Lussier,[2] J. E. Stubbs,[3] P. J. Eng,[3] L. Soderholm,[1] P. Fenter[1]

[1]Chemical Science and Engineering Division, Argonne National Laboratory, Argonne, IL/USA; [2] Department of Civil Engineering and Geological Sciences, University of Notre Dame, Notre Dame, IN/USA; [3] Center for Advanced Radiation Sources, University of Chicago, Chicago, IL/USA

The interaction of $U^{VI}O_2^{2+}$ and $Pu^{VI}O_2^{2+}$ with muscovite mica and the effect on the actinides' different redox properties were investigated using a combination of surface X-ray diffraction, alpha spectrometry and GI-XANES. Under similar experimental conditions, no sorption is observable upon reaction with UO_2^{2+}, in contrast Pu(IV)-oxo-nanoparticles were formed on the muscovite (001) basal plane after reaction with PuO_2^{2+} [1]. We attribute the difference in the observed reactivity to the greater stability of low oxidation states for Pu relative to U.

EXPERIMENTAL. For all experiments freshly cleaved mica single crystals are reacted with the actinide-bearing solution overnight. For the PuO_2^{2+} experiment the solution composition is $[PuO_2^{2+}] = 0.1$ mM, $[NaCl] = 0.1$ M, at pH = 3.2. The conditions for the UO_2^{2+} experiment are identical, but a higher concentration $[UO_2^{2+}] = 1.0$ mM was chosen to enhance uranyl adsorption.

RESULTS. Figure 1 shows the interfacial structure of muscovite after adsorption of UO_2^{2+} (red) and PuO_2^{2+} (blue), and after reaction with only the background electrolyte (NaCl) as a reference [2]. The structures after reaction with UO_2^{2+} and the reference are almost identical, indicating there is no adsorbed uranium at the muscovite interface. The structure of the Pu-system is completely different, it shows two broad peaks at 10 and 32 Å, and several sharper peaks located close to the surface (≤ 8 Å). This large electron density must be related to an uptake of Pu at the interface. This is confirmed by RAXR. The Pu RAXR spectra (Fig. 2B) show modulations at the Pu L_{III} adsorption edge, confirming that Pu is present at the muscovite surface. GI-XANES identifies Pu on the surface as Pu(IV). The oxidation state of Pu had been adjusted electrochemically, and was controlled by UV-vis spectroscopy, hence a reduction must have occurred during the experiment. Apparently sorption of Pu^{4+} is possible due to its significantly higher charge compared to Na^+, while sorption of plutonyl as well as uranyl is suppressed by
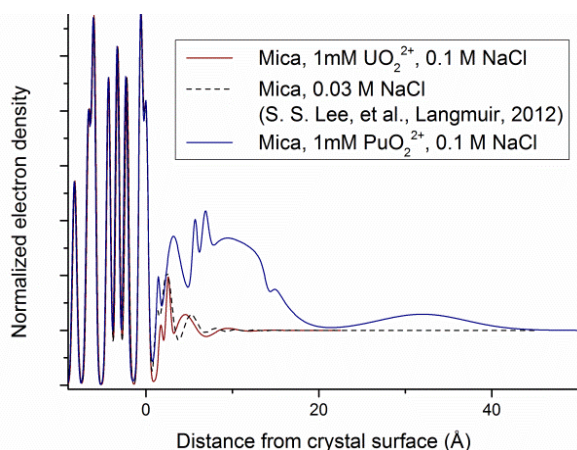
Fig. 1: Interfacial structure. Total electron density of the U (red) and Pu (blue) system, and a pure NaCl system (dashed), derived by CTR. The electron density is normalized to that of bulk water ρ(bulk water) = 0.33 e$^-$/Å^3. The average height of muscovite surface oxygens is set to be z = 0 Å.
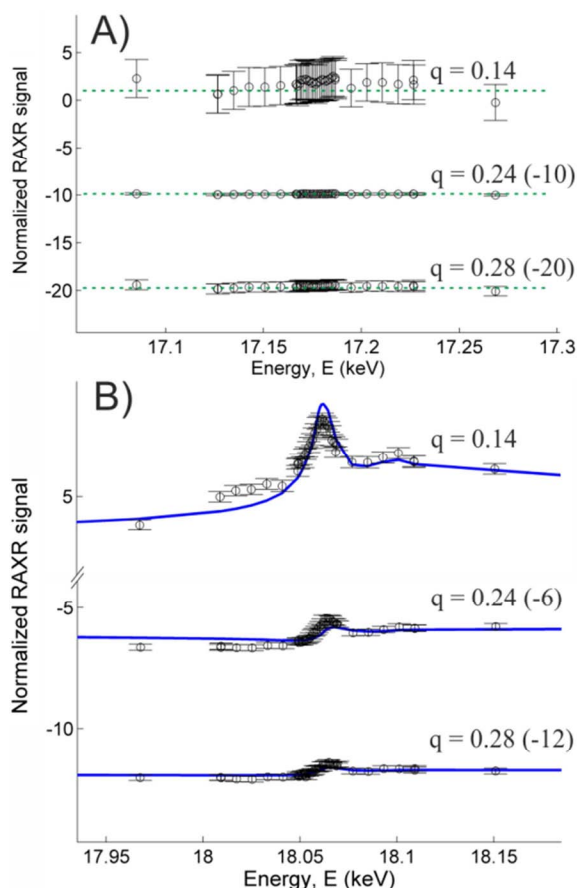
Fig. 2: Selected RAXR data (black circles) measured from the muscovite (001) basal plane. A) data after reaction with UO_2^{2+}. The line serves as a "guide-to-the-eye". B) data after reaction with PuO_2^{2+}, the blue represents the best fit model. Both figures show data of several q (Å^{-1}) offset in brackets for better clarity.

an excess of sodium.

Once a threshold of $[Pu^{4+}]$ is reached, oligomerization may occur, and Pu^{4+} is removed from the redox equilibrium. The reaction then becomes "auto-catalytic". The results demonstrate how redox behavior strongly influences the sorption behavior of hexavalent actinides.

[1] Hellebrandt, S. et al. (2016) *J. Phys. Chem. C*, in preparation.
[2] Lee, S. S. et al. (2012) *Langmuir* **28**, 8637–8650.

The surface destabilization effect of nitrate on the calcite (104) – Water interface and yttrium(III) sorption thereon

S. E. Hellebrandt, S. Hofman, J. E. Stubbs,[1] P. J. Eng,[1] T. Stumpf, M. Schmidt
[1]Center for Advanced Radiation Sources, University of Chicago, Chicago, IL USA

Calcite, as a most abundant mineral on earth, was studied with X-ray reflectivity under the influence of $NaNO_3$ [1]. The calcite (104) surface undergoes significant destabilization effects in the presence of $NaNO_3$, which occurs as partial dissolution and the formation of an amorphous layer at the interface. The disordering of the surface reaches more than 15 Å into the crystal bulk. Furthermore, this surface modification has also an effect on the sorption behavior of the rare earth element Y. Without $NaNO_3$ Y^{3+} adsorbs as both inner and outer sphere complexes, this was verified with resonant anomalous X-ray reflectivity (RAXR). If $NaNO_3$ is present, both species desorbs from the surface completely.

Transuranic elements as well as calcite play a significant role in the safety assessment of nuclear waste disposal sites. Here, the rare earth element yttrium served as a nonradioactive homologue to americium and curium, as its ionic radius and chemical behavior are similar. Calcite can be found at these sites in the near field as a secondary phase (e.g. by weathering of the cementitious materials) and as a constituent mineral in the surrounding host rocks. Geochemically, it has the potential to adsorb ions at its surface as well as substitute structural Ca^{2+} by guest ions with an ionic radius similar to calcium, such as americium and curium, in its crystal lattice. The influence of different dissolved cations on the incorporation process was investigated by Schmidt et al. [2]. They showed with time-resolved laser fluorescence spectroscopy (TRLFS) and Eu(III)/Cm(III) that there exists a coupled substitution mechanism (one Eu(III)/Cm(III) and one Na(I) ion replace two Ca(II) ions). Recently, Hofmann et al. [3] showed that the sorption of trivalent lanthanides and actinides can be affected by anionic ligands like nitrate. Atomic force microscopy indicated that in the presence of $NaNO_3$ a "gel-like layer" with lower crystallinity but unknown composition forms on the calcite surface. TRLFS with Eu(III) revealed the incorporation of the Eu(III) ions in this layer, instead of an incorporation directly into the calcite lattice.

EXPERIMENTAL. We used two surface specific high resolution X-ray reflectivity techniques, crystal truncation rod (CTR) measurements and resonant anomalous X-ray reflectivity (RAXR). The experiments were run *in situ*, with the mineral in contact with a thin solution layer. CTR results in an overall electron density profile from both, the first layers of the crystal bulk and the adsorbed water layer (including sorbed species). RAXR yields the near surface distribution of a distinct element (here: Y).

RESULTS. For our experiments we used freshly cleaved (along the (104) plane) calcite crystals, which were stored in calcite saturated solution (CSS). The sample was reacted with Y(III) over a course of ~ 170 hours and transferred to the diffractometer. Low quantities [~ 0.05 Y/A_{UC} (A_{UC} = area of the calcite unit cell ~ 20.20 Å²)] of adsorbed Y were detected on the calcite surface with more than one species with an average height of ~ 3 Å (see Fig. 1). In a second step, the sample was then flushed with a CSS con-
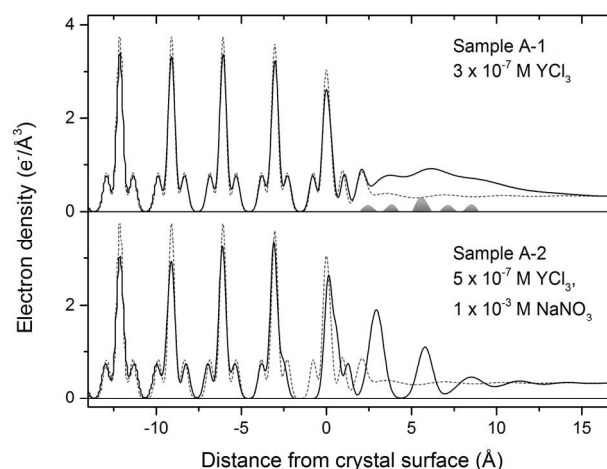
Fig. 1: e^--density profiles of the calcite (104) surface along the surface normal direction from best-fit models of CTR data. Top: Sorption of Y^{3+}. Bottom: After flushing with CSS containing $NaNO_3$. Dashed lines: Calcite/CSS reference system [4]. The approximate range for Y adsorption, obtained from model-independent analysis of RAXR data [5] is shown as a grey area plot.

taining 10 mM $NaNO_3$. After a short contact time with $NaNO_3$ (~ 48 h), Y was no longer detectable and consequently must have desorbed from the calcite surface entirely. CTR experiments for longer contact times (14 d) with $NaNO_3$ showed that nitrate quickly affects the water sorption structure on calcite. The first peak of the interfacial structure and the first, strongly destabilized calcite lattice layer (see Fig. 1) we identify as the amorphous surface layer, which has been described previously [3]. The amorphous layer pushes the interfacial water structure to a larger height above the crystal surface, structures the water up to large distances from the interface and prevents the adsorption of Y^{3+} on the calcite surface directly.

[1] Hellebrandt, S. E. et al. (2016) *Environ. Sci. Technol. Lett.,* submitted.
[2] Schmidt, M. et al. (2008) *Angew. Chem. Int. Ed.* **47**, 5846–5850.
[3] Hofmann, S. et al. (2014) *Geochim. Cosmochim. Acta* **125**, 528–538.
[4] Fenter, P. et al. (2012) *Geochim. Cosmochim. Acta* **97**, 58–69.
[5] Park, C. et al. (2007) *J. Appl. Crystallogr.* **40**, 290–301.

Molecular dynamics simulations of the calcite/solution interface as a means to explore surface modifications induced by nitrate

S. Hofmann, P. Spijker,[1] K. Voitchovsky,[2] M. Schmidt

[1]Department of Applied Physics, COMP Centre of Excellence, Aalto University, Helsinki, Finland; [2]Physics Department, Durham University, Durham, United Kingdom

The reactivity of calcite, one of the most abundant minerals in the earth's crust, is determined by the molecular details of its interface with the contacting solution. Recently, it has been found that trace concentrations of $NaNO_3$ severely affect calcite's (104) surface and its reactivity. Molecular dynamics (MD) simulations reveal density profiles of different ions near calcite's surface, with NO_3^- able to reach closer to the surface than CO_3^{2-} and in higher concentrations. Additionally, incorporation of NO_3^- into the surface significantly disturbs the water structure at the interface.

EXPERIMENTAL. The MD simulations protocol used for this study [1] was published previously [2]. Based on the system dimensions of $105 \times 64 \times 137$ Å^3 (of which 40 Å in the z-direction is the calcite crystal), the ion concentration is approximately 250 mM. The simulation was run for 5 ns at ambient conditions (310 K and 1 bar). Simulations were carried out using the MD code NAMD [3] with the empirical force field CHARMM [4] dictating all atom interactions. As the nitrate ion is not part of the standard distribution of the CHARMM force fields, its Van der Waals [5] and charge [6] parameters were obtained elsewhere and converted to the proper units and functional forms as used in the force field. The simulations are run in parallel on a typical Linux commodity cluster and analysis is performed visually using VMD [7] or numerically using the Python library MDAnalysis [8].

RESULTS. The densities of NO_3^-, CO_3^{2-}, and H_2O perpendicular to the calcite surface are presented in Fig. 1. The occurrence of at least three hydration layers is visible from the density of the water molecules. This hydration structure is in good agreement with simulations by Fenter et al. and also qualitatively similar to previous experimental findings
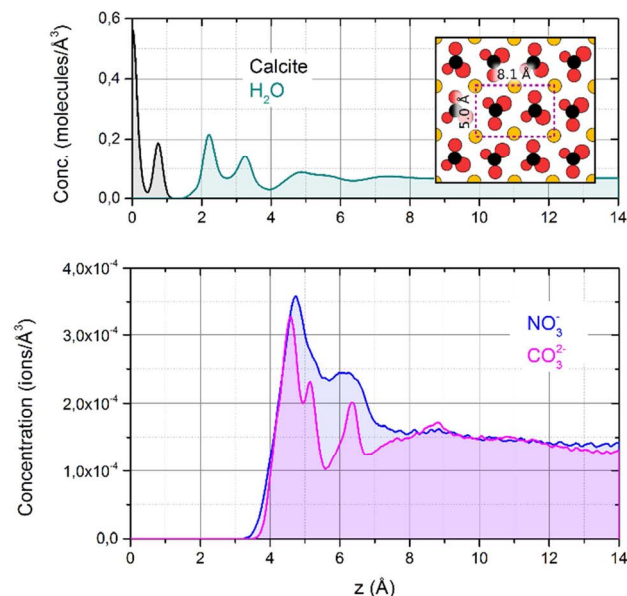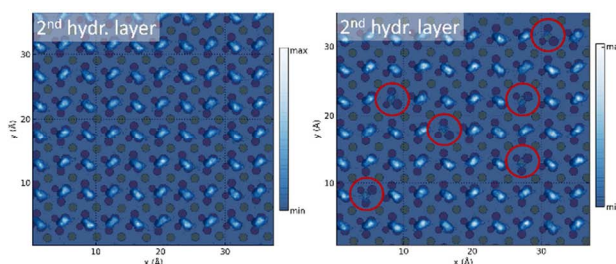
Fig. 2: Simulated water densities above the pristine calcite (104) surface (left) and a modified surface at the height of the 2nd hydration layer (right).

[9, 10]. In the bottom panel the ion densities for NO_3^- and CO_3^{2-} are shown. Water density profiles are not appreciably affected by the presence of the ions. Nitrate and carbonate anions cannot reach past the second hydration layer, but are able to pass the third layer and aggregate directly on top of the second adsorbed water layer. Integration of the respective ion densities (integration window 3–10 Å) reveals that nitrate is 25% more concentrated than carbonate at the interface. This aggregation clearly shows the high affinity of nitrate towards the calcite surface, even exceeding that of carbonate – a behavior that could explain the unique effect of $NaNO_3$ upon calcite [11]. Figure 2 displays the lateral density of water's oxygen atoms in planes taken parallel to the surface, at the location coinciding with the second hydration layer. Based on the assumption that the high affinity of NO_3^- towards the calcite surface will eventually lead to a substitution reaction, a second simulation was run where six surface carbonate groups within the surface plane were randomly replaced by nitrate ions. Their position is marked by red circles in the right half of Fig. 2. The second water layer exhibits definite changes with reduced water density on the surface, leaving the incorporation sites less hydrated within this layer. The overall structure of the liquid is disturbed at these sites.

Nitrate's strong affinity to the calcite surface and the disrupting effect upon the hydration structure at the interface gives new insight into the surface modification by $NaNO_3$.

[1] Hofmann, S. et al. (2016) *Sci. Rep.* (submitted).
[2] Ricci, M. et al. (2013) *Langmuir* **29**, 2207–2216.
[3] Phillips, J. C. et al. (2005) *J. Comput. Chem.* **26**, 1781–1802.
[4] Brooks, B. R. et al. (2009) *J. Comput. Chem.* **30**, 1545–1614.
[5] Baaden, M. et al. (2001) *J. Phys. Chem. B* **105**, 11131–11141.
[6] Del Popolo, M. G. et al. (2004) *J. Phys. Chem. B*, **108**, 1744–1752.
[7] Humphrey, W. et al. (1996) *J. Mol. Graph. Model.* **14**, 33–38.
[8] Michaud-Agrawal, N. et al. (2011) *J. Comput. Chem.* **32**, 2319–2327.
[9] Heberling, F. et al. (2014) *Appl. Geochem.* **45**, 158–190.
[10] Fenter, P. et al. (2013) *J. Phys. Chem. C* **117**, 5028–5042.
[11] Hofmann, S. et al. (2014) *Geochim. Cosmochim. Acta* **125**, 528–538.

Fig. 1: Simulated distribution of water and anionic species on the calcite (104) surface. The inset shows the crystal structure of the exposed surface as obtained from the simulations.

Sorption of Np(V) onto orthoclase and muscovite

C. Richter, F. Bok, V. Brendler

Selected batch experiments were performed to study the influence of pH, solid-liquid-ratio, and ionic strength on the sorption of Np(V) on orthoclase and muscovite. The obtained results were used to derive surface complexation constants for the sorption of Np(V) under the used conditions. At pH above 10, precipitation coupled to reduction was observed, probably induced by redox-sensitive impurities in the minerals.

EXPERIMENTAL. Sorption experiments were performed under ambient atmosphere with orthoclase and muscovite at solid-liquid-ratios (SLRs) of 1/20 and 1/80 g mL^{-1}. A concentration of 10^{-6} M Np(V) was used in 0.01 M NaClO$_4$ and the pH range of 5 to 12 was investigated. Additional batch experiments in 1 M NaClO$_4$ (SLR of 1/20 g mL^{-1}, 10^{-6} mol L^{-1} Np(V)) were performed in the pH range 7 to 10 relevant for Np(V) surface complexation.

RESULTS. Sorption of Np(V) onto both orthoclase and muscovite increases with rising pH. On the contrary, SLR has no significant effect on the amount of sorption. A shift of the sorption curve at higher ionic strength is not observed indicating inner-sphere sorption of neptunium.

Because the amount of sorption is quite low, any independent spectroscopic identification of the sorption complex is quite difficult, thus Gibbsite served as an analogue [1]. Np(V) sorption up to pH 10 can be accurately described by the ≡XO–NpO$_2$ surface species. Because of the weak sorption, including more species does not improve the fit (Fig. 1). The log $K°$ values obtained in this work (Tab. 1) are in good agreement to literature data [2] for other alumosilicates: log $K° = -4.04$ for kaolinite, log $K° = -3.62$ for gibbsite, and log $K° = -4.15$ for biotite.

However, at high pH values ($\geq$ 10) sorption increases rapidly. This behavior deviates from previous observations [3–6] for Np(V) sorption onto kaolinite, montmorillonite, and gibbsite, all in presence of carbonate. Actually, the observed higher fraction of immobilized Np in the alkaline range can hardly be caused by sorption. Above pH 8, negatively charged neptunium-carbonate complexes dominate the aquatic Np speciation and the surfaces of both investigated minerals are negatively charged, too. Thus, any formation of a neptunium surface complex is hindered by electrostatic repulsion. Vial wall sorption could also be ruled out by separate checks.

As a last option formation of Np precipitates was considered. The measurement of the redox potential of 10^{-6} M Np samples at pH 6 and 12 indicated a shift of the Eh from
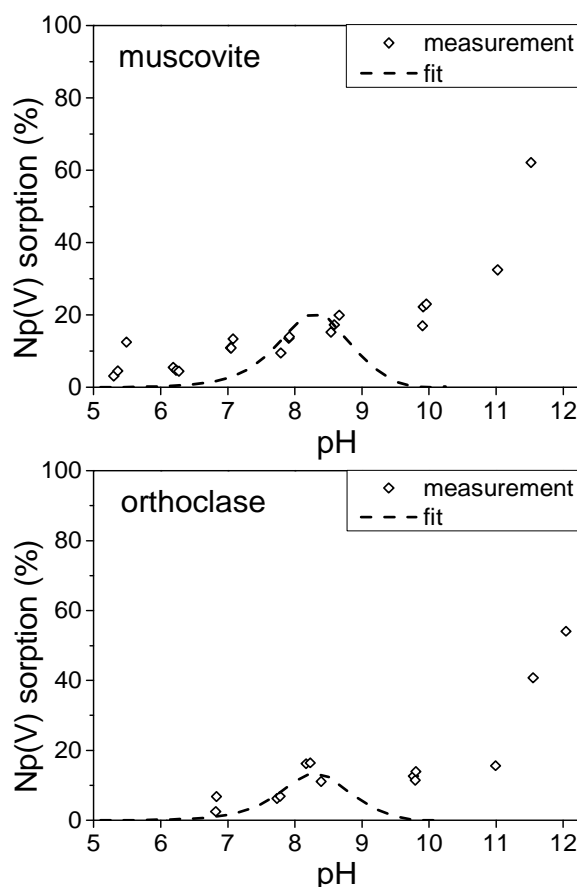
Fig. 1: Fitted surface speciation with ≡XO–NpO$_2$ onto muscovite and orthoclase (0.01 M NaClO$_4$, SLR 1/20, 10^{-6} M Np(V)).

0.3 V down to approximately 0 V. Thus, at higher pH values Np samples may be reduced. A closer look to the pH-Eh diagram of neptunium showed that with increasing pH and a slight shift of Eh to lower values the formation of Np(IV) might be possible. Furthermore, a reduction of Np(V) to Np(IV) can be forced by redox-sensitive Fe impurities of the mineral, see Gogolev et al. [7]:

$$Fe^{2+} + NpO_2^+ \leftrightarrow Fe^{3+} + NpO_2(am, hyd)$$
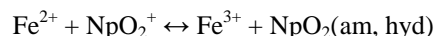
However, it is not clear yet which process triggers the reduction at higher pH values in the investigated systems, it might also be due to some of the mineral impurities other than iron. From these considerations, the formation of a Np precipitate like NpO$_2$(am, hyd) can be assumed, or the reduction of Np(V) to Np(IV) followed by sorption of Np(IV), which is generally stronger than sorption of Np(V). Further studies are required to resolve these questions.

[1] Gückel, K. et al. (2013) *Environ. Sci. Technol.* **47**, 14418–14425.
[2] Wang, P. M. et al. (2001) *Indust. Eng. Chem. Res.* **40**, 4428–4443.
[3] Schmeide, K. et al. (2010) *App. Geochem.* **25**, 1238–1247.
[4] Tachi, Y. et al. (2010) *Radiochim. Acta* **98**, 711–718.
[5] Turner, D. R. et al. (1998) *Clays Clay Min.* **46**, 256–269.
[6] Wu, T. et al. (2009) *Radiochim. Acta* **97**, 99–103.
[7] Gogolev, A. V. et al. (2006) *Radiochem.* **48**, 249–253.
[8] Arnold, T. et al. (2000) *Report FZR-272*, p. 31.
[9] Arnold, T. et al. (2001) *Environ. Sci. Technol.* **40**, 4646–4652.

Tab. 1: Recommended surface complexation parameters for Np(V) sorption onto orthoclase and muscovite.

	Orthoclase	**Muscovite**
SSA [m² g^{-1}]	0.083[a]	0.66[a]
SSD [sites nm^{-2}]	3.1[b]	2.61[c]
pK_1	6.47[b]	6.01[c]
pK_2	−7.85[b]	−7.86[c]
log $K°$ ≡XO–NpO$_2$	−3.92 ± 0.03[a]	−4.58 ± 0.03[a]

[a]: this work, [b]: adapted from albite in [8], [c]: [9].

Interfacial reaction of Sn^{II} on mackinawite (FeS)

S. Dulnee, A. C. Scheinost

The sorption and redox reactions between the fission product Sn, and the highly reactive steel-container corrosion-product mackinawite were investigated by Sn-K edge XANES and EXAFS spectroscopy [1].

EXPERIMENTAL. Mackinawite was synthesized in an anoxic glovebox (pO$_2$ < 1 ppm) as described earlier [2]. After washing, freeze-dried subsamples were analyzed by XRD and TEM, while the suspension was directly used for Sn sorption experiments. Suspensions with 2 g/L were equilibrated in 0.01 M NaCl for 24 hours at the desired pH values before adding Sn^{II} solutions to obtain nominal Sn^{II} loadings of 12.5 µmol/g. After 24 h equilibration, pH and Eh were measured, the samples centrifuged and the bottom slurry transferred to dedicated sample holders, which were immediately flash frozen in LN$_2$. XAFS spectra were measured at ROBL in fluorescence at 15 K.

RESULTS. XRD and TEM (insert in Fig. 1) confirmed the solid phase as low-crystalline mackinawite with a high surface area of about 330 m^2/g. Sn^{II} has a very high affinity towards this mackinawite, with log R_d > 5 across the whole pH range defined by the stability field of mackinawite (Fig. 1, note the increase of dissolved Fe below pH 6 and above pH 10). The measured Eh/pH values plotted in a Pourbaix diagram show that the sorption samples remain up to pH ~8 in the stability fields of mackinawite and sulfide, while they are in the stability fields of hematite (as proxy for Fe^{III} oxides) and sulfate above pH 9 (Fig. 2).

The Sn-K edge XANES (Fig. 3, left) of two samples at pH 5.7 and 7.0 show an edge energy of ~5 eV inferior to that of the samples at pH 7.7 and 9.1, and a much smaller white line, indicative of Sn^{II} in sulfur coordination. In contrast, the XANES of the two samples at higher pH is an indicative for Sn^{IV} in oxide coordination. This is further confirmed by the EXAFS Fourier transform magnitude (Fig. 3, right). A shell fit of the sample at pH 5.7 provided 2 S atoms at a distance of 2.38 Å from the central Sn atom, another 2 S atoms at 2.59 Å, and 0.5 Fe atoms at 2.86 Å. This radial distribution of atoms can be rationalized as a Sn^{II}S$_4$-complex, which forms with the mackinawite surface an innersphere sorption complex through the two shorter Sn–S bonds, while the two longer Sn–S point away from the surface into the solution.
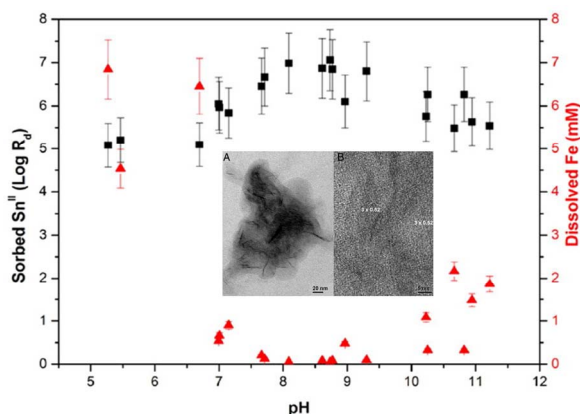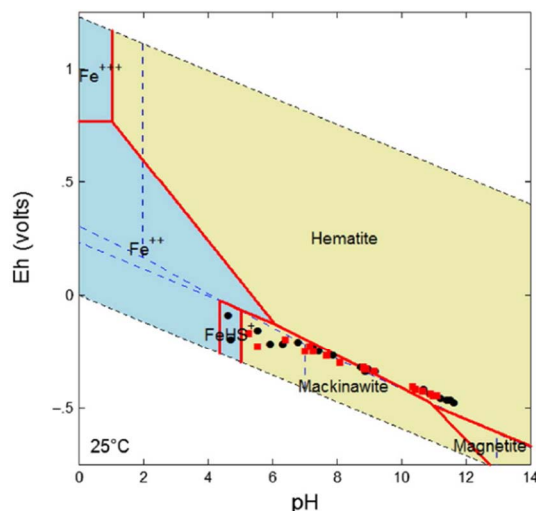
Fig. 2: Eh-pH diagram of the system Fe-S-H$_2$O at 25 °C showing the measured values in mackinawite suspensions before (black dots) and after (red squares) the addition of 12.5 µmol/g Sn^{II}. The diagram was calculated with Geochemists Work Bench using the expanded LLNL database and Fe and S concentrations of 10^{-3} M.
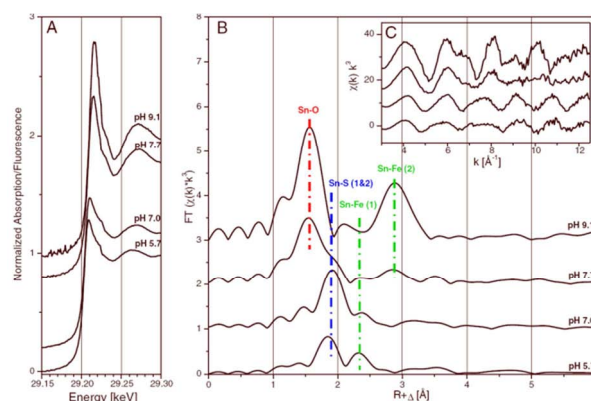
Fig. 3: Sn K-XANES (left) and EXAFS spectra (right) of selected samples at pH 5.7, 7.0, 7.7 and 9.1.

A shell fit of the sample at highest pH resulted in 6 O atoms at 2.04 Å and 6 Fe atoms at 3.29 Å, commensurate to Sn^{IV} replacing Fe atoms in the structure of green rust.

These mechanisms observed by spectroscopy are relevant not only for Sn, but also for the interaction of mackinawite with other redox-sensitive metal ions with soft Lewis acidity character (e.g. Sb, Pb, Cd, Hg). In spite of the changing Sn oxidation state, sorbent properties and ultimately retention mechanisms, retention of Sn in the mackinawite system is very strong, with log R_d values between 5 and 7 across a wide pH range. Similar high log R_d values have been recently observed also in the presence of magnetite [3] and goethite [4]. Given the ubiquitous nature of these minerals in the near-field and the far-field of potential nuclear waste repositories, ^{126}Sn is not expected to be a major contributor to the radiotoxic inventory potentially released from spent nuclear fuel or other radioactive waste forms.

[1] Dulnee, S. et al. (2015) *J. Contaminant Hydrol.* **177–178**, 183–193.
[2] Kirsch, R. et al. (2011) *Environ. Sci. Technol.* **45**, 7267–7274.
[3] Dulnee, S. et al. (2013) *Environ. Sci. Technol.* **47**, 12852–12859.
[4] Dulnee, S. et al. (2014) *Environ. Sci. Technol.* **48**, 9341–9348.

Fig. 1: Schematic representation of solid phases, solution species and the formation of the poly-oxo cluster U$_{38}$ as a function of reaction time.

Technetium(VII,IV) retention by iron(II)-containing minerals

K. Schmeide, F. Spranger, C. Franzen, S. Weiss, K. Heim, H. Foerstendorf, F. Bok, K. O. Kvashnina

The Tc retention by the iron(II)-containing minerals magnetite ($Fe^{II}Fe^{III}_2O_4$) and siderite ($Fe^{II}CO_3$) was studied by means of batch sorption experiments as well as ATR FT-IR and XAS spectroscopy. The strong Tc retention could be attributed to surface-mediated reduction of Tc(VII) to Tc(IV).

Under oxic conditions, Tc is present as pertechnetate (TcO_4^-, Tc(VII)), which is a highly soluble, aqueous species known not to sorb significantly on minerals or sediments. However, under anaerobic conditions and in the presence of a reducing agent, Tc(VII) is reduced to Tc(IV). Thereby, the Tc solubility decreases drastically due to precipitation of respective hydrolysis products [1, 2]. Iron(II)-minerals, ubiquitous in nature and corrosion products of carbon steel canisters storing radioactive waste, are characterized by redox reactivity and a high sorption capacity. Thus, they can control the environmental fate of radionuclides, namely Tc, the aim of this study.

EXPERIMENTAL. The preparation of mineral phases (magnetite, siderite) and of sorption samples was performed under anoxic conditions (glove-box with pure N_2 atmosphere) at RT with degassed Milli-Q water.
Conditions of batch sorption experiments: $[^{99}TcO_4^-] = 1 \times 10^{-5}$ M; S/L = 0.2 g/L; $I = 0.1$ or 1 M (NaCl). Pre-equilibration and sorption time were 2 d each, samples were analyzed by liquid scintillation counting.
XAS samples: $[^{99}TcO_4^-] = 1268$ or 634 kBq/40 mL; S/L = 7.5 g/L; $I = 0.1$ M (NaCl); pH 7 (mag.) and 8 (sid.). The Tc retention onto magnetite was also studied by *in situ* IR spectroscopy. After conditioning with 0.1 M NaCl solution, the mineral film was rinsed with the sample solution ($[TcO_4^-] = 5 \times 10^{-4}$ M; 0.1 M NaCl) for 60 min.

RESULTS. Figure 1 shows an almost complete Tc retention by magnetite and siderite independent of pH and ionic strength. This supports results found by Kobayashi et al. [2]. According to E_h/pH-calculations (not shown), the redox potentials of selected Tc/magnetite samples, monitored at the end of the sorption experiments, are at the borderline between Tc(VII) and Tc(IV) (140 mV at pH 6; −151 mV at pH 10). This means TcO_4^- can be reduced by magnetite. The redox potentials of Tc/siderite samples are even lower, they decrease from −247 mV at pH 8 to −563 mV at pH 11. This confirms the results of batch experiments where the Tc retention by siderite was found to be faster compared to magnetite (not shown).
During IR experiments only the aquatic, hardly sorbed TcO_4^- was observed. In the time frame of the *in situ* IR experiment, the signal of the Tc(VII) ion did not disappear indicating that the reduction to Tc(IV) occurs on a longer time scale.
The XANES spectra (Fig. 2), obtained for magnetite and siderite, are similar (absorption edge 21,058 eV, no pre-edge) to each other, but differ from the XANES spectrum of TcO_4^-. This verifies that the immobilization of Tc onto these minerals is due to surface-mediated reduction of Tc(VII) to Tc(IV). Thus, both minerals contribute to the retention of Tc under repository conditions.
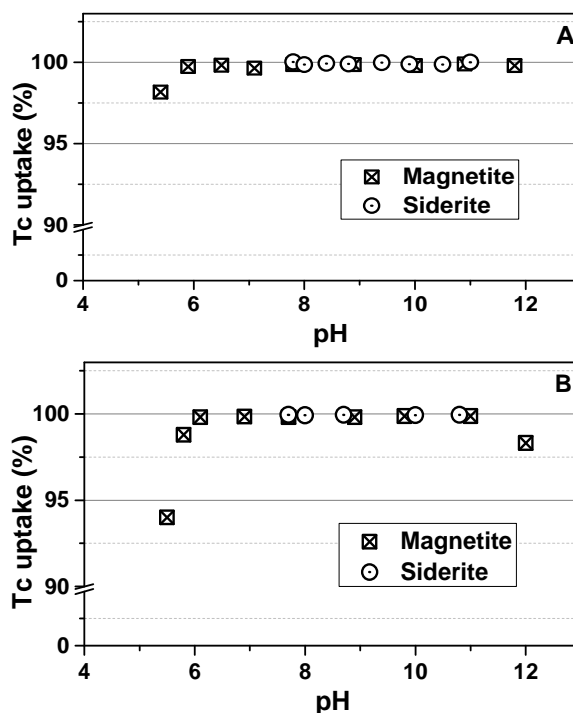
Fig. 1: Tc uptake onto magnetite and siderite as function of pH value in 0.1 M NaCl (A) and 1 M NaCl (B).
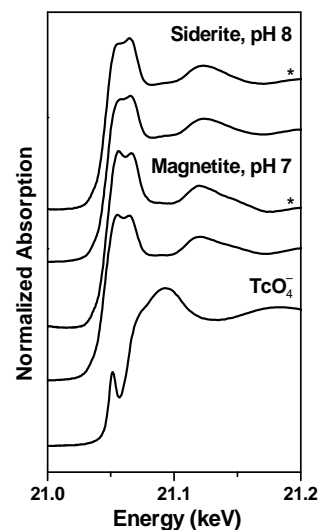
Fig. 2: Tc K-edge XANES spectra of Tc(VII) reacted with siderite and magnetite in comparison to a TcO_4^- reference spectrum (*indicates higher Tc concentration, see experimental section).

[1] Peretyazhko, T. et al. (2012) *Geochim. Cosmochim. Acta* **92**, 48–66.
[2] Kobayashi, T. et al. (2013) *Radiochim. Acta* **101**, 323–332.

Vibrational spectroscopy of the sorption processes of Se(IV) onto γ-alumina

N. Mayordomo,[1] H. Foerstendorf, K. Heim, N. Jordan, C. Franzen

[1]Centro de Investigaciones Energéticas, Medioambientales y Tecnológicas, Madrid, Spain

The sorption reactions of Se(IV) on γ-alumina were investigated by *in situ* IR spectroscopy in the circumneutral pH range. From the spectra significant interactions of Se(IV) and the alumina surface can be deduced suggesting the formation of inner-sphere complexes. Contributions of outer-sphere complexes might have to be considered with increasing pH.

The retention of fission products such as selenium is of major concern for a nuclear waste repository in deep geological formations. The multi-wall barrier concept considers bentonite as a potential backfill material which provides a high retention property necessary for the long-term safety of the repository site. For a reliable risk assessment, the molecular events occurring at the mineral-water interfaces have to be understood in detail. γ-alumina, ubiquitous in the environment and representing a model oxide for more complex aluminosilicates, can serve for spectroscopic investigations of the sorption processes of dissolved fission products. In this work, we present preliminary results of *in situ* IR spectroscopic experiments of the sorption processes of Se(IV)-oxoanions on γ-alumina surface.

EXPERIMENTAL. The set-up and the performance of the in situ experiments are described in detail elsewhere.[1, 2] All experiments were carried in D_2O due to strong background absorption properties of bulk water in the frequency range below $900\ cm^{-1}$.[2]

RESULTS. The spectra of the aqueous solutions predominantly containing the $(HSeO_3^-)_2$ dimer and the SeO_3^{2-} ions are shown in Fig. 1A as black and grey curves, respectively [3]. These spectra serve as references for the spectra of the sorbed species as shown in Fig. 1B. A brief assignment is as follows: in the mid-IR frequency range ($> 600\ cm^{-1}$), two stretching modes are observed, that is the symmetric $\upsilon_1(SeO)$ and the asymmetric $\upsilon_3(SeO)$ modes. The bands of the former mode show up at 851 and $807\ cm^{-1}$ for the $(HSeO_3^-)_2$ dimer and the SeO_3^{2-} ions, respectively. Note that the *in situ* sorption experiments were performed at an initial concentration of $500\ \mu M$ of Se(IV), at which the monomeric $HSeO_3^-$ species are predominant. Nevertheless, only small shifts on the frequency of the υ_1 and υ_3 modes are to be expected compared to the $(HSeO_3^-)_2$ dimer.[3]

The spectra of the sorption species show significantly shifted bands in comparison of the reference spectra evidencing the formation of sorption species at the alumina surface (Fig. 1B). With respect to the predominant aqueous species present at the prevailing pH values, that is the $HSeO_3^-$ ion, the spectra of the sorption species show a significantly bathochromically shifted $\upsilon_{3,as}$ mode at $762\ cm^{-1}$ which is further shifted to $747\ cm^{-1}$ with increasing pH. In contrast, the small band presumably representing the $\upsilon_1(SeO_3)$ mode at $844\ cm^{-1}$ is nearly not shifted but shows reduced intensity with increasing pH.

The formation of inner-sphere (IS) complexes is corroborated by *in situ* IR spectroscopy desorption studies and by classical batch experiments (data not shown). Note that bidentate bridging IS complexes were already identified by means of X-ray Absorption Spectroscopy.[4] A thorough analysis of reference solid compounds in the literature is actually in
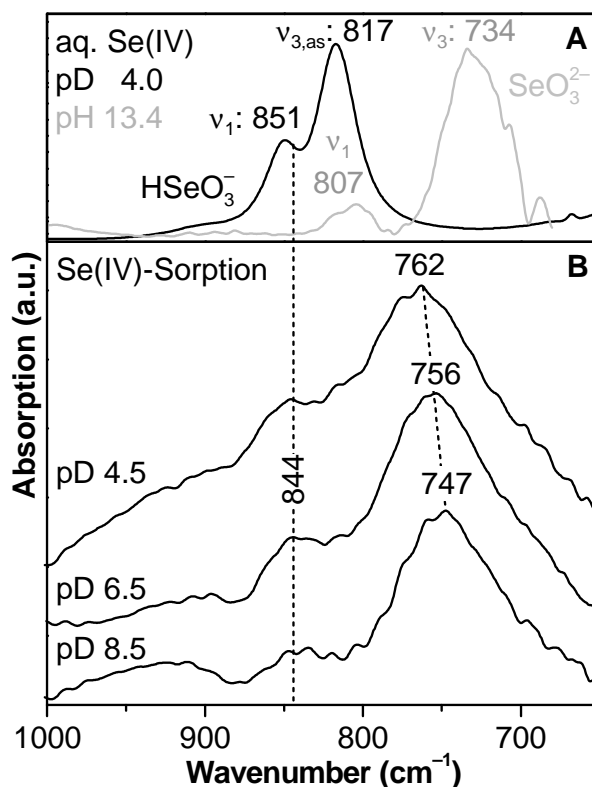
Fig. 1: IR spectra of the $HSeO_3^-$ (0.5 M; black trace) and SeO_3^{2-} ions (0.088 M; grey trace) in aqueous solution (A) and of the in situ sorption Se(IV) species on γ-alumina under inert gas conditions after 60 min of induced sorption (B).

progress to assign/confirm the symmetry of the sorbed surface species.

At pH 8.5, contributions of outer-sphere complexes to the spectrum might have to be considered because the overall shape of the spectra of the sorbed species become more similar to those of the SeO_3^{2-} shown in Fig. 1A. A verification of this assumption by batch experiments is in progress.

In this work we obtained *in situ* spectroscopic information of the sorption reactions of aqueous Se(IV) on alumina surface. This is an important prerequisite for future investigations on the overall retention mechanisms of backfill material, such as bentonite, or onto other mineral phases present on the groundwater. In particular, the competitive reactions in the presence of other main anions, namely bicarbonate, might be decisive for a reliable risk assessment of the setup in the near field of a nuclear waste repository.

[1] Müller, K. et al. (2012) *Geochim. Cosmochim. Acta* **76**, 191–205.
[2] Jordan, N. et al. (2013) *Geochim. Cosmochim. Acta* **103**, 63–75.
[3] Kretzschmar, J. et al. (2015) *Dalton Trans.* **44**, 10508–10515.
[4] Elzinga, E. J. et al. (2009) *J. Colloid Interface Sci.* **340**, 153–159.

Effect of glutamic acid on covellite dissolution

R. Barthen, L. Karimzadeh, M. Gründig, H. Lippold, J. Grenzer,[1] K. Franke, J. Lippmann-Pipke

[1]HZDR, Institute for Ion Beam Physics, Dresden, Germany

Understanding mineral dissolution at neutral pH is crucial for copper winning from ores which exhibit strong acid neutralizing capacities such as Kupferschiefer ores. To identify key parameters we studied the effect of glutamic acid on the dissolution of synthetic covellite. We could show that covellite dissolution induced by glutamic acid is highly pH-dependent and conclude that this is caused by the underlying reaction mechanism.

Bioleaching has become an important method for metal winning in recent years. While much is known about bioleaching with acidophilic bacteria and archaea, knowledge of neutrophilic bioleaching remains scarce. Neutrophilic microorganisms are capable of producing organic acids and metallophores which are able to solubilize valuable metals such as copper. One example of a metal-complexing biomolecule is glutamic acid. This molecule exhibits a high affinity towards copper [1] and can be produced biotechnologically in large quantities. Elucidation of the mechanisms by which organic acids interact with solids such as copper minerals could improve the leaching efficiency for sulfidic Kupferschiefer type ores.

EXPERIMENTAL. CuS was synthesized by a chemical bath deposition method [2]. Crystal structure and stoichiometry were verified by energy dispersive X-ray spectroscopy and scanning electron microscopy. The pH-dependent leaching assays were performed with 10 mL glutamic acid solution (68 mM) and 10 mg CuS. Copper concentration and pH of the supernatant were checked regularly. Experimental results were compared with simulation data obtained with the geochemical modeling tool PHREEQC.

RESULTS. The pH value of the leaching solution is the key factor controlling CuS dissolution by glutamic acid. Increasing the pH of the leaching solution from 6 to 9 increases the copper concentrations by a factor of 5 (Fig. 1).

Copper solubilization is a two-step process: First, covellite dissolves in the aqueous phase (Eq. 1)

$$CuS \rightleftharpoons Cu^{2+} + S^{2-} \qquad (1)$$
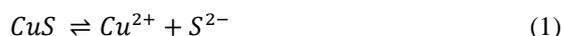
which is followed by the complexation of the copper ion by glutamic acid (Eq. 2).

$$Glu + Cu^{2+} \rightleftharpoons CuGlu + 2H^+ \qquad (2)$$
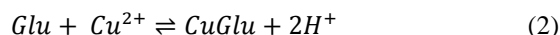
Protons and copper ions compete for the available binding sites at the glutamate molecules. At high pH, the equilibrium is shifted towards the right side, favoring the formation of the copper glutamate complex. The proton released during the complexation could be monitored by a decrease in pH (Fig. 2). Acid generation is most prominent at pH 8, since at pH 9 the higher hydroxyl ion concentration compensates the hydronium ion formation. Our model is able to describe the increase of the copper concentration in the aqueous phase. Further studies have to show if this can be applied to other conditions as well.
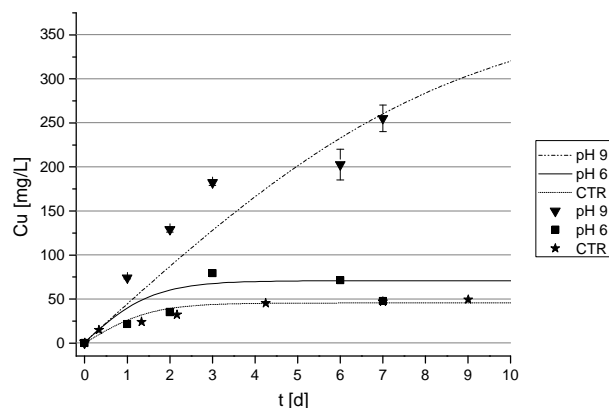
Fig. 1: Copper solubilization as a function of time at different pH. Symbols: experimental results, lines: model simulations.
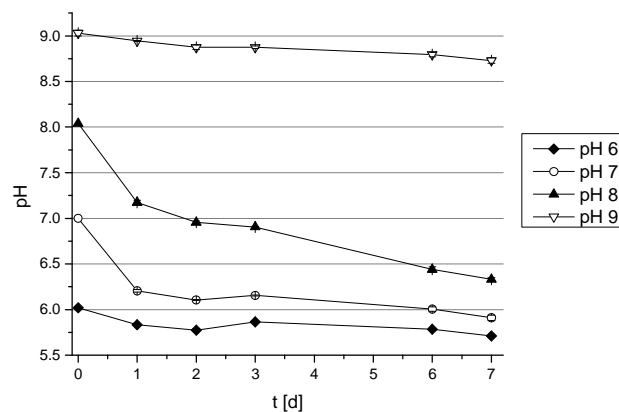
Fig. 2: Acid generation during covellite leaching by glutamic acid at different starting pH values.

[1] Sajadi, S. A. A. (2010) *Nat. Sci.* **2**, 85–90.
[2] Xin, M. et al. (2009) *Appl. Surf. Sci.* **256**, 1436–1442.

Effect of microbial siderophore DFOB on mobility and transport of copper(II) – Column experiments and modelling

L. Karimzadeh, J. Lippmann-Pipke, K. Franke

The effect of the microbial siderophore DFOB on the mobility and transport of copper in the presence of clay mineral is studied in column experiments at pH 6.5. Results show that under experimental conditions DFOB forms copper complexes and increases the metal mobility in the column. Transport of Cu in the column was modelled using the interface COMSOL-PHREEQC, iCP 1.2 [1], according to the one-dimensional advection-reaction-dispersion equation and a surface complexation model (PHREEQC 2.18, [2]).

EXPERIMENTAL. The kaolinite used as the adsorbent was obtained from Sigma-Aldrich Chemie GmbH, Germany. The copper stock solutions was prepared from copper(II) nitrate trihydrated $Cu(NO_3)_2 \cdot 3H_2O$ (Merck, Germany). DFOB is provided from Sigma-Aldrich as mesylate salt and its stock solution prepared at 1.5 mM concentration by dissolving it in distilled water. Experiments were conducted in a glass column with 1 cm of internal diameter and 7.5 cm height. Columns were packed with a homogenous mixture of 2 wt.% kaolinite and 98 wt.% cleaned glass beads (d < 0.5 mm). For column sorption experiments Cu (1.5 mM) and Cu+DFOB (each 1.5 mM) solutions were injected at flowrate of 0.04 mL/min. For desorption experiments columns saturated with Cu (1.5 mM) were flushed with distilled deionized water (DDW) and with DFOB solution, respectively. Finally, Cu concentration of collected effluent samples were analysed by means of ICP-MS (Thermo Scientific ELEMENT XR). A batch sorption experiment was conducted to rule out any significant Cu sorption on the glass beads.

RESULTS. Results reveal that under the experimental conditions DFOB enhances Cu mobility and transport in the column. The Cu breakthrough curves obtained in the column experiments for sorption and desorption are presented in Fig. 1. In the presence of DFOB the breakthrough occurs already after 1.5 pore volumes, whereas in the absence of DFOB the breakthrough occurs only after 2.8 pore volumes. DFOB forms stable and mobile metal complexes and blocks some of the kaolinite sorption edge sites. Therewith it enhances the Cu mobility in the column resulting in a faster appearance of the Cu breakthrough in the effluent. Karimzadeh et al. [3] studied the effect of DFOB on Pb, Zn, and Cd sorption onto zeolite in batch experiments. They found that under neutral and alkaline pH, DFOB decreases metal sorption on zeolite, whereas under acidic conditions DFOB slightly elevated metal sorption.

Furthermore, effect of DFOB on Cu mobility is also reflected in the results of desorption experiments (Fig. 1, right). Flushing the column with DDW (rectangles) leads to a quite abrupt drop of Cu concentration in the eluent, indicating incomplete desorption. Flushing with DFOB (diamonds) mobilizes more Cu from the column. The established geochemical model using log k values from Neubauer et al. [4] well predicts the influence of DFOB on Cu transport in the column. The obtained model results show good agreement with experimental data.

These results are of relevance in respect to microbial bioleaching studies at neutral pH. Successful leaching might
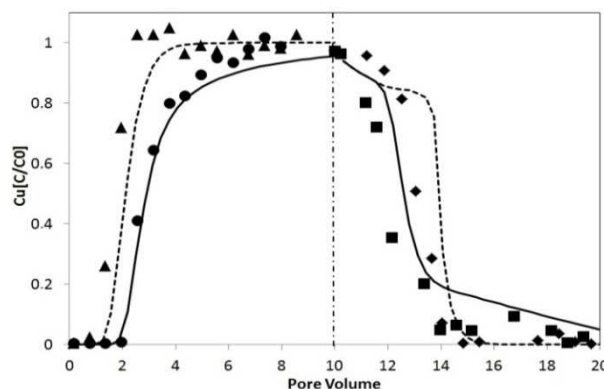
Fig. 1: Cu sorption (left) and desorption breakthrough curves (right). Symbols are experimental results (● 1.5 mM Cu, ▲ 1.5 mM Cu:DFOB in 1:1 ratio, ■ DDW, ♦ 1.5 mM DFOB), and lines are modelled results (solid line: in absence of DFOB, dashed line: in the presence of DFOB).

not necessarily lead to effective Cu removal from the ore, if Cu sorption to abundant mineral or organic surfaces is not effectively reduced. Supply of effective Cu complexing ligands enhancing the Cu mobility may be crucial to successful bioleaching at neutral pH.

[1] Nardi, A. et al. (2014) *Comput. Geosci.* **69**, 10–21.
[2] Parkhurst, L. D. et al. (1999) User's guide to PHREEQC U.S.G.S., Denver, p. 326.
[3] Karimzadeh, L. et al. (2013) *Aquat. Geochem.* **19**, 25–37.
[4] Neubauer, U. et al. (2000) *Environ. Sci. Technol.* **32**, 144–1408.

Modeling the influence of pH on 1D transport of MCPA in an artificial soil matrix

H. Lippold, C. Stuhlfauth,[1] L. Karimzadeh, J. Lippmann-Pipke

[1]Institute of Geosciences, Johannes Gutenberg University Mainz, Germany

MCPA (2-methyl-4-chlorophenoxyacetic acid), one of the most widely used herbicides worldwide, is not considered to be an environmental risk because it "disappears" rapidly in soil. This is mainly attributed to biodegradation, but it might be pretended by sorption processes as well. In the column experiments presented here, mobility of MCPA as a function of pH was investigated for a sand matrix coated with goethite as a reactive soil mineral. In order to examine whether the parameters of a surface complexation model (CD-MUSIC), optimized for the batch system, are compatible with the flow conditions of a dynamic system, the breakthrough curves were modeled on the basis of these parameters by means of the computer programs PHREEQC and iCP.

EXPERIMENTAL. Plexiglass columns (length: 10 cm, ID: 4 cm) were slurry-packed with goethite-coated sand (1 wt% goethite) under a CO_2 atmosphere. Conditioning to the desired pH value was accomplished by passing 10–15 pore volumes of pH-adjusted 0.01 M $NaNO_3$ upward through the packed bed. Breakthrough curves (BTC's) for a continuous step input of MCPA (0.1 mM in 0.01 M $NaNO_3$, pH-adjusted) were recorded at a flow rate of 0.1 mL min^{-1}, measuring the UV absorbance ($\lambda = 279$ nm) of effluent fractions. Hydrodynamic parameters were determined with [^{3}H]H_2O as a non-reactive tracer (0.3 kBq mL^{-1} in 0.01 M $NaNO_3$), using Liquid Scintillation Counting for detection.

Tab. 1: Best-fit parameters of the 1D column system.

Pore water velocity:	3.8×10^{-6} m s^{-1}
Effective porosity:	0.365
Dispersivity:	8.7×10^{-4} m

RESULTS. The influence of pH on the affinity of MCPA towards the goethite surface is reflected by significant differences in retardation (Fig. 1). Breakthrough at pH 3.5 occurs after passage of ~ 2 pore volumes of solvent, whereas at ambient pH, the BTC of MCPA virtually coincides with the BTC of tritiated water. Since the sorption capacity of soil for phenoxy acid herbicides is dominated by Fe oxyhydroxides, it can be concluded that the short half-life of MCPA in subsurface environments is not due to immobilization by sorption but rather attributable to degradation.

From the viewpoint of electrostatic interaction, the decline in adsorption with increasing pH may be readily explained by the progressive reduction of the positive surface charge of goethite (pH$_{PZC}$ > 7) owing to deprotonation of surface hydroxyl groups, counteracting adsorption of the anionic MCPA. However, from the absence of a significant influence of ionic strength, it was inferred that adsorption is not primarily electrostatically driven but dominated by the formation of an inner-sphere complex [1]. Structural information obtained from molecular modeling was used to configure the parameters of the CD-MUSIC model for surface complexation [2]. By fitting the interaction constants, adsorption of MCPA on goethite as a function of pH in batch experiments could be well described [1].

Using the same CD-MUSIC parameters, BTC's of MCPA were modeled on the basis of the one-dimensional (1D) ad-
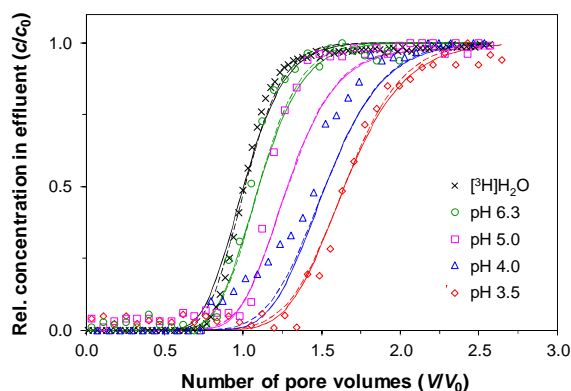
Fig. 1: Breakthrough curves of MCPA for different pH values, obtained in column experiments with goethite-coated sand. Solid and dashed lines show the results of transport modeling based on the computer codes PHREEQC and iCP, respectively.

vection-reaction-dispersion equation for simulating our column experiments. The speciation program PHREEQC [3] was applied to calculate solid-liquid distribution of MCPA in dependence on solution chemistry and concentration of surface sites according to the CD-MUSIC model. Transport calculations were performed in two different ways: (a) using the explicit finite difference scheme included in the PHREEQC program and (b) coupling PHREEQC to the finite elements software COMSOL Multiphysics® using the Java interface iCP [4]. In either case, the column was partitioned into 50 segments. The results of these model calculations are included in Fig. 1.

Positions and slopes of the experimental BTC's can be approximately described by the modeling results based on one uniform parameter set. However, the concentration of sites had to be considerably reduced compared to the known matrix composition, which is indicative of limited accessibility of pore space and/or goethite particle surfaces, possibly caused by preferential flow. Modeled BTC's obtained with both codes (PHREEQC and iCP) are in good agreement with each other, demonstrating the correct configuration of iCP. Spatially resolved investigations by Positron Emission Tomography, accompanied with 2D modeling by iCP, will unveil the actual flow pattern and provide explanations for the discrepancy between measured and effective site density.

[1] Kersten, M. et al. (2014) *Environ. Sci. Technol.* **48**, 11803–11810.
[2] Hiemstra, T. et al. (1996) *J. Colloid Interface Sci.* **179**, 488–508.
[3] Parkhurst, D. L. et al. (2013) in: *US Geological Survey Techniques and Methods*, Book 6, Chapter A43, Denver, CO.
[4] Nardi, A. et al. (2014) *Comput. Geosci.* **69**, 10–21.

PET imaging of carbon nanotube transport

S. Schymura, J. Kulenkampff, K. Franke, J. Lippmann-Pipke

Transport of a concentrated carbon nanotube (CNT) dispersion through porous media was imaged using positron emission tomography (PET). The *in situ* visualization of nanotube transport reveals sedimentation effects causing a pronounced initial deposition of the CNTs around the column inlet.

EXPERIMENTAL. 5 mg of oxidized multi-wall carbon nanotubes (MWCNT, IoLitec, Germany) in 5 mL phosphate buffered water at pH 6 were radiolabeled with I-124 by reaction in an Iodogen-coated centrifuge vial for 4 h in an ultrasonic bath in the dark [1,2]. After washing with distilled water 5 mL of a 1 mg/mL MWCNT dispersion in distilled water, produced by ultrasound treatment, was used in PET transport experiments [3]. The particle dispersion was injected into a 4 cm x 9 cm glass column filled with 3 mm glass beads at a flow rate of 0.1 mL/min. Additionally an experiment using [F-18]KF as a conservative tracer was conducted.

RESULTS. Upon injection of the nanotube dispersion the MWCNTs remain in the column for a very long time (Fig. 1, red squares) while the conservative tracer breaks through after about 350 min (Fig. 1, open symbols). Still, also the conservative tracer does not elute quantitatively. From PET imaging we learn about the fate of the remaining amounts of tracer inside the column. Immediately after injection in both experiments the activity spreads over the whole lowermost cross section of the column, but only the conservative tracer ascends through the column (not shown), according to the flow rate. In contrast the MWCNTs largely deposit at the bottom and do not move any further. Figure 2 shows the spatial distribution of the remaining conservative tracer and the MWCNT at t ~ 350 min. The remaining conservative tracer has accumulated in the least flushed corners at the base of the column (*left*), while the MWCNT dispersion has remained all across the base of the column (*right*). Only after a very long leaching period of several days eventually 76% of the MWCNTs leave the column while 24% remain deposited at the column bottom.

Under the experimental conditions strong negative surface potentials should inhibit interaction between particles and matrix (Tab. 1.). Filtration of well dispersed MWCNTs is unlikely due to the large grain size of the glass beads. Consequently the observed effects are attributed to sedimentation and hydrodynamic deposition effects. In the course of multiple days slow dismantling of the deposited aggregates by continuous gentle shear flow could cause continuous leaching and eventual transport of the majority of CNTs.

[1] Deng, X. et al. (2008) *Nanotechnology* **19**, 075101.
[2] Franke, K. et al. (2010) *Radiochim. Acta* **98**, 333–339.
[3] Schymura, S. et al. (2016) in preparation.
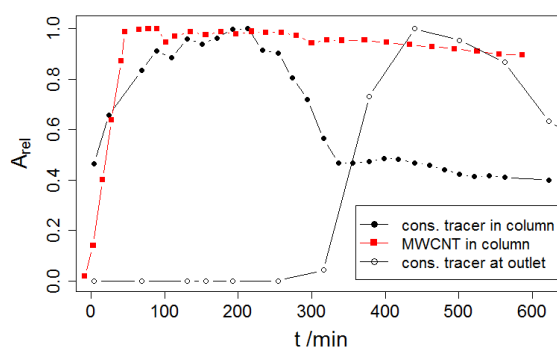
Fig.1: Relative total activities of the conservative tracer and CNTs as measured by PET in the column and relative total activity of the conservative tracer at the outlet as measured by a flow-through counter. All referred to the corresponding maximum value.
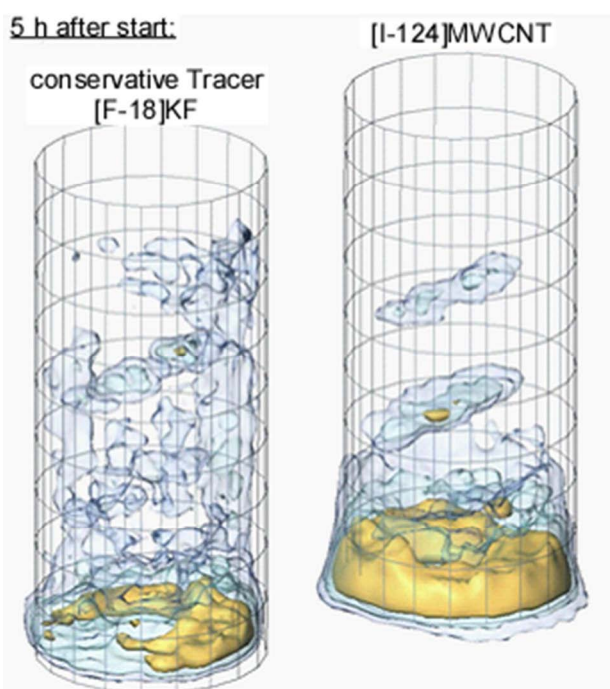
Fig.2: PET-images of the tracer distribution at t ~ 350 min (breakthrough of the conservative tracer) for the conservative experiment (left) and the MWCNT transport experiment (right), respectively. At this time about 50% of the conservative tracer had left the column, while the total activity of the CNTs remains constant (Fig. 1).

Tab. 1: ζ-potential of nanoparticles and matrix at the experimental conditions of the PET experiment as measured by electrophoretic light scattering.

Material	ζ-potential
MWCNT	−41.6 mV
Glass matrix	−50.3 mV

Developing

THERMODYNAMIC
DATABASES

Comparison of different estimation methods for temperature correction of $\log_{10} K$ for the aqueous systems U(VI)–SO_4^{2-} and U(VI)–CO_3^{2-}

C. Franzen, K. Müller, R. Steudtner, V. Brendler

Two different second-law extrapolations for the calculation of the equilibrium constants at different temperatures within a range of 273 to 371 K are assessed with respect to applicability.

The temperature dependence of the $\log_{10}K$ value of any reaction can be calculated if the following thermodynamic parameters are known: $\log_{10}K°$; $\Delta_r S°$; $\Delta_r H°$; and the temperature dependence of $\Delta_r C_p°$. However, there is still a lack of reliable thermodynamic data for most actinide hydrolysis products and complexes with inorganic ligands, e. g. SO_4^{2-} or CO_3^{2-}, in particular for polymeric complexes. Theoretical approximations may be helpful to estimate $\log_{10}K$ values at temperatures other than T_0.

EXPERIMENTAL. The simplest assumption is that $\Delta_r C_p^{\ominus}$ is zero at all temperatures, *i. e.* a constant enthalpy of reaction. In this case, the integrated van't Hoff expression is used for calculations.

$$log_{10}K(T) = log_{10}K° + \frac{\Delta_r H°_m}{Rln(10)}\left(\frac{1}{T_0} - \frac{1}{T}\right) \quad (1)$$

For a temperature difference $(T-T_0)$ equal or less than 10 K, the error introduced in $\log_{10}K(T)$ by this simplification will be well within its uncertainty limits [1].

In cases where the extrapolation extends over a temperature range larger than about 10 K, several other approaches are available, where $\Delta_r C_p°$ is assumed to not vary with temperature [1]. In order to compare the integrated van't Hoff expression with a more complex model we chose the Ryzhenko–Bryzgalin model (RBM). As can be seen in Eq. 2, this approximation includes more parameters, which are specific for the corresponding complexes. More details concerning this model can be found in literature [2].

$$log_{10}K(T,p) = \frac{T_0}{T}log_{10}K°$$
$$+ \frac{|Z_a Z_c|_{eff}}{r_{eff}}\frac{N_A e^2}{4\pi\epsilon_\circ RTln(10)}\left(\frac{1}{\varepsilon(T,p)}\right.$$
$$\left. - \frac{1}{\varepsilon(T_0,p°)}\right) - \sum_i v_i log_{10}\rho(T,p) \quad (2)$$

RESULTS. The estimations based on the integrated van't Hoff expression and the RBM for the systems UO_2^{2+}–SO_4^{2-} and UO_2^{2+}–CO_3^{2-} are shown in Fig. 1 and 2, respectively. Values for $\log_{10}K(298 \text{ K})$ used for calculations are taken from literature [3]. For the UO_2^{2+}–SO_4^{2-} system, both models show an increase of $\log_{10}K$ with increasing temperature for both the 1 : 1 and the 1 : 2 complex. However, at the lowest and highest temperatures, the RBM gives slightly higher values than van't Hoff.

Concerning the UO_2^{2+}–CO_3^{2-} system, the RBM shows higher values at low temperatures and lower values for high temperatures compared to van't Hoff. For the 1 : 3 complex both models predict the trend of a decreasing $\log_{10}K$ with increasing temperatures. For the 1 : 1 and 1 : 2 complexes, however, the models are contradictory. Namely, RBM yields decreasing $\log_{10}K$ values with increasing temperatures, whereas van't Hoff predicts increasing $\log_{10}K$ values
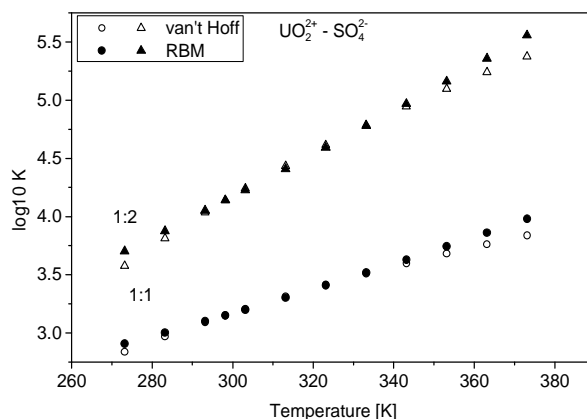
Fig. 1: $\log K(T)$ in the system U(VI)–SO_4^{2-} calculated with integrated van't Hoff and RBM..
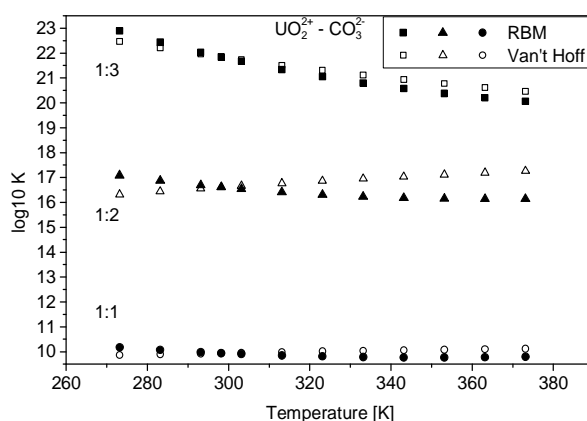
Fig. 2: $\log K(T)$ in the system U(VI)–CO_3^{2-} calculated with integrated van't Hoff and RBM.

for the 1 : 2 complex and turns back to a nearly temperature-independent pattern for the 1 : 1 complex.

Second-law extrapolations must be used with caution in the absence of experimental heat capacities. Additionally, when fitting high T equilibrium constants, more than one equation should be tested and compared. In order to get more reliable data, experimental measurements should be performed in order to determine equilibrium constants at different temperatures for various representative systems.

[1] Puigdomènech, I. et al. (1999) NEA-TDB-4 Guideline.
[2] Ryzhenko, B. N. et al. (1991) *Geochem. Int.* **28**, 77–83.
[3] Guillaumont, R. et al. (2003) *Update on the chemical thermodynamics of U, Np, Pu, Am and Tc.* Elsevier, Amsterdam..

How to handle activity coefficients of weak complexes in thermodynamic databases: a case study

N. Jordan, K. Spahiu[1]

[1]Swedish Nuclear Fuel and Waste Management Co (SKB), Stockholm, Sweden

A procedure to handle the $\log \beta$ of weak complexes in thermodynamic databases (TDB) is described here. It consists in extrapolating data obtained at constant ionic strength and in mixed electrolytes (e.g. $HClO_4$ and HNO_3) to the pure background electrolyte media (perchlorate), i.e. at trace ligand (NO_3^-) concentration. The obtained equilibrium constants can subsequently be extrapolated to zero ionic strength using, e.g., the Specific Ion Interaction Theory (SIT) approach.

The performance assessments of radioactive waste disposals as well as the optimization of technological processes to access critical raw materials rely on the accuracy of the physico-chemical parameters compiled in TDB (enthalpy, free Gibbs energy, etc.).

Most of the stability constants β published in the literature were obtained via the "ionic medium method", by using an inert electrolyte (classically from 0.01 to 4 M) at a concentration orders of magnitude higher than those of the involved reactants and products. Thus the activity coefficients (γ) of the reacting species remain reasonably constant during the measurements.

To express the activity coefficients in high ionic strength (I) medium, the Nuclear Energy Agency [1] recommended the use of the SIT theory:

$$\log_{10} \gamma_i = -z_i^2 \frac{A\sqrt{I}}{1+1.5\sqrt{I}} + \sum_j \varepsilon(i,j,I) \cdot m_j \qquad (1)$$

with z_i being the charge of the ion, A an empirical Debye–Hückel parameter, m the molality and $\varepsilon(i,j)$ ion-ion interaction coefficients. According to (1), γ are depending on the ionic strength as well as the composition of the media.

In the case of weak complexes, to maintain the ionic strength constant, it is sometimes necessary to increase the ligand concentration up to a full replacement of the ions of the background electrolyte. Unfortunately, numerous studies assumed that keeping constant the ionic strength ensures the constancy of the activity coefficients, which is not always valid at high ionic strength.

Hence, Spahiu et al. [2] proposed to use as a reference state the pure background electrolyte (e.g. $HClO_4$) at an ionic strength I, in order to obtain an expression for activity coefficient changes in mixtures (e.g. $HClO_4$–HNO_3) at the same ionic strength.

We will exemplarily apply this methodology to the study of Khopkar et al. [3], who investigated the complexation of Eu(III) by NO_3^- by solvent extraction (dinonylnaphthalene sulphonic acid in n-hexane) at 30 °C. The composition of the aqueous phase was 1 M H^+, $[NO_3^-] = 0$ to 1.0 M and $[ClO_4^-] = 1 - [NO_3^-]$ M. The concentration of $DNNS^-$ in the organic phase was held constant.

RESULTS. Khopkar et al. reported $\beta_1 = 1.80 \pm 0.03$ for the formation of $EuNO_3^{2+}$ [3]. Changes in the activity coefficients were not considered. Using the methodology of Spahiu et al., the following equation is obtained:

$$\frac{D_0}{D} = \left[10^{a \times [NO_3^-]} + \beta_1'[NO_3^-]10^{c \times [NO_3^-]} \right] \qquad (2)$$

with D_o and D being the distribution coefficient of Eu(III) without and with nitrate, respectively, a = 0.11 and c = 0.05
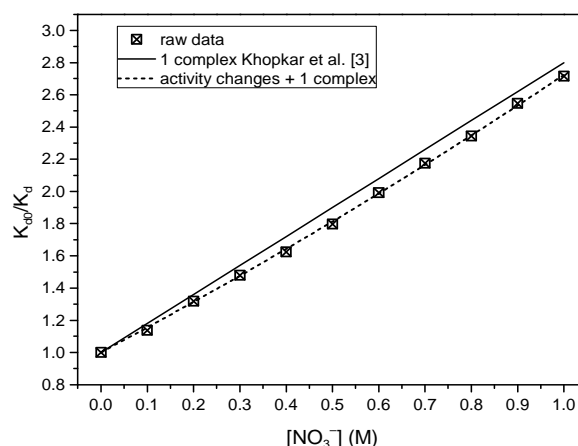
Fig. 1: Experimental data from Khopkar et al. [3] plotted against the concentration of NO_3^-. The black line corresponds to the original paper, with the formation of $EuNO_3^{2+}$ but no consideration of γ changes. The dotted line was recalculated in this work by additionally considering changes in activity coefficients.

constant parameters depending on the ion-ion interaction coefficients of Eu^{3+}, H^+ and $EuNO_3^{2+}$ and β_1' the formation constant of $EuNO_3^{2+}$ in pure $HClO_4$. After fitting the experimental data with equation given in (2), $\beta_1' = 1.28$ was obtained. This results in a better fit than Khopkar et al. (Fig. 1).

This methodology enables to account for changes in the composition of the ionic medium and to treat variation in the activity coefficient in a satisfactory way. It thus allows determining a complexation constant at constant ionic strength in "pure" ionic media and trace concentration of the ligand. It enables (a) to obtain a consistent set of data and (b) to discard weak high-order complexes having no independent spectroscopic validation. Finally, the complexation constants at trace ligand concentration can be extrapolated to zero ionic strength using the SIT equation. Obviously, this procedure can be applied to other weak complexing ligands such as sulfate and chloride.

[1] Lemire, R. J. et al. (2013) *Chemical thermodynamics of Iron Vol. 13a*, Elsevier Science Publishers B. V., Amsterdam.
[2] Spahiu, K. et al. (1998) *Radiochim. Acta* **82**, 413–419.
[3] Khopkar, P. K. et al. (1971) *J. Inorg. Nucl. Chem.* **33**, 495–502.

Thermodynamic reference database THEREDA: 6. Oxygen solubility in water and brines

F. Bok

Dissolved oxygen influences the chemistry of various radionuclides in the aqueous solution. In the presence of dissolved oxygen, the poorly soluble (hydro-) oxides of reduced radionuclides, *e.g.* U(OH)$_4$(am), PuO$_2$(am/cr) get oxidized and the radionuclides become more soluble in water. A consistent set of Pitzer ion-ion-interaction coefficients was deduced for the calculation of the amount of dissolved oxygen in aqueous solution and brines with high salinity.

The Pitzer approach can be used for the calculation of the activity coefficient of dissolved oxygen in highly saline solutions [1]. Already published datasets containing ion-ion-interaction coefficients for O$_2$ in salt solutions [2–4] are not consistent with the THEREDA database [5]. Combining them would not reproduce experimental O$_2$ solubility data. Therefore, a new set of interaction coefficients for dissolved O$_2$ in salt solutions had to be created consistent to the already established THEREDA dataset.

FITTING PROCEDURE. Experimental solubility data for oxygen in water and binary as well as some ternary salt solutions were taken from ~100 references. All solubility data were recalculated to µmolal scale as a function of molal salt concentration and temperature.

Pitzer interaction coefficients $\lambda_{O_2\text{-}c}$, $\lambda_{O_2\text{-}a}$, $\xi_{O_2\text{-}c\text{-}a}$, $\xi_{O_2\text{-}c\text{-}c'}$, and $\xi_{O_2\text{-}a\text{-}a'}$ (c = cation, a = anion) have been determined using the geochemical speciation software PHREEQC (batch version 3.1.7-9213) [6] coupled with the parameter estimation software UCODE-2005 [7].

First, the Pitzer interaction coefficients for 25 °C were deduced. There, all binary mixtures of the alkali chloride systems (Na$^+$, K$^+$, H$^+$ / Cl$^-$, OH$^-$ - H$_2$O) were fitted simultaneously to obtain the respective Pitzer interaction coefficients. As an initial coefficient $\lambda_{O_2\text{-}Cl^-}$ was set to zero. The obtained coefficients were then used as boundary conditions for the fitting of the alkaline sulfate (Na$^+$, K$^+$, H$^+$ / SO$_4$$^{2-}$, OH$^-$ - H$_2$O), alkali carbonate (Na$^+$, K$^+$ / CO$_3$$^{2-}$ - H$_2$O), alkali phosphate (Na$^+$, K$^+$, H$^+$ / H$_n$PO$_4$$^{3-n}$ - H$_2$O) systems, for binary solutions of CaCl$_2$, MgCl$_2$, MgSO$_4$, and ternary solutions containing Na$^+$ and Mg^{2+} as well as Cl$^-$ and SO$_4$$^{2-}$.

For the alkali and alkaline earth chloride and sulfate systems oxygen solubility data at various temperatures are available. To take the temperature dependency of the O$_2$ solubility into account, the parameters of the PHREEQC temperature function of the Pitzer interaction coefficients were deduced directly by equation (1), where P is the coefficient (λ or ξ), T is the temperature in Kelvin, T_r is the reference temperature (298.15 K), and ln is the natural logarithm. This temperature function is compatible with all common speciation codes. The previously obtained interaction coefficients at 25 °C were used as A$_0$ parameter.

$$P = A + A_1 \left(\frac{1}{T} - \frac{1}{T_r}\right) + A_2 \, ln\left(\frac{T}{T_r}\right) + A_3(T - T_r) +$$
$$A_4(T^2 - T_r^2) + A_5\left(\frac{1}{T} - \frac{1}{T_r}\right) \tag{1}$$

It was found that only the parameters A$_1$ and A$_2$ are necessary to describe the temperature dependency of the O$_2$ solubility in salt solutions, all others can be set to zero.
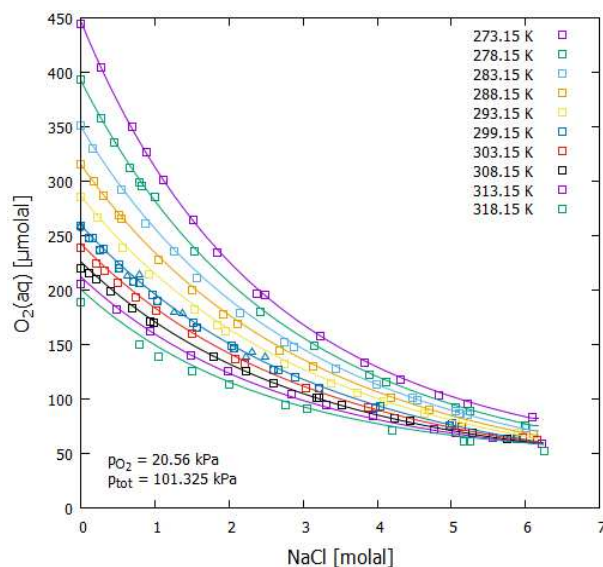
Fig. 1: O$_2$ solubility in NaCl solutions at different temperatures (□ experimental values from [3], ─ calculations using this work).

RESULTS. A self-consistent set of Pitzer interaction coefficients for the description of oxygen solubility in binary and some ternary salt solutions could be obtained for the system Na$^+$, K$^+$, H$^+$, Ca^{2+}, Mg^{2+} / Cl$^-$, SO$_4$$^{2-}$, CO$_3$$^{2-}$, PO$_4$$^{3-}$, OH$^-$ - H$_2$O including the corresponding acids and hydroxides.

For the chloride and the sulfate subsystems, temperature function parameters could be obtained to describe the temperature dependency of the O$_2$ solubility in these salt solutions. An example is given in Fig. 1 showing the O$_2$ saturation in NaCl solution as function of ionic strength and temperature.

[1] Pitzer, K. S. (1991) *Ion interaction approach: theory and data correlation, Activity coefficients in electrolyte solutions*, CRC Press, Boca Raton, Florida.
[2] Clegg, S. et al. (1990) *Geochim. Cosmochim. Acta* **54**, 3315–3328.
[3] Millero, F. J. et al. (2002) *Mar. Chem.* **78**, 217–230.
[4] Geng, M. et al. (2010) *Geochim. Cosmochim. Acta* **74**, 5631–5640.
[5] THEREDA – Thermodynamic Reference Database (http://www.thereda.de).
[6] Parkhurst, D. L. et al. (2013) *Description of Input and Examples for PHREEQC Version 3—A Computer Program for Speciation, Batch-Reaction, One-Dimensional Transport, and Inverse Geochemical Calculations*, U.S. Geological Survey, Denver, Colorado.
[7] Poeter, E. P. et al. (2008) *UCODE_2005 and Six Other Computer Codes for Universal Sensitivity Analysis, Calibration, and Uncertainty Evaluation*, U.S. Geological Survey, Reston, Virginia.

Multidimensional "smart Kd-matrices": americium(III) and neptunium(V)

M. Stockmann, V. Brendler, J. Flügge,[1] U. Noseck[1]

[1]Gesellschaft für Anlagen- und Reaktorsicherheit (GRS) gGmbH, Brunswick, Germany

In the framework of the WEIMAR project, the smart K_d-concept [1] was extended towards a more realistic description of sorption processes and radionuclide migration in the existing transport program r³t [2]. So far, the pH, the ionic strength (IS) and the concentrations of dissolved inorganic carbon [DIC], [Ca] and radionuclides [RN] were considered and varied according to field site conditions of the Gorleben site. In this article, recent results for smart K_d-distributions of Am(III) and Np(V) are presented.

Pre-calculated smart K_d–values and their resulting total variance can be described by frequency distribution functions. In Fig. 1a/b histograms are shown for americium(III) and neptunium(V) based on replicated Latin-Hypercube Sampling (rLHS) with a sampling size of 20,000 samples. It is obvious that using only a mean K_d-value (blue line in Fig. 1) would not be suitable, and the distribution is not even a Gaussian. Both observations strongly support that the full range of the calculated K_d-values must be taken into consideration for reactive transport calculations. Moreover, the constant K_d-values used so far [3] are not conservative and must be replaced in certain cases (here for Np(V)) by the minimum values (red lines in Fig. 1) when considering worst-case scenarios.

In Fig. 2a,b, 3-D subsets from the pre-calculated 5-D smart K_d-matrices for Am(III) and Np(V) are illustrated. The subsets only show the K_d-variability caused by pH (in the range of 6 to 9), of [Ca] and IS, thereby ignoring the effects of [DIC] and [RN]. However, pH and [DIC] are correlated (not
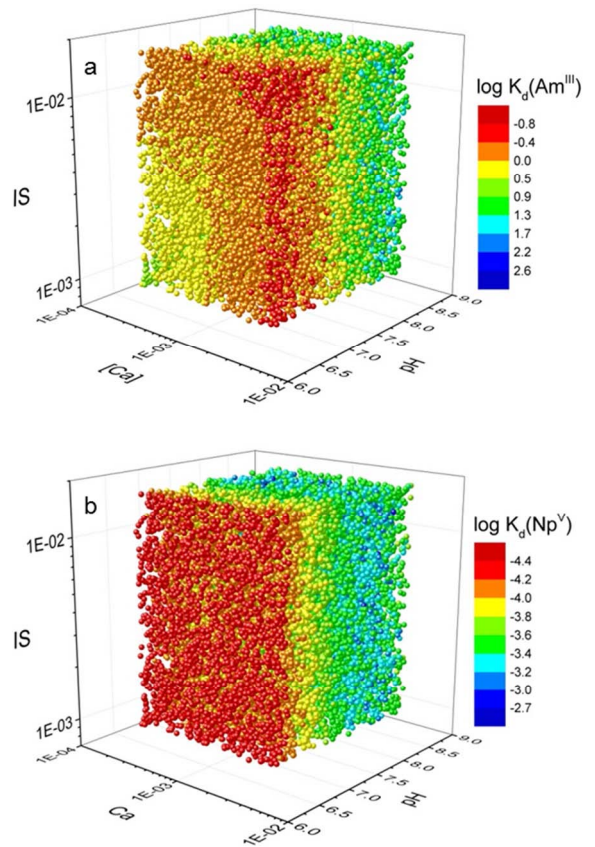
Fig. 2: 3-D subsets from 5-D smart K_d-matrices for Am(III) (a) and Np(V) (b) (K_d in m³/kg).

shown here). The correlation factor R = 0.8 is estimated from fundamental data (valid assumption) combined with on-site data. In general, it is clearly visible, that the pH mainly influences the sorption: the K_d increases with rising pH until the sorption maximum and then decreases again. In the case of Am(III), also combined effects are visible depending on both the Ca content and the IS.

[1] Noseck, U. et al. (2012) *Report GRS-297*.
[2] Fein, E. (2004) *GRS-Report 192*.
[3] Suter, D. et al. (1998) *Proceedings DisTec 98*.

Fig. 1: Histograms of 20,000 pre-calculated log K_d values based on rLHS for Am(III) (a), and Np(V) (b).

Long-Lived Radionuclides in

BIOLOGICAL
SYSTEMS

pH-dependent Pu interaction of one bacterial isolate from Mont Terri Opalinus Clay

H. Moll, A. Cherkouk

Sporomusa sp. **MT-2.99 cells displayed a strong pH dependent affinity for Pu. Relatively high maximal Pu loadings as for instance 230 mgPu/g$_{dry\ biomass}$ for *Sporomusa sp.* at pH 6.1 were achieved. A much slower abiotic reduction of Pu(VI) was observed at pH 4 compared to pH 6.1. Independent on pH an enrichment of Pu(V) in the supernatant and of Pu(IV)-polymers on the biomass was discovered.**

In this study, our first experiments reported in [1] could be extended to a broader pH range. The performed experiments help to get a more comprehensive overview of the interaction potential of one of our bacterial isolates namely *Sporomusa sp.* MT-2.99 from Mont Terri Opalinus Clay [2], towards plutonium. Here no electron donor was added where biosorption is favored.

EXPERIMENTAL. *Sporomusa sp.* MT-2.99 cells were cultured anaerobically in R2A medium at 30°C. Cells were harvested in the mid-exponential growth phase, washed and suspended in 0.9% NaCl solution containing 100 µM Na-pyruvate. The experiments were performed anaerobically at [dry biomass] of 0.33 ± 0.01 g$_{dry\ weight}$/L and pH values of 3, 4, 6.1 and 7 at 25 °C in 0.1 M NaClO$_4$. [^{242}Pu]$_{initial}$ was varied between 0.2 and 110 mg/L. The ^{242}Pu present in blank, supernatant, and washed biomass suspension at pH 0 was analyzed using solvent extraction, and LSC as described in [3].

RESULTS. *Sporomusa sp.* cells display a strong pH dependent affinity for Pu (see Fig. 1A). At pH 3, only 13% of the initial Pu was accumulated, whereas 90% were associated with the biomass at pH 7.
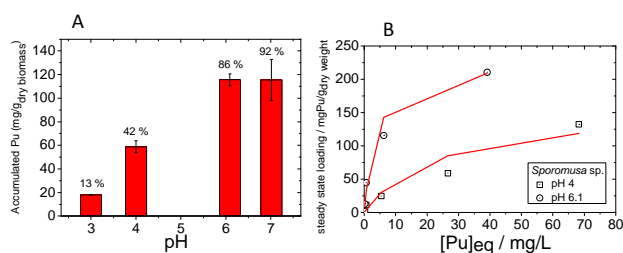
Fig. 1: Biosorption of Pu on *Sporomusa sp.* MT-2.99 at [^{242}Pu]$_{initial}$: 45 mg/L in 0.1 M NaClO$_4$ as a function of pH under steady state conditions (A). Langmuir isotherms obtained in the *Sporomusa sp.* system (B).

The biosorption of Pu was evaluated using the Langmuir absorption isotherm model. The application of the Langmuir-isotherm model in order to describe the biosorption of heavy metals in biological systems was reported for instance in [4]. As depicted in Fig. 1B the Langmuir model could describe the experimental data with a reasonable quality. The sorption experiments showed that *Sporomosa sp.* cells are more effective in removing Pu from the surrounding solution compared to *Paenibacillus sp.* (data not shown). This effect is more pronounced at longer contact times. At pH 6.1 the maximal Pu loading on *Sporomusa sp.* cells was calculated to be 230 mgPu/g. It was reported that aerobic soil bacteria accumulated ca. 45 mgPu/g$_{dry\ weight}$ [5]. This concludes that *Sporomusa sp.* accumulated relatively high amounts of Pu.
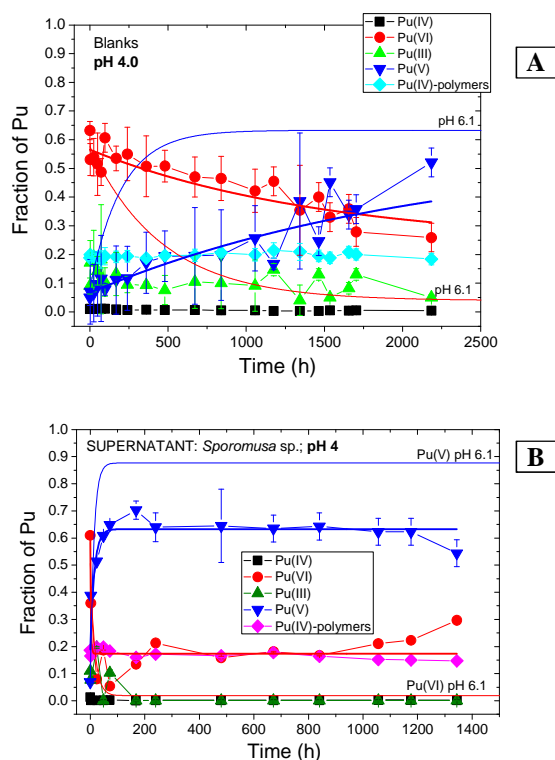
Fig. 2: ^{242}Pu oxidation state distributions determined by solvent extraction as a function of the incubation time ([^{242}Pu]$_{initial}$: 108 ± 5 mg/L, 0.1 M NaClO$_4$, pH 4). Blank samples (A) and supernatants in the *Sporomusa sp.* system (B).

In the beginning, the dominating Pu species are Pu(VI) ($58 \pm 7\%$) Pu(IV)-polymers ($19 \pm 1\%$), and Pu(III) ($13 \pm 6\%$, see Fig. 2A). The decrease of Pu(VI) at pH 6.1 is 3.2 times faster than at pH 4. The increase of Pu(V) at pH 6.1 is 3.3 times faster than at pH 4. It follows that a more acidic pH stabilizes Pu(VI). A significant change of the Pu oxidation state distributions was observed in the supernatants (see Fig. 2B for *Sporomusa sp.*). At both pH values a fast decrease of Pu(VI) combined with a fast increase of Pu(V) was observed. At pH 4 the enrichment of Pu(V) was less strong and also higher remaining Pu(VI) concentrations in the supernatants were measured. This might indicate a lower reducing impact of the cells at pH 4. The observed bioreduction process of Pu(VI) to Pu(V) by cells of *Sporomusa sp.* and *Paenibacillus sp.* [1] is not yet fully understood. No differences were observed regarding the Pu oxidation state distributions in the acidified biomass suspensions if no electron donor was previously added. The major Pu oxidation state was Pu(IV)-polymers with an average amount of 42%.

[1] Moll, H. et al. (2015) *Report HZDR-059*, p. 12.
[2] Bachvarova, V. (2009) *Report FZD-530*, p. 18.
[3] Moll, H. et al. (2006) *Radiochim. Acta* **94**, 815–824.
[4] Klimmek, S. (2003) *Charakterisierung der Biosorption von Schwermetallen an Algen*. PhD thesis, TU Berlin.
[5] Panak, P. J., Nitsche, H. (2001) *Radiochim. Acta* **89**, 499–504.

Cultivation, preparation and characterization of *Sporosarcina ureae* biomass for metal sensor and actor materials

M. Vogel, S. Matys,[1] J. Raff

[1]Helmholtz Institute Freiberg for Resource Technology, Freiberg, Germany

***Sporosarcina ureae* cells were successfully cultivated in technical scale with a biomass yield of 300 g wet weight per cultivation. This biomass amount was appropriate for preparation of 1.5 g dry weight cell surface-layer proteins. The specific and unspecific binding behavior of these proteins towards rare earth elements and heavy metals was proven, respectively.**

The presented work is part of the project BIONEWS dealing with long-term stable cells for the development of sensor and actor materials for strategic relevant metals, in particular rare earth elements (REE). *Sporosarcina ureae* cells were chosen as potential biomass as they possess surface-layer proteins as outermost cell envelope which should be able to specifically bind REE. Additionally, these spore-forming cells can be cultivated under selective conditions in presence of high amounts of urea. All these properties are important for function and regeneration of the novel sensor and actor materials based on living cells. But in a first step the surface-layer proteins alone as interacting part of the cells should be isolated and characterized regarding metal binding behavior in the desired pH range (≤ 4) and at low metal concentrations.

EXPERIMENTAL. *Sporosarcina ureae* ATCC 13881 was cultivated in Mast-medium at pH 8 in Erlenmeyer flasks, in 5 L and in 70 L bioreactor under stirring at 30 °C. For preparation of surface-layer proteins cells were harvested at the end of exponential growth phase, re-suspended in buffer and proteins were isolated according to the protocol in reference [1]. Molecular mass of the protein was determined by SDS-PAGE. Functionality was checked through recrystallization on polyelectrolyte coated SiO_2 wafer by AFM.
The isolated proteins (1 g/L) were tested for their metal binding behavior using 100 µM metal salt solutions (Eu, Tb, Y, Au, U) at different pH values between 3 and 4.5. After 24 h, remaining metal contents in protein free solutions (separated with centrifugal filter units) was measured by ICP-MS.

RESULTS. Cultivation of *Sporosarcina ureae* cells in Mast-medium was successful also after an up-scaling to a 70 L bioreactor. So, with a single cultivation about 300 g (wet weight) biomass was obtained. This biomass was sufficient to isolate about 1.5 g (dry weight) of surface-layer proteins.
The isolated surface-layer protein of *S. ureae* was identified by SDS-PAGE and recrystallization on technical surfaces. SDS-PAGE revealed a molecular weight of 116 kDa which is in agreement with literature values [2]. The functionality of the surface-layer protein could be demonstrated by formation of the protein lattice on a polyelectrolyte-modified SiO_2-wafer. The lattice showed p4-symmetry as described previously [2].
The results of metal sorption by these surface-layer proteins in pH range 3 to 4.5 are given in Fig. 1. As can be seen, the tested REE are bound in comparable amounts with a sorption optimum around pH 3.5. The 4 to 5 mol REE/mol protein correspond to 45% of the initially applied REE concentration. For Au and U there is a slight increase in sorbed
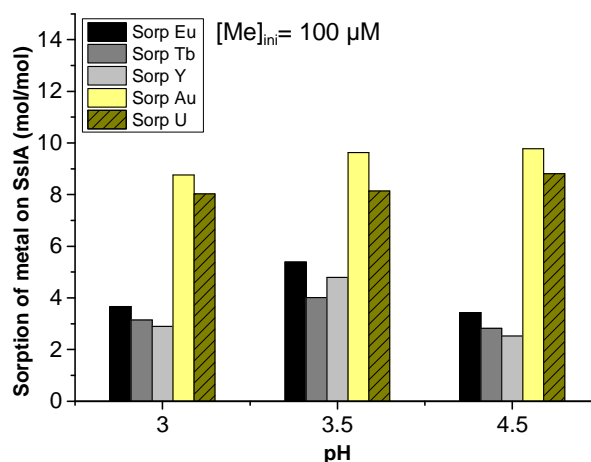
Fig. 1: Metal sorption by *Sporosarcina ureae* surface-layer protein.

metal per mol protein with rising pH from 9 to 10 and 8 to 9 mol metal/mol protein, respectively. At pH 4.5, 100% of the applied Au and 85% of the applied U was bound.
The observed differences in heavy metal and REE binding can be explained with different binding mechanisms: first of all, the improved heavy metal sorption with increasing pH could be explained by an increasing amount of deprotonated functional groups which are involved in unspecific binding. In contrast to that, REE are expected to bind specifically to the Ca-binding sites in the protein replacing Ca.
With single metal solutions *S. ureae* surface-layer shows similar sorption behavior as known from *Lysinibacillus sphaericus* surface-layer proteins. There were also first experiments with industrial waters containing REE and heavy metals which indicated that the proteins possess a preferred binding affinity to REE over heavy metals. This selectivity and the required conditions need to be further investigated. Nevertheless, the obtained results are promising and it can be stated that the surface-layer proteins of *S. ureae* can be applied for the development of single-use sensor and actor materials to proof the functionality concepts before the operating mode will be transferred to the complex system of living cells.

[1] Raff, J. et al. (2003) *Chem. Mater.* **15**, 240–244.
[2] Engelhardt, H. et al. (1986) *J. Bacteriol.* **168**, 309–317.

Proof of U(VI) sorption on *Acidovorax facilis* by TRLFS and EF-TEM/EELS

E. Krawczyk-Bärsch, U. Gerber, R. Steudtner

In EF-TEM/EELS studies it was shown that U(VI) is sorbed mainly on the outer membrane of *Acidovorax facilis*. The results are supported by TRLFS measurements, which were performed on the pellet of the cells. In comparison to reference spectra of some cell membrane components, the measured emission spectra of the *A. facilis* pellet show the best agreement with those of the Uranyl-lipopolysaccharide-complex. Hence, it can be concluded that phosphoryl groups may be the main binding sites for uranyl, located in the lipopolysaccharide unit in the outer membrane.

EXPERIMENTAL. For our studies we used *Acidovorax facilis* (formerly *Pseudomonas facilis*), an aerobic Gram-negative Betaproteobacteria, which is commonly found in soil. Experiments were performed in batch cultures under aerobic conditions at 25 °C using nutrient broth. The cells were grown to an optical density (OD600) of around 1.5. For U(VI) biosorption experiments the cultures were washed two times with tap water and then re-suspended in tap water. After that, $UO_2(NO_3)_2$ was added to the solution to achieve an initial uranium concentration of 0.05 and 0.1 mM at a neutral pH range. The duration of the sorption experiments were limited to 48 h. As a response to uranium stress, *A. facilis* was forming extracellular polymeric substances (EPS) resulting in the formation of cell agglomerates. For separating the EPS from the bacteria, the cell agglomerates were ultra-centrifuged ($40.000 \times g$) for 2 h at 10 °C. The cell pellet was used for time-resolved laser-induced fluorescence spectroscopy (TRLFS). The U(VI) luminescence at 274 K was measured after excitation with laser pulses at 266 nm and with an average pulse energy of 300 µJ. The emitted fluorescence light of the cell pellet was recorded using an iHR550 spectrograph and an ICCD camera in the 370–670 nm wavelength range by averaging 100 laser pulses and using a gate of 2000 µs. The data were analyzed using Origin software, version 8.6, including the Peak Fit module, version 4.0. After the U(VI) biosorption experiments, *A. facilis* cells were prepared for Energy-filtered transmission electron microscopy (EF-TEM) and electron energy-loss spectroscopy (EELS) by following the routine embedding protocol [1].

RESULTS. The measured emission spectrum of the pellet is characterized by five emission bands, as shown in the luminescence spectrum (Fig. 1). Their peak maxima were observed at 481.2, 497.8, 519.5, 544.1 and 569.3 nm ± 0.5 nm. In addition, the spectra of the Uranyl-complexes of lipopolysaccharide ($R-O-PO_3-UO_2$) and peptidoglycan ($R-COO-UO_2$) were used for comparison. The reference spectra display band positions at 481.5, 498.1, 519.6, 542.9 and 567.5 nm for pH 4 [2] as well as 481.6, 498.1, 518.0, 539.0 and 566.0 nm for pH 4 [3]. They show only a small deviation from those observed in our studies with the best agreement by those of the Uranyl-lipopolysaccharide-complex. Hence, it can be concluded that phosphoryl groups may represent the main binding sites for uranyl, located in the lipopolysaccharide unit in the outer membrane by Gram-negative *A. facilis* cells. But also complexation to on carboxylic groups can not completely ruled out.

The results provide microscopically and spectroscopically evidence of uranium sorbed at the outer membrane of
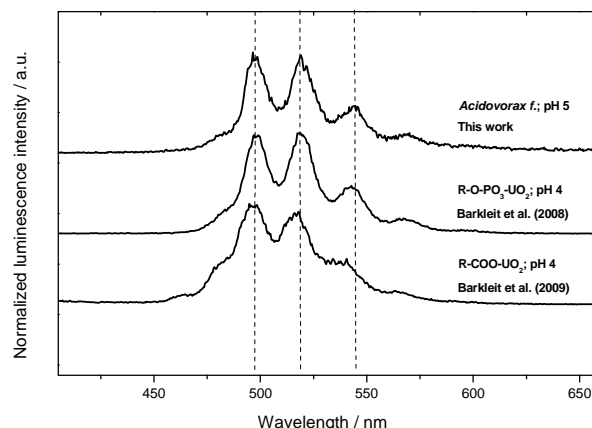
Fig. 1: Luminescence spectrum of *Acidovorax facilis* cells at 274 K exposed to U, in comparison with reference spectra of Uranyl-lipopolysaccharide- [2] and peptidoglycan-complexes [3].

A. facilis cells by showing high electron density. EELS analysis identified uranium as a constituent, based on ionization intensity peaks of O-edges (Fig. 2). The results support the TRLFS measurements and contribute to a better understanding of the binding mechanisms of U(VI) on *A. facilis* cells.
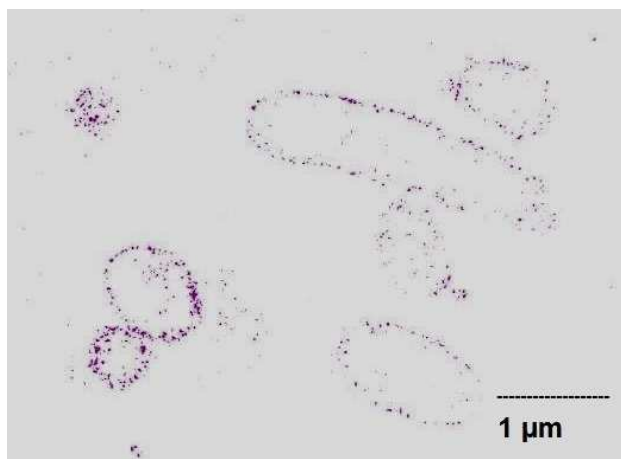
Fig. 2: EF-TEM element distribution mapping of uranium showing high electron density at the outer membrane of *A. facilis*

[1] Lünsdorf, H. et al. (2001) *Methods Enzymol.* **331**, 317–331.
[2] Barkleit, A. et al. (2008) *Dalton Trans.* 2879–2886.
[3] Barkleit, A. et al. (2009) *Dalton Trans.* 5379–5385.

Comparative studies on the interactions of the natural isolate KS5 and one reference strain (DSM 10134) with uranium(VI)

U. Gerber, E. Krawczyk-Bärsch, T. Arnold

The yeast KS5 (*Rhodosporidium toruloides*) was isolated by culure dependent method directly from the flooding water in Königstein (Germany). To compare the U tolerance and immobilization ability of the isolate a reference culture DSM 10134 (*R. toruloides*) was applied. Both cultures displayed the ability to tolerate high amounts of U, in contrast the reference KS5 showed a six-fold higher U tolerance in comparison to the reference strain. U immobilization studies displayed that both organisms are able to remove high amounts. The flooding water in Königstein has to be cleaned up for many years by an intensive waste water treatment plant. Possibly, with the help of natural occuring microorganisms the flooding water could be cleaned up using *in situ* bioremediation.

Fig. 1: Kinetic of U immobilization by KS5 and DSM 10134. Initial U concentration: 100 μM, background: tap water pH 5.0, incubation for 48 h at 30 °C and 180 rpm.

EXPERIMENTAL. The flooding water was collected at a pipeline of the waste water treatment plant into sterile bottles and was directly transported to the laboratory. Under sterile conditions several volumes (100–500 μL) were plated on solid agar plates containing SDA (Sabouraud dextrose agar) medium (5 g/L Peptone, 5 g/L Casein, 40 g/L Glucose and 15 g/L Agar). The agar plates were incubated at 28 °C for several days. After the appearance of single colonies they were transferred into liquid SD medium. The cultures were incubated at 28 °C, at 180 rpm for 48 h. Subsequently, the DNA was extracted using the alkaline lysis method for identification of the microorganism [1]. A part of the 18S rDNA gene was amplified using the primers EukA (5´-AACCTGGTTGATCCTGCCAGT-3´ [2]) and EukBr (5´-TGATCCTTCTGCAGGTTCACCTAC-3´ [3]). The resulting amplicons were analyzed by agarose gel electrophoresis, purified and sequenced by GATC (Germany). DSM 10134 (R. toruloides) was obtained from the Leibniz Institute DSMZ-German Collection of Microorganisms and Cell Cultures and cultivated in liquid SD medium at 28 °C. For U immobilization studies KS5 and DSM 10134 were grown in liquid SD medium and afterwards washed in background medium used for the immobilization experiment. Subsequently, the cells were harvested by centrifugation and U in the supernatant was determined by ICP-MS. For the determination of the MIC (Minimal inhibitory concentration) and MTC (Maximum tolerated concentration) five-fold diluted SDA medium was supplemented with several U concentrations (0.05–10.0 mM). The cells were grown for 48 h in liquid SD medium at 28 °C and 180 rpm. Afterwards the cells were harvested, washed and diluted to an OD_{600} of 0.5. An aliquot of 100 μL of the diluted cell suspensions were plated on the U containing plates.

Tab. 1: MIC and MTC of KS5 and DSM 10134 for U.

	MIC (mM)	MTC (mM)
Isolate KS5	6.0	5.0
DSM 10134	1.0	0.7

RESULTS. The results of the tolerance tests showed a six-fold higher U tolerance (Tab. 1) of the natural isolate KS5 (*R. toruloides*) compared to the reference strain DSM 10134. These findings suggest that natural occurring microorganisms within U contaminated waters developed adap-

tion mechanisms to survive. The immobilization experiments with an initial U concentration of 100 μM showed that the reference DSM 10134 is capable to immobilize higher amounts of U than the isolate KS5 (Fig. 1). The U immobilization within the first hours is faster and equilibrium is reached after 48 h with 150 mg U/1 g BDM (bio dry mass). Whereas the natural isolate KS5 immobilized around 120 mg U/1 g BDM. The immobilization of U by KS5 within the first hours was attributed to a slower process. The lower amount of immobilized U and also the slower process could also be explained by adaption mechanisms due to a response to U toxicity. Transmission Electron Microscopy analysis displayed that U is immobilized intracellularly by active bioaccumulation and in addition by passive biosorption on the cell membrane (data not shown) as already described [4, 5].
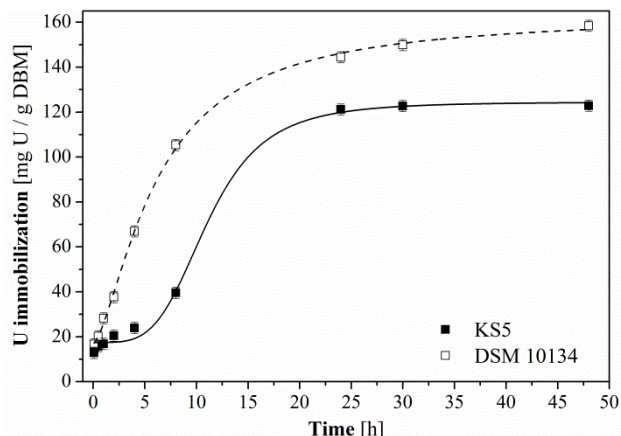
OUTLOOK. Further investigations on a molecular genetic level or on a protein level could explain the adaption mechanisms of the natural isolate and are needed to understand the interaction mechanisms of microorganisms with U in detail.

[1] Tsai, Y. et al. (1991) *Appl. Environ. Microbiol.* **57**, 1070–1074.
[2] Aguilera, A. et al. (2010) *International Microbiol.* **13**, 21–32.
[3] Aguilera, A. et al. (2006) *Syst. Appl. Microbiol.* **39**, 596–605.
[4] Markch, S. J. (2002) *Scientific World Journal* **2**, 707–729.
[5] Mullen, M. D. (1989) *Appl. Environ. Microbiol.* **55**, 3143–3149.

First insights in the Eu(III) speciation in *Halobacterium noricense* DSM-15987 suspensions

M. Bader, H. Moll, A. Cherkouk

The association of Eu(III) on the halophilic archaeon *Halobacterium* (*Hbt.*) *noricense* DSM-15987 was investigated between pC$_{H+}$ 4 to 8 in 3 M NaCl. In contrast to uranium [1], a lower affinity of Eu(III) towards *Hbt. noricense* was observed. Three different Eu(III)-species could be isolated in this system, whereas one is the Eu(III) aquo ion and one represents a *Hbt. noricense* associated species. The third species might belong to a dissolved species.

Currently, salt, clay and crystalline rocks are considered as potential host rocks for a nuclear waste disposal in Germany. In addition to bacteria and fungi, archaea are dominating the indigenous microbial community in salt rock as shown in the Waste Isolation Pilot Plant in Carlsbad, New Mexico, USA [2]. To date, only a few studies has evaluated the interactions of halophilic microorganisms with Eu(III) as inactive analogue for trivalent actinides [3]. Recently, an extremely halophilic archaeon namely *Hbt. sp.*, putatively *noricense* (WIPP strain) was isolated from the WIPP site [2]. Its closest phylogenetic relative *Hbt. noricense* DSM-15987, which we used for our investigations, was originally isolated from a salt mine in Austria [4].

EXPERIMENTAL. *Hbt. noricense* DSM-15987 was cultivated in DSM-Medium 372 at 30 °C. The cells were grown up to exponential growth phase (OD$_{600}$ of 0.5) for 4 days and harvested by centrifugation at 10,000 × g for 10 min. To study the interactions of *Hbt. noricense* with Eu(III), the cell pellet was washed three times and resuspended in 3 M NaCl solution containing 34 µM Eu(III). Due to the high ionic strength, the measured pH value was corrected by addition of the factor 0.49 to gain the hydrogen ion concentration pC$_{H+}$ according to literature [5]. TRLFS measurements were performed under N$_2$ atmosphere in 3 M NaCl at 25 °C. Changes in the Eu(III) speciation were investigated at a biomass concentration of 0.5 g/L as a function of pC$_{H+}$. Experimental details about the laser system can be found in [6].

RESULTS. The affinity of *Hbt. noricense* cells to accumulate Eu(III) is relatively low after an incubation time of 1 h (Fig. 1A). However, an increase of Eu(III) sorption was observed with increasing pC$_{H+}$ from 4.1 (10% sorbed) to 7.9 (40% sorbed).
In the *Hbt. noricense* system only weak changes are visible at pC$_{H+}$ ≤ 5.4 in the TRLFS spectra related to interactions between Eu(III) and *Hbt. noricense* (Fig. 1 B).
These spectral changes depending on pC$_{H+}$ are in agreement with the luminescence lifetime measurements. In the pC$_{H+}$
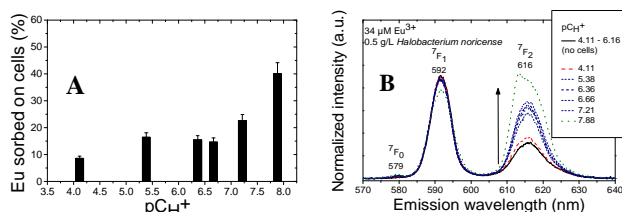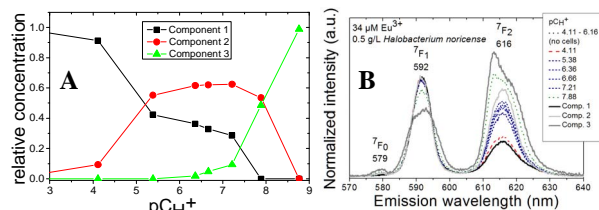
Fig. 2: ITFA results gained from the TRLFS spectra shown in Fig. 1B. Iterative target test (ITT) calculated species distribution of the components (A). ITFA extracted TRLFS component spectra (solid lines) and experimental data (dotted lines) (B).

range from 3.9 to 6.4, the short lifetime of ca. 108 µs can be assigned to the Eu(III) ion. Whereas the long lifetime of 430 µs measured at all pC$_{H+}$ values indicates a Eu(III) species either complexed with cell exudates or directly on functional groups of the cell envelope. From pC$_{H+}$ 6.7 to 8.1, the shorter lifetime increased to an average value of 190 µs. This indicates a third distinct chemical environment contributing to the speciation of Eu(III) in the cell suspensions. However, it is not possible to distinguish between cell bound and ligand bound Eu(III). For a comprehensive evaluation of the spectral data set recorded, iterative target transformation factor analysis (ITFA) was applied [7]. The calculations revealed three components (Fig. 2). Component 1 can be assigned with the Eu(III) aquo ion. Component 2 occurs over the neutral pC$_{H+}$ range 5 to 8 and is a stable innerspherical complex with 2 water molecules in its coordination sphere. A defined chemical assignment of the involved functional groups is not possible. Most likely it belongs to carboxylic groups but phosphoryl groups may also participate. Component 3 could be a dissolved species what is in accordance with the percentage sorption data. Such a detailed characterization of aqueous Eu(III)-*Hbt. noricense* species based on the changes of the intrinsic luminescence of Eu^{3+} has not been reported before.

[1] Bader, M., Cherkouk, A. (2015) *Report HZDR-059*, p. 10.
[2] Swanson, J. S. et al. (2012) *Status report Los Alamos National Laboratory LA-UR-12-22824*, p. 1.
[3] Ozaki, T. et al. (2004) *Radiochim. Acta* **92**, 741–748.
[4] Gruber, C. et al. (2004) *Extremophiles* **8**, 431–439.
[5] Borkowski, M. et al. (2009) *Report Los Alamos National Laboratory LA-14360*, p. 26.
[6] Moll, H. et al. (2008) *Biometals* **21**, 219–228.
[7] Rossberg, A. et al. (2003) *Anal. Bioanal. Chem.* **376**, 631–638.

Fig. 1: Eu(III) association on *Hbt. noricense* DSM-15987 after an incubation time of 1 h as a function of pC$_{H+}$ ([Eu] 34 µM, [dry biomass] 0.5 g/L, 3 M NaCl)(A). Corresponding TRLFS spectra (B).

Interactions of Eu(III) with biogenic CaCO₃ studied with TRLFS

E. V. Johnstone, A. Cherkouk, M. Schmidt

The interactions of Eu(III) with CaCO₃ arising from biogenic origin was investigated by Time-Resolved Laser-Induced Fluorescence Spectroscopy (TRLFS). Biologically-induced precipitation via ureolysis was studied with the bacteria *Sporosarcina pasteurii* in the presence of Eu(III). Biomineralization occurred forming mixed phases of vaterite and calcite after one day that transformed over two weeks to pure calcite. Eu(III) was quantitatively removed from solution during mineral formation. TRLFS results show that after one day the Eu^{3+} is located in the vaterite phase. After one week, the Eu^{3+} was found primarily in the vaterite, despite calcite now being the predominant mineral, and a transition species was also formed. In the calcite two incorporated Eu^{3+} species were present: one substitutes at the Ca^{2+} site in the crystal lattice and the other is speculated to be associated with the organic-mineral matrix.

EXPERIMENTAL. *Sporosarcina pasteurii* were grown and inoculated ($OD_{600} = 0.01$) into CaCO₃ mineralizing media [1] containing urea (333 mM) and Eu^{3+} (5×10^{-7} M). Mineralizing media without bacteria was used as a control. Mineralizing experiments were cultured at 30 °C under atmosphere for one day, one week, or two week durations. Changes in pH, [NH_4^+], and metal concentration in solution were tracked over time, and the resulting biomineral was collected and characterized by X-ray diffraction, thermal gravimetric analysis, microscopy, and TRLFS, as well as other physicochemical techniques. TRLFS was performed using a pulsed Nd:YAG laser pumped dye laser system at ~ 10 K.

RESULTS. Under the conditions studied, *S. pasteurii* were capable of ureolytically inducing CaCO₃ precipitation in the presence of Eu^{3+}. The decrease in concentrations of Eu^{3+} and Ca^{2+} was paralleled by the increase in pH and [NH_4^+] in solution where maximum values of 9.2 and 1 mol/L, respectively, were attained after 48 hours. Precipitation of CaCO₃ occurred between 3 and 4 hours, after which no detectable amount of leaching of Eu^{3+} was observed.

Samples taken after one day exhibited various morphologies, although framboidal agglomerations consistent with vaterite morphology were prevalent ranging from approximately 2 to 150 µm in size. The composition determined by XRD was a mixture of vaterite (91 wt%) and calcite (9 wt%). The content of organic material was ~ 6 wt% revealed by TGA. TRLFS analysis shows a single species centered at 579.1 nm (Fig. 1). The lifetime of this species was determined to be 4550 ± 580 µs consistent with no coordinated water and incorporation into the mineral. The emission spectra yielded a two-fold splitting of the $^5D_0 \rightarrow {}^7F_1$, and although the splitting of the $^7F_2$ band is unresolved the spectra is consistent with Eu^{3+} vaterite incorporation species.[2]

The sample after one week exhibited similar morphologies as the sample after one day, but particle surfaces contained rhombohedral growths as reported for calcite. This particle morphology transformation was consistent with phase composition that again yielded a mixed phase containing calcite (85 wt%) and vaterite (15 wt%). Again, the total amount of organic matter (2 wt%) was determined by TGA. The
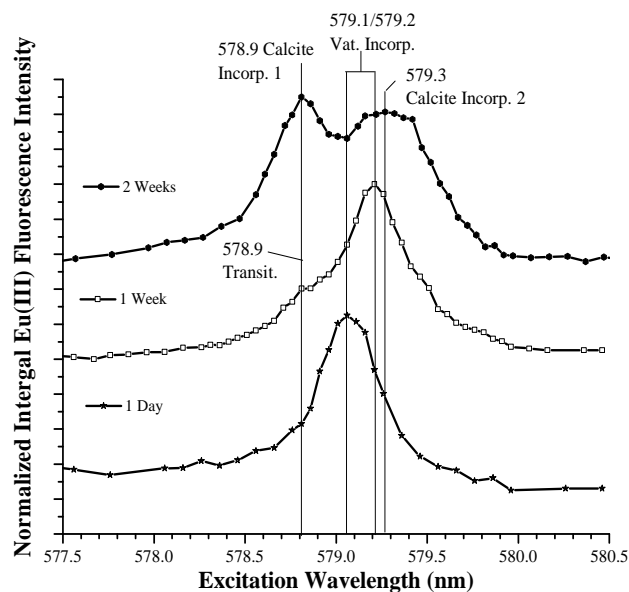
Fig. 1: Excitation spectrum of .Eu^{3+} species in biogenic CaCO₃ after one day, one week, and two weeks

TRLFS analysis yielded two species in the excitation spectrum at 578.9 nm and 579.2 nm. The lifetime measurement 4330 ± 560 µs and corresponding emission spectrum of the species at 579.2 nm were identical to the 579.1 nm species in the one day sample and consistent with Eu^{3+} incorporated into vaterite. The species at 578.9 nm yielded a lifetime of 1100 ± 140 µs associated with 0.5 coordinated water molecules, which is similar with the transition species reported previously during the transition of inorganic vaterite to calcite.[2]

The composition of the sample after two weeks was determined to be pure calcite with ~2 wt% organic material and particle morphologies consistent with biogenic calcite. TRLFS characterization of the sample yielded two distinct species in the excitation spectrum at 578.9 nm and 579.3 nm, respectively. The lifetime of the species at 578.9 nm was 2780 ± 360 µs indicative of complete loss of hydration and incorporation into the matrix. Similarly, the 579.3 nm species was also found to be incorporated in the mineral with a lifetime of 3380 ± 300 µs. The two-fold $^7F_1$ and three-fold $^7F_2$ bands in the emission spectrum of the 579.3 nm species are consistent with the Eu^{3+} substitution at the Ca^{2+} site in the calcite lattice.[3]

Compared to its inorganic counterpart, biomineralized CaCO₃ exhibits unique geochemical behavior arising from the incorporated biological signatures within the mineral, i.e., bacteria, organics. These results show that the origin of a mineral can affect how the mineral interacts with trivalent actinides and lanthanides.

[1] Stocks-Fischer, S. et al. (1999). *Soil Biol. Biochem.* **31**, 1563–1571.
[2] Schmidt, M. et al. (2010). *J. Colloid. Interf. Sci.* **351**, 50–56.
[3] Schmidt, M. et al. (2008). *Angew. Chem. Int. Ed.* **47**, 5846–5850.

Metal ion-specific thermal stability of bacterial S-Layers

B. Drobot, J. Raff, K. Fahmy

Many bacteria are covered by a surface layer (S-layer), i.e., a para-crystalline two-dimensional array of proteins which control cell shape, act as molecular sieves and have potential applications as radionuclide-binding material for bioremediation of polluted areas. Knowledge and control of the metal-dependent stability of the purified proteins is required for their technical application. Here, we have explored by differential scanning calorimetry the thermal stability of the S-layer protein slp-B53 from *Lysinibacillus sphaericus*, a Gram-positive bacterium isolated from a uranium mining waste pile [1].

EXPERIMENTAL. Differential scanning calorimetry (DSC) measurements were carried out on a nano-DSC (TA-instruments, Eschborn, Germany). A concentration of 7.5 mg/mL slp-B53 was used in all experiments, the heating rate was 0.5 Kmin^{-1}. Cation concentrations were 10 mM for runs with $CaCl_2$ and $MgCl_2$. Unfolding curves were fitted by Gaussian components and a sigmoidal curve in order to quantify contributions from different protein fractions and post-transition heat capacity changes, respectively.

RESULTS. Figure 1 shows the results of DSC experiments performed with slp-B53 under different ionic conditions. Four Gaussian curves could describe the heat capacity changes during thermal unfolding in all cases. The first un-

folding transition at about 45 °C amounted 13 to 20% of the integrated heat uptake. We assign it to a varying fraction of destabilized monomers in each sample because its DSC curve extended over a large temperature interval. The second and third components represent states with increasing stability which we assign to intact monomers (M) and dimers (D) in the desalted sample which unfold at 51 °C and 53 °C, respectively. Finally, the most stable protein fraction (L) unfolded at about 60 °C which was under all conditions accompanied by an increase of the post transition heat capacity Δc_p. Such an increase is typical of the exposure of hydrophobic protein surfaces during unfolding [2] and was accounted for by a sigmoidal function of variable position, steepness and amplitude.

The most stable fraction L exhibited the strongest modulation by ions. Its contribution to the DSC signal rose from 28% in the absence of salts to 37% in the presence of calcium. In agreement with the lattice-stabilizing function of calcium, we assign the high temperature transition to the disruption an S-layer-like lattice interactions between monomers. The concomitant decrease of the monomer contribution suggests that calcium recruits mainly monomers for the extension of S-layers, whereas the enthalpic contribution from dimers stayed almost constant. Magnesium was much less effective in evoking these changes (not shown). The assignment of the 60 °C transition to unfolding of proteins within a lattice is further supported by its width which decreased from 7 °K to 5 °K in the desalted and calcium-bound state, respectively. This indicates that the unfolding becomes more cooperative in the presence of calcium as expected for the formation of a para-crystalline lattice.

In summary, the neutralization of carboxylates on the protein surface by calcium is probably crucial for reducing protein solubility and increasing packing into the S-layer by abolishing electrostatic repulsion. The data support a model in which calcium but not magnesium promotes S-layer formation by assembling monomers into a lattice that is largely held together by ion coordination leading to the interfacial burial of hydrophobic protein surfaces. The increase of the solvent-exposed hydrophobic surface during unfolding is thus largest for Ca-bound S-layers, where the hydrophobic intermolecular contacts are initially buried in the protein interfaces of the lattice and become exposed only upon thermal denaturation. Correspondingly, the steepness and amplitude of the sigmoidal curves that account for changes in heat capacity before and after denaturation scale with the fraction S. In the absence of ions or with magnesium (not shown), M and D states dominate and their hydrophobic regions are solvent-exposed already in the folded state, such that unfolding cannot further increase the heat capacity to the extent seen with Ca^{2+}.

[1] Lederer, F. L. et al. (2013) *Microbiology* **159**, 1097–1108.
[2] Privalov, P. L. et al. (1988) *Adv. Protein Chem.* **39**, 191–234.
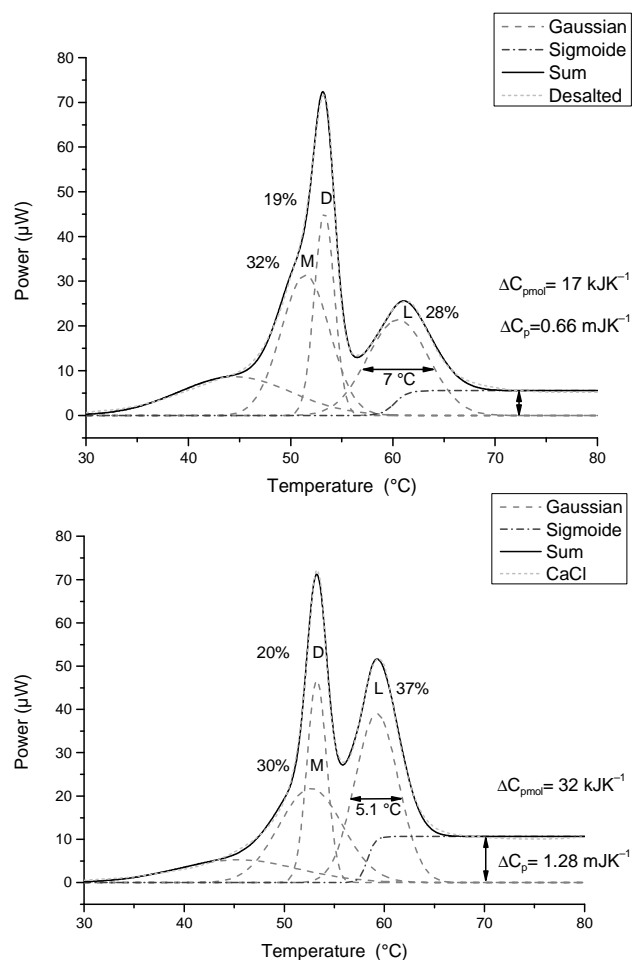
Fig 1: Differential scanning calorimetry (DSC) curves of slp-53 in the desalted state (A) and in the presence of 10 mM Ca^{2+} (B).

Interaction of actinides with plant cell metabolites: method development for the identification of plant cell metabolites

S. Sachs

A method for the separation of plant cell metabolites from nutrient media with subsequent HPLC analysis was developed.

Detailed knowledge of the radionuclide transfer in the environment including the food chain is the basis for the reliable assessment of the resulting risk potential for human and wildlife. In order to improve the knowledge of the underlying processes, interactions of plants with actinides are studied (e.g., [1–3]). Due to the interaction with heavy metal ions, plants segregate metal chelates into the rhizosphere, store metal chelates in vacuoles or synthesize protective metabolites that can bind metal ions and consequently reduce their availability in the cytoplasm [4]. We study the release of plant cell metabolites in consequence of the cell contact with actinide ions. Focusing on flavonoids, flavonoid glycosides, and phenolic acids, produced by plants as response to heavy metal stress (e.g., [5, 6]), a method is developed that allows the separation of these metabolites from nutrient media as basis for their further identification. This method involves the separation of metabolites from the medium by solid phase extraction (SPE), which is suitable for the separation of flavonoids and phenolic compounds from aqueous solutions (e.g., [7]), and their following analysis by high-performance liquid chromatography (HPLC).

EXPERIMENTAL. Methanolic solutions of quercetin, quercetin-3-β-d-glycoside and sinapinic acid were diluted with cell culture medium R [8] to a final concentration of 5×10^{-5} mol/L of each compound. CHROMABOND® HR-X columns (Macherey-Nagel) were used for SPE. The columns were activated with methanol, followed by acidified Milli-Q-water (pH 2, HCl). The pH value of the test solution was adjusted to pH 2 (HCl). 3 mL of this solution were given onto the SPE column. Subsequently, the column was washed with acidified Milli-Q-water (pH 2, HCl) in order to remove polar medium components, e.g., sucrose. The adsorbed substances were recovered by elution with 1 mL methanol. The initial test solution, its eluate after passing the column, the washing solution as well as the methanolic eluate were analyzed by HPLC using a method adapted from [9] (Agilent LC 1200; Zorbax Eclipse XDB-C_{18}, 4.6×150 mm, 5 µm; eluent A: H_2O-CH_3COOH (495 : 5), eluent B: CH_3OH, gradient elution, 1 mL/min; 23 °C; diode array detector (DAD): 254 nm; fluorescence detection (FLD): Ex: 380 nm, Em: 470 nm). In addition to the test solution, solutions of medium R before and after 24 h contact with *Brassica napus* cells [3] were subjected to SPE and subsequent HPLC.

RESULTS. Figure 1 shows the chromatograms of the initial test solution and its methanolic SPE eluate. Comparing the data it becomes obvious that all model substances are recovered in the eluate with slightly increased intensity. This points to a separation of the model compounds from the medium and their enrichment. The FLD data show also the occurrence of medium constituents in the eluate (marked with *). Nevertheless, a significant amount of the ingredients of medium R was removed by SPE. The chromatograms of the test solution after passing the SPE column and of the washing solution (data not shown) indicate that the
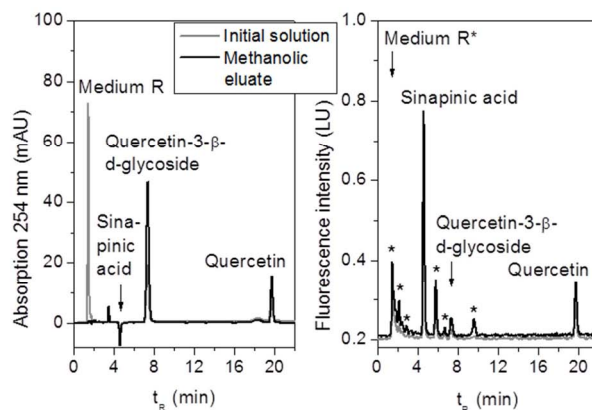
Fig. 1: Chromatograms of the initial test solution and the methanolic SPE eluate (DAD$_{254\,nm}$ (left), FLD$_{Ex:\,380\,nm,\,Em:\,470\,nm}$ (right)).

model compounds are completely bound onto the column and not washed out during the washing step. Thus, this method appears to be suitable to separate and enrich the studied type of compounds.

Figure 2 shows the chromatograms of medium R before and after cell contact and of the respective methanolic SPE eluates. The comparison of the data demonstrates the separation and enrichment of cell metabolites from the medium by SPE. Further studies will focus on the fractionation and spectroscopic identification of these metabolites.
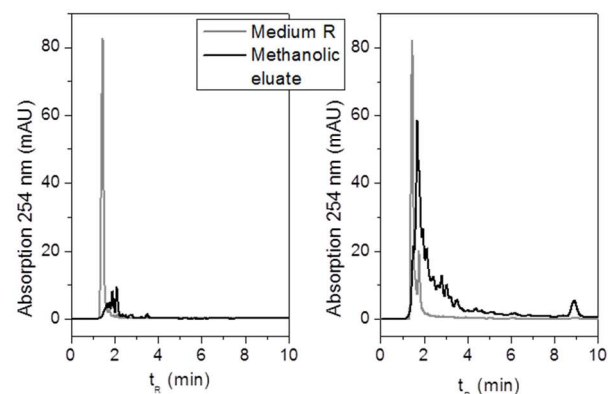
Fig. 2: Chromatograms of medium R before (left) and after contact with *Brassica napus* cells (right) and of their corresponding methanolic SPE eluates (DAD$_{254nm}$).

[1] Günther, A. et al. (2003) *Radiochim. Acta* **91**, 319–328.
[2] Laurette, J. et al. (2012) *Environ. Exp. Bot.* **77**, 96–107.
[3] Geipel, G. et al. (2015) *Biometals* **28**, 529–539.
[4] Weiler, E., Nover, L. (2008) *Allgemeine und molekulare Botanik*, Thieme, Stuttgart.
[5] Keilig, K. et al. (2009) *Bot. Stud.* **50**, 311–318.
[6] Janas, K. M. et al. (2009) *Acta Physiol. Plant* **31**, 587–595.
[7] Chen, H. et al. (2001) *J. Chromatogr. A* **913**, 387–395.
[8] www.dsmz.de/fileadmin/downloads/PC/medium/R.pdf.
[9] Daigle, D. J. et al. (1982) *J. Chromatogr.* **240**, 202–205.

Nuclear Reactor

SAFETY
RESEARCH

Sensitivity study of the reaction rate of a PWR Aeroball Measurement System (AMS)

J. Konheiser, S. Müller, M. Seidl[1]

[1]E.ON Kernkraft GmbH, Hannover, Germany

The Aeroball Measurement System (AMS) is an important in-core instrumentation in German pressurized water reactors. Therefore, it is essential to know the possible uncertainties of this system. One is the lack of knowledge of the correct positions of the balls in the guide tubes. The position changes can be up to 7 mm. Since the neutron flux distribution is not constant across the guide tubes, different reaction rates can result from the displacements. Both fuel assembly and full core calculations were carried out with the Monte Carlo code MCNP5. Differences in the reaction rates of up to 2% could be determined. In the most cases, differences are only up to 0.5%.

In Germany, KWU built pressurized water reactors (PWR), the so-called Aeroball Measuring System (AMS) is used for the high precision monitoring of the local core power. The measuring principle of the AMS is based on the activation of small moveable steel balls with 1.5 wt% vanadium. 28 fuel assembly positions are connected to the AMS. The AMS has been designed such that the balls can be pneumatically pushed back and forth from the reactor into a dedicated measuring system located inside in the reactor building during reactor operation. As a result of the rapid decay of ^{52}V, the AMS measurement can in principle be repeated every 15 minutes, practically without impact on the results of the next measurement. A detailed description of the AMS can be found in literature [1]. Since the three constituent tubes of the AMS have different diameters and no spacers in between, it is possible that during a cycle the balls are not always located in the center of the guide tubes. Displacements of up to 0.35 cm from the center are possible. In addition, it must be assumed that the power respectively neutron flux distribution within the guide tube has a certain gradient, so that the position of the AMS has an impact on the activation. To determine the impact of these uncertainties on the activation rate is the focus of this work.

MONTE-CARLO CALCULATION. The Monte Carlo method is ideally suited for such studies. The geometry can be precisely modeled and also be easily changed. On the other hand, since small effects are expected, good statistics is required. MCNP5 [2] was used for the calculations. All geometries have been reproduced in detail. At four quasi-independent positions in the fuel assemblies AMS were placed for the calculation. Figure 1 shows a horizontal cross section through the geometry model of the calculations. Periodic boundary conditions were assumed. The fuel assemblies consisted of a 16×16 square lattice. Each of the lattice cells contains either a fuel rod or a guide tube for an absorber rod. For the fuel assemblies with AMS lances these were precisely modeled in the corresponding guide tube positions.
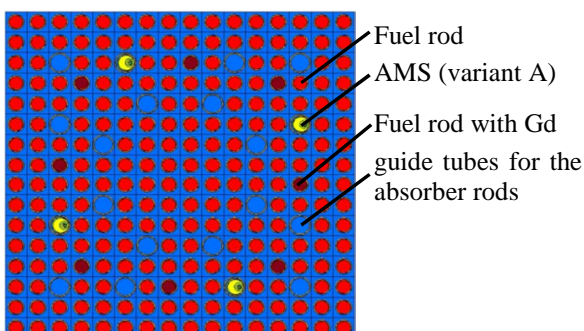
RESULTS. First, reference activation values were determined with the AMS lances in the middle position. The average reaction rate of the four positions were used as default values.

In order to study the displacement effect, the same fuel assembly conditions were assumed in each of the geometric variants. These were fresh assemblies without gadolinium and a boron concentration in the cooling water of 1000 ppm. Figure 2 shows the relative deviation of the reaction rates at eight positions different from the default position and for the three different geometric variants A, B and C.
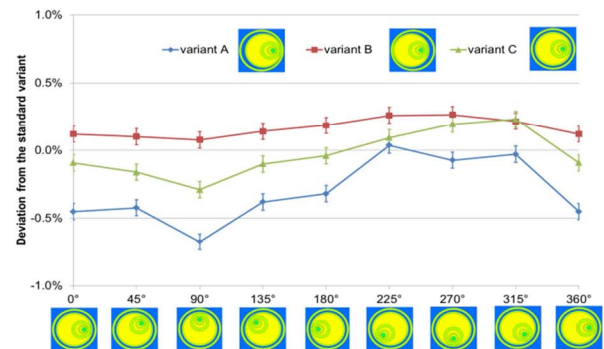
Fig. 2: Percentage deviation of three geometry variants from the reaction rates from the standard variant.

The small pictures below the diagram show the corresponding position of AMS lance components within the guide tube. It was found that the reaction rates for each variant only vary in a small corridor ranging from 0.2% to 0.7%. In the case of "A" the maximum deviations occur. It is remarkable that all of the values are virtually negative in this variant, i.e. reaction rates are always smaller than the reference.

CONCLUSIONS. The analysis has shown that the activation rates of the aeroball measurement system of KWU built PWRs are very robust with regard to possible variations of the AMS lance positions inside the fuel assembly guide tubes either in infinite-lattice configuration. The maximum deviation was found to be 0.7%.

[1] AREVA NP, U.S. EPR Nuclear Incore Instrumentation Systems, 2006, Report no. ANP-10271NP Revision 0.
[2] Kiedrowski, B. et al. (2010) *MCNP5-1.60 Feature Enhancements and Manual Clarifications*, LA-UR-10-06217.

Fuel rod

AMS (variant A)

Fuel rod with Gd

guide tubes for the absorber rods

Fig. 1: Calculation model of the fuel assembly with AMS.

Application of the severe accident code ATHLET-CD. Modelling and evaluation of accident management measures (Project WASA-BOSS)

P. Wilhelm, M. Jobst, S. Kliem, Y. Kozmenkov, F. Schäfer

The improvement of the safety of nuclear power plants is a continuously on-going process. The analysis of transients and accidents is an important research topic, which significantly contributes to safety enhancements of existing power plants. In case of an accident with multiple failures of safety systems core uncovery and heat-up can occur. In order to prevent the accident to turn into a severe one or to mitigate the consequences of severe accidents, different accident management measures can be applied. Numerical analyses are used to investigate the accident progression and the complex physical phenomena during the core degradation phase, as well as to evaluate the effectiveness of possible countermeasures in the preventive and mitigative domain [1, 2]. The presented analyses have been performed with the computer code ATHLET-CD developed by GRS [3, 4].

Within the framework of the joint research project „Weiterentwicklung und Anwendung von Severe Accident Codes – Bewertung und Optimierung von Störfallmaßnahmen" (WASA-BOSS) of the Federal Ministry of Education and Research, HZDR focuses on analyses of hypothetical severe accidents, assessment and optimization of accident management measures. Two basic accident scenarios are investigated: station blackout (SBO, total loss of AC power supply) and a loss of coolant accident (LOCA). To improve the confidence in the simulations, statistical methods were applied to evaluate the uncertainty in predicting the timings of main events as well as to estimate the time margins for operators to prepare countermeasures. During an SBO accident the observation of event occurrence significantly reduces timescale uncertainties for the subsequent events. This is a consequence of strong statistical correlations between the timings of events.

NUMERICAL ANALYSIS. An ATHLET-CD model for a generic German reactor of type KONVOI was developed. It includes all main components, systems and regulations, which are needed to simulate core degradation scenarios. The thermal hydraulic representation of the primary and secondary circuits is a two loops model; a triple loop and a single loop (Fig. 1). For the reactor core a six channel representation with typical KONVOI reactor geometry and data are applied.
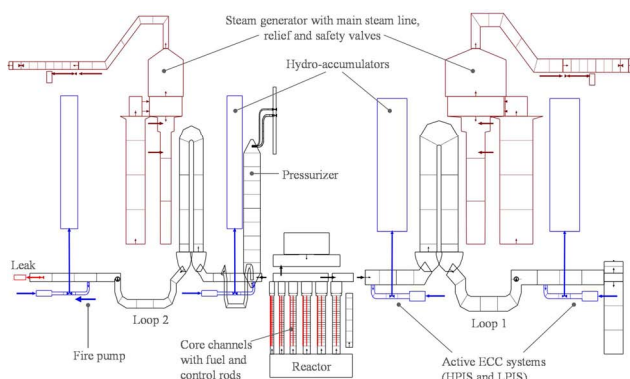
For the SBO event simulations for three basic scenarios were performed: case 1-SBO without accident management measures; case 2-SBO with primary side depressurization (PSD) at $T_{core\ exit} > 400$ °C; case 3-SBO with PSD and additional hypothetical injection from a mobile pump into the primary circuit. PSD is performed by full opening of the pressurizer relief and safety valves. The calculated problem time is 8 hours. Figure 2 depicts the main results of the simulations. Cladding temperature of 1200 °C is the criterion that the fuel cladding is cracked. Without any accident management measures (case 1) heating up of the core and reactor pressure vessel (RPV) failure under high pressure is expected. Reduction of the pressure on the primary side (case 2) allows water injection from the passive safety systems (hydro-accumulators). The core heat up is delayed with approximately 1.5 hours compared to the case without accident management. In case 3 the pump injection starts after PSD and as soon as the primary pressure drops below the nominal pump head. The results show that in this case the pump is able to compensate the mass loss through the pressurizer valves and heating up of the core can be stopped.
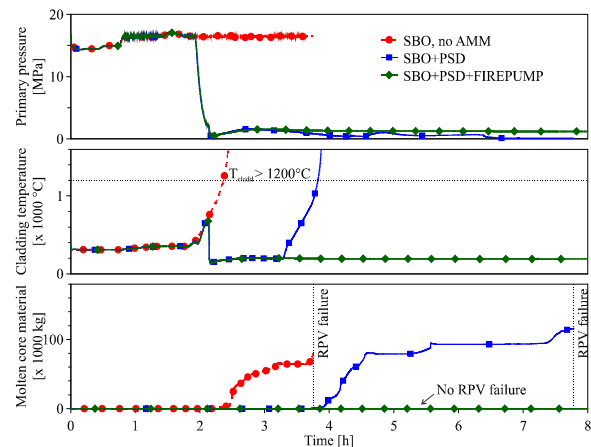
Fig. 2: SBO. Primary pressure, cladding temperature and mass of molten material evolution in time.

[1] Roth-Seefrid, H. et al. (1994) *Nucl. Eng. Des.* **148**, 133–150.
[2] Tusheva, P. et al. (2015) *atw.* **60**, 442–447.
[3] Lerchl, G. et al. (2012) *ATHLET Mod 3.0 Cycle A User's Manual,* Gesellschaft für Anlagen- und Reaktorsicherheit (GRS) mbH.
[4] Austregesilo, H. et al. (2014) *ATHLET-CD Mod 3.0 Cycle B User's Manual,* Gesellschaft für Anlagen- und Reaktorsicherheit (GRS) mbH.

Fig. 1: The model.

Hybrid Micro-Depletion method in the DYN3D code

Y. Bilodid

A new method for accounting spectral history effects was developed and implemented in the reactor dynamics code DYN3D. Detailed nuclide content is calculated for each region of the reactor core and used to correct fuel properties. The new method demonstrates excellent results in test cases.

Nuclear reactors' dynamics simulators such as DYN3D [1] are routinely used for nuclear reactor analyses. The neutronic properties of the nuclear fuel (XS) for reactor simulators are pre-generated using lattice neutron transport codes and stored in a form of XS-libraries. The following simplification is involved in the XS-libraries generation: fuel depletion is simulated in a lattice code in core-averaged operational conditions such as fuel and water temperatures. However, in a reactor core operational parameters are varying in space and time. The deviation of the local fuel depletion conditions from those used for XS-library generation leads to systematic errors in XS estimation, which are referred as spectral history effects.

A number of methods are utilized by reactor simulators to account for a spectral history. The local depletion history could be represented by some history indicator: a burnup-averaged value of operational parameters [2], a ratio of neutron fluxes in fast and thermal energy groups [3] or a local value of an indicator nuclide (e.g. Pu) [4]. The local value of such a history indicator is calculated by the reactor simulator code and used to correct the pre-generated XS from the XS-library. Another group of methods, so-called micro-depletion, propose to calculate the local concentrations of the most important nuclides and explicitly add their contributions to XS.

Each of the mentioned methods demonstrates acceptable accuracy in its range of applicability, but none is universal in terms of described systems and history effects.

THE NEW METHOD. This work proposes a generalized hybrid method capable of accurately accounting for various operational conditions and outage history effects, which combines extended micro-depletion with Pu-indicator method. Macroscopic absorption and fission XS are corrected using the micro-depletion correction, where the detailed nuclide content (one to two thousands of nuclides) is calculated for each node. Detailed nuclide content consideration allows obtaining concentrations of neutronically important nuclides without major approximations and simplifications in transmutation chains. Microscopic-XS, as well as the scattering matrix, diffusion coefficients and other fuel properties, are corrected proportionally to the sum of fissile nuclides ^{233}U, ^{235}U, ^{239}Pu, and ^{241}Pu absorption, which is chosen as the history indicator.

The hybrid method was implemented in the reactor dynamics code DYN3D. The depletion solver utilizes fast and accurate Chebyshev rational approximation (CRAM) method [5], which is particularly computationally efficient when applied to transmutation matrices.

The accuracy of the proposed hybrid micro-depletion method was verified against Serpent Monte-Carlo reference in 2D infinite lattice test cases with boiling water reactor (BWR) UOX and pressurized water reactor (PWR) MOX fuel unit cells. For each fuel type, a library of two-group macroscopic-XS, isotopic microscopic-XS and historical
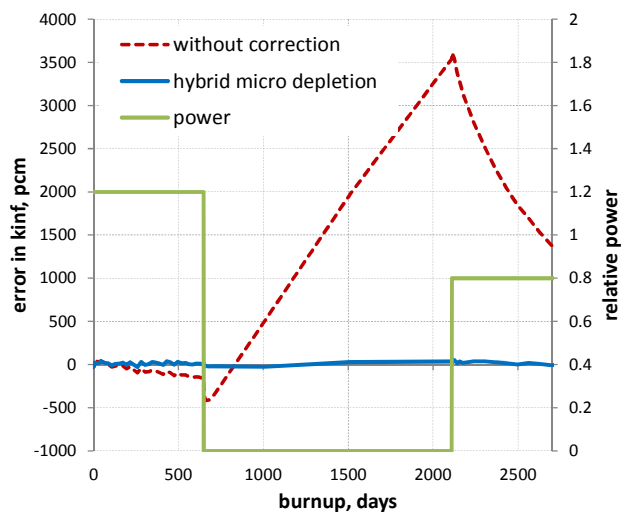
Fig. 1: Improvement of calculation results in a fuel outage test case.

coefficients was generated using two identical Serpent branching sets with different depletion histories. Each parameter in XS-library depends on burnup and instantaneous coolant density, fuel temperature and boron concentration for PWR cases. The obtained data sets were used by DYN3D to simulate fuel depletion in various spectral conditions.

VALIDATION. The proposed hybrid micro-depletion method was verified against Serpent Monte-Carlo reference in 2D infinite lattice test cases with BWR UOX and PWR MOX fuel unit cells. In all test cases, the deviation of the DYN3D results with hybrid micro-depletion from the reference was within the statistical uncertainty.

FUTURE WORK. Calculation of a detailed nuclide content (> 1000) nuclides is computationally costly. Depletion solver performance could be improved without loss of accuracy by optimizing transmutation matrix and keeping only neutronically important nuclides and their precursors (~300 nuclides).

On the other hand, tracking of detailed nuclide content would allow realistic modeling of decay heat and spent fuel activity without the need of any approximations.

The code user could choose between full and optimized transmutation matrix according to simulation purpose.

[1] Grundmann, U. et al. (2005) *Report FZR-434*.
[2] Bahadir, T. et al. (2005) *Proc. M&C 2005*.
[3] Baturin, D. M. et al. (2001) *Atomic Energy* **90**, 267–272.
[4] Bilodid, I. et al. (2010) *Ann. Nucl. Energy* **37**, 1208–1213.
[5] Pusa, M. et al. (2010). *Nucl. Sci. Eng.* **164**, 140–150.

DYN3D thermal expansion models for SFR applications

E. Nikitin, E. Fridman

The nodal diffusion code DYN3D is under extension for SFR applications. As a part of the extension a new model for axial thermal expansion of fuel rods was developed. The new model provides a flexible way of handling the axial fuel rod expansion, because each sub-assembly and node can be treated independently. The performance of the model was tested on a large oxide SFR core, and the results were compared to the reference full core Serpent solution. The test results indicated that the proposed model can accurately account for the axial expansion effects on full core level.

In this study a new model for the treatment of axial fuel rod expansions was developed for the nodal diffusion code DYN3D [1]. The idea of the model is to preserve the axial size of the nodes and to account for the axial expansion effects by manipulation of homogenized few-group cross sections (XS). The model was tested at full core level on a large Sodium fast reactor (SFR) core design adopted from the OECD/NEA SFR benchmark [2]. The XS were produced with Serpent Monte Carlo (MC) code [3], based on methodologies, which were recently established for 3D nodal diffusion analyses of SFR cores [4–6]. The XS are created for different degrees of the axial thermal expansion assuming the expansion is driven by the cladding temperature.

THE AXIAL FUEL ROD EXPANSION MODEL. The model recombines ("mixes") the XS for the affected nodes, depending on the contribution of the expanded materials inside of the node. It is done according to the following procedure:
- Initial axial discretization is specified to account for the material boundaries at some reference temperature (e.g. room temperature) as shown in Fig. 1 (left).
- The obtained axial nodes are further subdivided into a smaller node with a height of the anticipated maximal possible axial expansion of a lower node and into a bigger one as shown in Fig. 1 (right).
- For each sub-assembly, the local nodal temperatures are used for the estimation of the axial expansion and the new material interface levels. It should be noted that all new material levels are located within the "striped" regions as depicted in Fig. 1 (right).
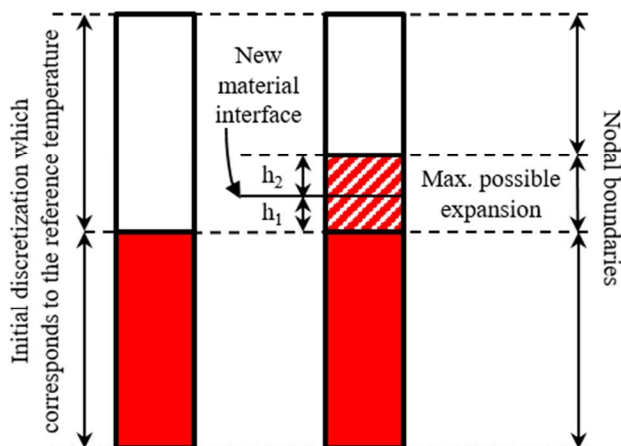
Tab. 1: Comparison of the axial fuel rod expansion coefficients.

dL/L	Axial expansion coefficient (pcm/K)		Relative difference
	Serpent	**DYN3D**	
0.5%	−0.122	−0.127	4.1%
1.0%	−0.147	−0.143	−2.7%
1.5%	−0.158	−0.160	1.3%
2.0%	−0.176	−0.178	1.1%

- When a new material interface within the "striped" regions is detected, the mixing of the XS is performed. For this purpose, volume weighted average of XS is used:

$$\Sigma = \frac{h_1\Sigma_1 + h_2\Sigma_2}{h_1 + h_2}, \qquad (1)$$

where h is the height of the material inside the node, Σ are the XS of the material, and the indices represent the lower and upper materials. The Σ includes all macroscopic reaction cross sections, group-to-group scattering matrices, and diffusion coefficients.

In principal, the XS mixing can be performed without specifying additional "mixing" nodes. However, the XS mixing over entire "initial" nodes can lead to a so-called cusping effect, which is especially problematic for the nodes with significantly different neutronic properties (e.g. adjacent fuel and sodium plenum nodes). The introduction of smaller "mixing" nodes helps to reduce this dilution and smearing effect.

RESULTS. The DYN3D calculations applying the mixing model were compared with the reference heterogeneous Serpent MC solution. The axial expansion coefficients are compared in Tab. 1. The DYN3D results are in very good agreement with the reference solution. The comparison of the axial power distributions show a good agreement with the Serpent solution. Even in the worst case – at 1.0% of expansion – the maximal relative difference for fuel nodes and the top node does not exceed 1.2% and 3.6%, respectively.

CONLCUSIONS. The results of the current test calculations indicate that the proposed model can accurately account for the axial expansion effects on full core level. Furthermore, the new model provides a flexible way of handling the axial fuel rod expansion, because each sub-assembly and node can be treated independently.

[1] Grundmann, U. et al. (2000) *Proc. PHYSOR 2000*, Pittsburgh, USA.
[2] Blanchet, D. et al. (2011) AEN – WPRS Sodium Fast Reactor Core Definitions (version 1.2), OECD/NEA.
[3] Leppänen, J. (2013) *Serpent – a Continuous-energy Monte Carlo Reactor Physics Burnup Calculation Code.* http://montecarlo.vtt.fi/.
[4] Fridman, E. et al. (2013) *Ann. Nucl. Energy* **53**, 354–363.
[5] Rachamin, R. et al. (2013) *Ann. Nucl. Energy* **55**, 194–204.
[6] Nikitin, E. et al. (2015) *Ann. Nucl. Energy* **75**, 492–497.

Fig. 1: Subdivion of nodes, and mixing of the XS according to the new material interface level.

Application of the SPH method in nodal diffusion analyses of SFR cores

E. Nikitin, E. Fridman, K. Mikityuk[1]

[1]Paul Scherrer Institut, Villigen, Switzerland

The current study investigated the potential of the SPH method, applied to correct the few-group XS produced by Serpent, to further improve the accuracy of the nodal diffusion solutions. The procedure for the generation of SPH-corrected few-group XS is presented in the paper. The performance of the SPH method was tested on a large oxide SFR core from the OECD/NEA SFR benchmark. The reference SFR core was modeled with the DYN3D and PARCS nodal diffusion codes using the SPH-corrected few-group XS generated by Serpent. The nodal diffusion results obtained with and without SPH correction were compared to the reference full-core Serpent MC solution. It was demonstrated that the application of the SPH method improves the accuracy of the nodal diffusion solutions, particularly for the rodded core state.

The goal of the current study is to assess the potential of Superhomogenization (SPH) method [1, 2], particularly applied to the control rod regions, to further improve the accuracy of the nodal diffusion solutions for Sodium cooled Fast Reactors (SFR). The approach to the generation of SPH-corrected homogenized few-group cross sections (XS) is briefly described and the performance of the SPH method is tested on a large SFR core design adopted from the OECD/NEA SFR benchmark [3]. The reference core is modeled with DYN3D [4] and PARCS [5] multi-group nodal diffusion codes using SPH-corrected few-group XS generated by Serpent Monte Carlo (MC) code [6]. The current results are compared with the previous Serpent-DYN3D and Serpent-PARCS solutions obtained without applying the SPH correction [7].

GENERATION OF SPH-CORRECTED XS. The SPH method was applied to correct the flux-volume weighted XS of the control rod (CR) channels. The SPH factors were calculated using the Serpent and DYN3D codes in the following manner.

a. The SPH factors μ for each region r and energy group g are calculated as:

$$\mu_{r,g} = \frac{\bar{\phi}_{r,g}^{Het}}{\phi_{r,g}^{Hom}} \cdot N_g,$$ (1)

where $\bar{\phi}_{r,g}^{Het}$ and $\phi_{r,g}^{Hom}$ are the average heterogeneous and homogeneous neutron fluxes in region r and group g obtained from heterogeneous Serpent transport solution and homogeneous DYN3D diffusion solution respectively. N_g is a normalization factor calculated as:

$$N_g = \frac{\sum_r V_r \cdot \phi_{r,g}^{Hom}}{\sum_r V_r \cdot \bar{\phi}_{r,g}^{Het}}.$$ (2)

b. Modified cross sections, $\Sigma_{r,g}^{Mod}$, are calculated for each region and energy group using the SPH factors generated according to Eq. 1:

$$\Sigma_{r,g}^{Mod} = \mu_{r,g} \cdot \Sigma_{r,g}.$$ (3)

c. The diffusion problem is solved again by the DYN3D code using the modified cross sections. The obtained homogeneous neutron fluxes are used for the calculation of a new set of the SPH factors. This iterative process is terminated after n iteration when the convergence criterion is satisfied for each r and g:

$$max\left\{\frac{|\mu_{r,g}^n - \mu_{r,g}^{n-1}|}{\mu_{r,g}^{n-1}}\right\} < 10^{-6}.$$ (4)

More details can be found in [8].

Tab. 1: Comparison of the multiplication factors and control rod worths.

	k-eff Serpent*	Difference vs. Serpent (pcm)			
		DYN3D	DYN3D + SPH	PARCS	PARCS + SPH
Unrodded	1.01070	−128	−64	−84	−21
Rodded	0.95249	−255	−107	−264	−121
$\Delta\rho_{CR}$, pcm	−6046	−127	−43	−180	−100

*: Standard deviation of k-eff = 2 pcm.

RESULTS. The DYN3D and PARCS calculations were compared with the reference heterogeneous Serpent MC solution for unrodded and rodded states. The integral core parameters are compared in Tab. 1. The k-eff is underestimated by DYN3D and PARCS, but the use of the SPH correction significantly reduces the discrepancy. Furthermore, the SPH correction noticeably improves the prediction of the total CR worth. The relative difference in radial power distribution between Serpent and nodal diffusion codes is shown in Tab. 2. As shown in Tab. 2, the use of the SPH correction reduces the deviation from the reference MC solution. The improvement in k-eff and radial power distribution is significantly more pronounced in the case of the rodded core modeling.

Tab. 2: Relative difference in radial power distribution.

	Ave. / Max. difference vs. Serpent (%)			
	DYN3D	DYN3D + SPH	PARCS	PARCS + SPH
Unrodded	0.25 / 0.66	0.21 / 0.59	0.35 / 1.07	0.23 / 0.67
Rodded	1.74 / 4.67	0.32 / 1.41	2.37 / 6.00	0.88 / 3.05

CONLCUSIONS. The presented results show that the application of the SPH correction leads to a better agreement in k-eff, radial power distribution, and total CR reactivity worth between the nodal diffusion and the reference MC solutions.

[1] Kavenoky, A. (1978). *The SPH Homogenization Method*, in Proc.: A Specialists' Meeting on Homogenization Methods in Reactor Physics, IAEA-TECDOC-231, Lugano, Switzerland.
[2] Hebert, A. (1993) *Nucl. Sci. Eng.* **113**, 227–238.
[3] Blanchet, D. et al. (2011) *AEN – WPRS Sodium Fast Reactor Core Definitions (version 1.2),* OECD/NEA.
[4] Grundmann, U. et al. (2000) *Proc. PHYSOR 2000*, Pittsburgh, USA.
[5] Downar, T. J. et al. (2010) *PARCS v3.0 – U.S. NRC Core Neutronics Simulator*, Theory Manual, Ann Arbor, MI.
[6] Leppänen, J. (2013) *Serpent – a Continuous-energy Monte Carlo Reactor Physics Burnup Calculation Code.* http://montecarlo.vtt.fi/.
[7] Nikitin, E. et al. (2015) *Ann. Nucl. Energy* **75**, 492–497.
[8] Nikitin, E. et al. (2015) *Ann. Nucl. Energy.* **85**, 544–551.

Simulation of a Pressurized Water Reactor Main Steamline Break benchmark case using the coupled codes DYN3D and Trio_U

A. Grahn, A. Gommlich, S. Kliem

In the framework of the European project NURESAFE, the reactor dynamics code DYN3D, developed at HZDR, was coupled with the Computational Fluid Dynamics (CFD) solver Trio_U, developed at CEA France, in order to replace DYN3D's one-dimensional hydraulic part with a full three-dimensional description of the coolant flow in the reactor core at higher spatial resolution. The present document gives a short introduction into the coupling method and shows results of its application to the simulation of a main steamline break (MSLB) accident.

COUPLING APPROACH. The method applied here is similar to that described in [1], in that the reactor core is represented by a porous domain and the physical interface between the core model of DYN3D and the CFD solver is the volumetric heat source provided by DYN3D. The feedback parameters sent back from Trio_U are coolant velocity, temperature and pressure, and boron concentration. Trio_U solves the internal energy transport equation

$$\frac{\partial T}{\partial t} + \mathbf{u} \cdot \nabla T = \frac{1}{\rho_0 c_{p0}} \left[\nabla \cdot (\lambda \nabla T) + S_{\text{th}} \right] \quad (1)$$

for the coolant. In this form, the equation assumes that a number of important material properties, in particular density ρ and specific heat capacity c_p, may not depend on temperature. This limitation of Trio_U may lead to an overprediction of the coolant temperature at the core outlet if coolant properties at core inlet temperature conditions are used in the simulation. In order to partly compensate the neglected temperature dependency, the modified heat source

$$S_{\text{th}}^* = \frac{\rho_0 c_{p0}}{(\rho c_p)_T} S_{\text{th}} \quad (2)$$

is introduced, which multiplies the heat source supplied by DYN3D with the correction factor $\rho_0 c_{p0}/(\rho c_p)_T$ where the denominator contains the actual coolant properties at the local temperature in the core. Since the coolant's heat capacity increases with increasing temperature in the relevant range of operational conditions, the heat source is downscaled appropriately. However, the constant density approximation of Trio_U, which gives rise to an imbalance of the mass conservation if the flow is non-isothermal, cannot be worked around. This may lead to discrepancies in the heat transfer coefficient and hence in the coolant temperature as compared to a standalone DYN3D calculation. At the code level, the coupling of DYN3D and Trio_U uses the Open-Source Salomé Platform (http://salome-platform.org) which provides objects and methods for computational mesh generation, field data storage and data interpolation between the low-resolution DYN3D nodal mesh and the refined mesh on which Trio_U solves the equations of momentum, boron and energy transport. Moreover, DYN3D and Trio_U implement the ICoCo specification [2] which defines the interface methods that allow a supervisor program to communicate with and to control the time advancing of the coupled codes.

APPLICATION TO MSLB. This simulation case considers a shut-down PWR whose secondary coolant loop suffers a break of the steamline connecting the steam generator with
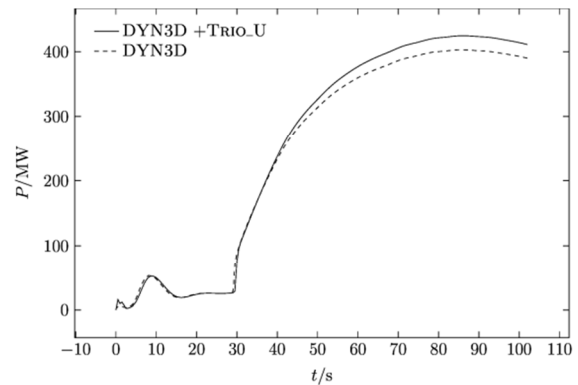
Fig. 1: Total power of the reactor core after main steamline break; comparison of coupled and DYN3D standalone solutions.

the turbine. The pressure loss leads to a sudden evaporation of the secondary coolant and a temperature drop which retroacts onto the primary coolant temperature. The colder primary coolant entering the reactor causes a power excursion of the latter due to the PWR feedback characteristics. Fig. 1 compares the core powers obtained by the coupled-code and by the DYN3D standalone simulations. During the power excursion, after approx. 40 s, both solutions begin to depart from each other and reach a maximum deviation of about 20 MW.

However, the coolant temperature profiles along the hottest fuel assembly at $t = 86$ s differ by less than 2 K, which is quite a good agreement, as can be seen in Fig. 2. The observed deviations are caused by the aforementioned approximations of the CFD code.
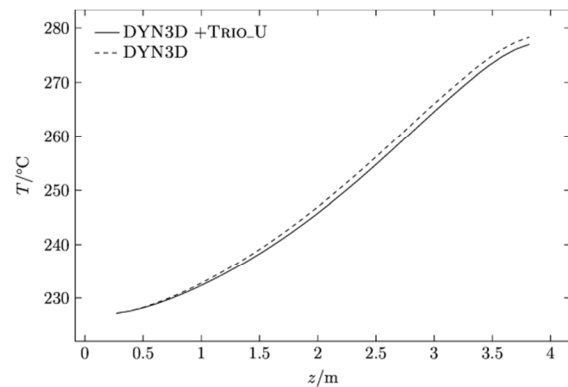
Fig. 2: Vertical coolant temperature profiles in hottest fuel assembly at $t = 86$ s.

Future applications of the code coupling encompass full reactor vessel simulations of overcooling and underboration transients to provide realistic reactor inlet boundary conditions due to coolant mixing in the upstream parts (downcomer, lower plenum) of the vessel.

[1] Grahn, A. et al. (2015) *Anucene* **8**, 197–203.
[2] Deville, E.; Perdu, F. (2012) *Documentation of the Interface for Code Coupling* : ICoCo, CEA, Paris.

HZDR contribution to the FP7-EURATOM project FREYA

E. Fridman

A short description of the European FP7-EURATOM project FREYA is presented. The HZDR contribution to FREYA is briefly summarized.

The Fast Reactor Experiments for hybrid Applications (FREYA)[1] is a European FP7 EURATOM project launched in 2011 and led by the Belgian Nuclear Research Centre (SCK•CEN). The main goal of FREYA is to support the design and licensing of sub-critical and critical fast spectrum systems which can be potentially used for transmutation of nuclear waste. The supported transmutation systems under consideration include Multi-purpose hYbrid Research Reactor for High-tech Applications (MYRRHA) [2] and Advanced Lead cooled Fast Reactor (LFR) European Demonstrator (ALFRED) [3]. While ALFRED is a "traditional" critical fast reactor, MYRRHA is being designed to operate in both critical and sub-critical (accelerator driven) modes. In the framework of the FREYA project, a number of sub-critical and critical experiments were conducted at the VENUS-F facility at SCK•CEN, Mol, Belgium. The major efforts were dedicated to the investigation of reactivity monitoring methods in sub-critical cores as well as to the validation of neutronic computational codes and nuclear cross section data of important actinides. The FREYA project consists of the following four technical working packages (WP):
– WP1: ADS on-line reactivity monitoring methodologies;
– WP2: Sub-critical configurations for design and licensing of MYRRHA;
– WP3: Critical configurations for design and licensing of MYRRHA;
– WP4: Critical configurations for LFR.
The Reactor Safety Division of Institute of Resource Ecology is involved in WP3 and WP4 of the FREYA project.

CRITICAL CORE CONFIGURATIONS. Within WP3 and WP4, several critical core configurations have been investigated in the VENUS-F reactor. Within the constraints of available fuel at the VENUS facility during the FREYA-project, these cores reflect basic features of the MYRRHA and ALFRED systems:
– CR0 – reference critical core (Fig. 1, left)
– CC5 – "clean" MYRRHA core mock-up (Fig. 1, right)
– CC7 – Modified CC5 core with additional graphite blocks simulating MYRRHA BeO reflector
– CC8 – Modified CC7 core with several MYRRHA In-Pile Sections (IPSs). "Full" MYRRHA core mock-up
– CC6 – Modified CC5 core with ALFRED island
The VENUS-F core contains a 12×12 square grid surrounded with a stainless steel casing and lead reflector. The core is loaded with 5×5 fuel assemblies (FA) of different design, reflector blocks, experimental assemblies, six safety and two control rods. The FA of the reference CR0 core consists of 30% enriched metal U rodlets and lead blocks. In the FA of the CC5-CC6 cores some of the lead blocks were replaced by Al_2O_3 rodlets. During the experimental campaign, several integral parameters were measured including: core multiplication factor (k-eff), effective delayed neutron fraction (β-eff), prompt neutron generation time, and control rod worth. The measured data also included:
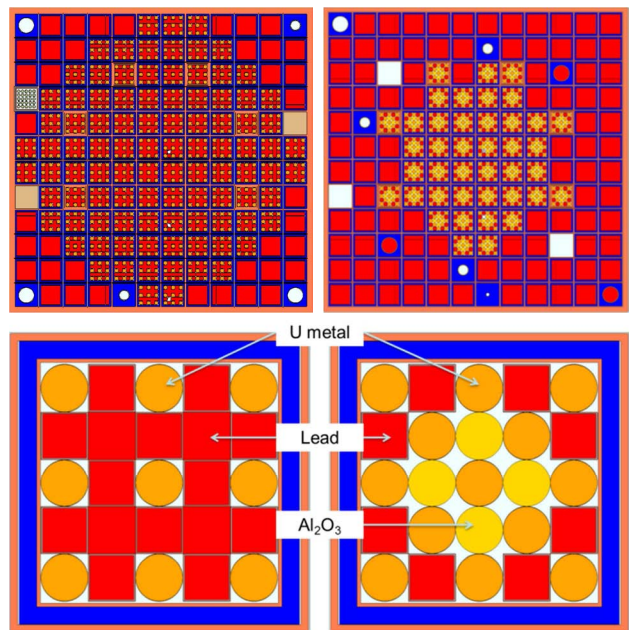
Fig. 1: VENUS-F core (up) and fuel assembly (down) configurations. Left: Reference critical configuration (CR0). Right: "Clean" MYRRHA mock-up (CC5).

– Axial traverses – axial fission rate distribution obtained with fission chambers containing different actinide deposits (U-234, U-235, U-238, Np-237, Pu-239)
– Spectral indexes – fission rate ratios of some important actinides such as U-234, U-238, Np-237, Pu-239, Pu-242, and Am-241 to that of U-235
– CC6 core – lead void reactivity effect

HZDR CONTRIBUTION. The aforementioned critical core configurations were modeled at HZDR using the continuous-energy Monte-Carlo (MC) reactor physics code Serpent [4]. The Serpent simulations were based on very detailed VENUS-F core models. The Serpent results were compared with the experimental data as well as with the computational results obtained by other project participants. The results are published [5, 6]. The analysis of the C/E discrepancies will help to improve the nuclear data in the energy region specific to fast reactors.

[1] http://freya.sckcen.be/en.
[2] Van den Eynde, G. et al. (2014). *An updated core design for the multi-purpose irradiation facility MYRRHA*, in proc.: PHYSOR 2014, Kyoto, Japan.
[3] Grasso, G. et al. (2014). *Nucl. Eng. Des.* **278**, 287–301.
[4] Leppänen, J. (2013). *Serpent – a Continuous-energy Monte Carlo Reactor Physics Burnup Calculation Code.* http://montecarlo.vtt.fi/
[5] Kochetkov, A. et al. (2015). *Control Rod Worth Measurements in a Fast Neutron VENUS-F critical core,* in proc.: ICAPP 2015, Nice, France.
[6] Kochetkov, A. et al. (2016). *Spectrum Indexes and Minor Actinides measurements in several fast lead cooled VENUS-F zero power critical cores,* in proc.: PHYSOR 2016, Sun Valley, USA.

Investigation of severe slugging under flow conditions of a parabolic trough power plant with direct steam generation

A. Hoffmann

The DISS test facility at the Plataforma Solar de Almería, Spain, produces high pressure steam directly within the parabolic trough collectors. Two collectors are connected with a U-shaped connection pipe which can suffer under the flow phenomenon of severe slugging at low mass flow operation. The objective is to investigate numerically the flow situations with ATHLET and state the relevance of severe slugging in the installed U-shaped pipes. The simulation results reveal that normal operation conditions are uncritical and no severe slugging can be expected.

Severe slugging can occur in a pipeline-riser system that consists of a horizontal or downwards inclined pipe and a following upwards inclined pipe, cf. Fig. 1. If a low gas and liquid mass flow is fed at the inlet an irregular and periodic two-phase flow at the outlet can occur, namely severe slugging [1, 2]. In the course of this the outlet pressure is kept constant. One severe slugging cycle contains four steps (Fig. 1): slug formation, slug production, blowout and blowdown [3]. The main driving forces are the gravitational force in the vertical pipe and the compressibility of the gas phase in the downwards inclined pipe [4].
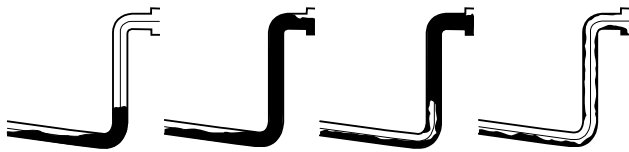
Fig. 2: Schematic of the four steps of one severe slugging cycle from left to right.

METHOD. The one-dimensional two-fluid model of ATHLET [5] is used for the numerical investigation. The separated transient momentum equations for gas and liquid phase enable reliable simulations. A successful validation of ATHLET for severe slugging is shown in [6]. The present contribution studies different flow conditions (inlet mass flows, outlet pressures). The given flow conditions are mass flows from $\dot{m} = 0.4$–1.6 kg/s, $\dot{x} = 0.02$–0.06 and pressures from $p = 5$–60 bar. The tested pipe geometry consists of a horizontal, downwards inclined and vertical pipe. More details are reported in [6].

RESULTS. A simulation case is evaluated as severe slugging case if the height of the accumulated water in the vertical pipe reaches an averaged hydrostatic pressure of over 0.2 bar, cf. first drawing in Fig. 1. Figure 2 and 3 depict the calculated cases and cases with severe slugging are assigned with a fulfilled marker. The cases at 5 bar show severe slugging in a relatively large related region. The lowest line of markers represents the smallest mass flow of 0.4 kgs^{-1} and the top one the highest mass flow of 1.6 kgs^{-1}. At a system pressure of 30 bar the region of severe slugging is considerably reduced. This behavior can be explained with the decreasing density ratio of the liquid and gas phase at higher pressures. The compression of the gas phase is aggravated and, consequently, an important mechanism in the formation of severe slugging is attenuated. Interestingly there are no cases with severe slugging at the lowest mass flow which actually is the most critical situation. At an operating pressure of 60 bar no severe slugging is calculated.
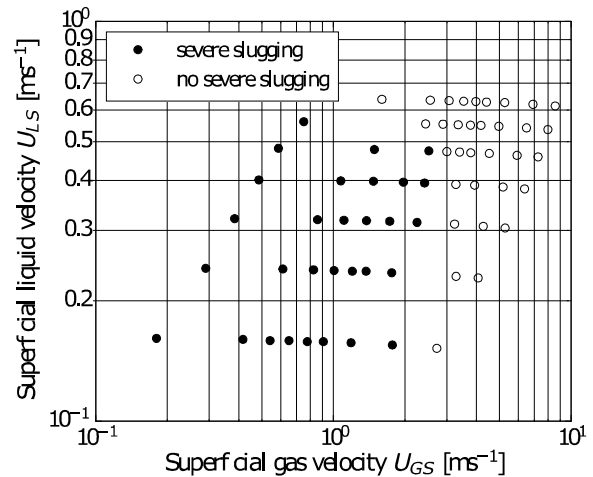
Fig. 1: Results for different inlet conditions at 5 bar [6].
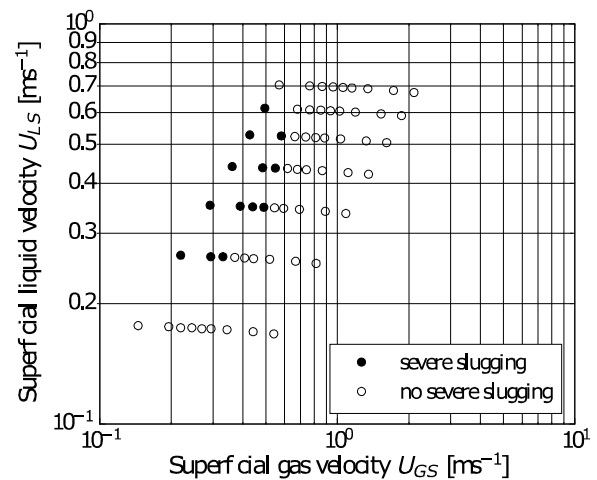
Fig. 2: Results for different inlet conditions at 30 bar [6].

CONCLUSIONS. Severe slugging in fixed pipe geometry is numerically investigated at different flow conditions. At low pressures severe slugging is more often computed especially at low mass flow rates. Furthermore, the results reveal that a high pressure operation basically prevents the occurrence of severe slugging. Due to the high pressure direct steam generation in parabolic trough power plants undesired implications of severe slugging are not expected during the operation.

[1] Schmidt, Z. et al. (1985) *Soc. Petroleum Eng. J.* **25**, 27–38.
[2] Schmidt, Z. et al. (1980) *Soc. Petroleum Eng. J.* **20**, 407–414.
[3] Taitel, Y. (1986) *Int. J. Multiphase Flow* **12**, 203–217.
[4] Balino, J. et al. (2010) *Int. J. Multiphase Flow* **36**, 643–660.
[5] Austregesilo, H. et al. (2012) ATHLET Mod 3.0 Cycle A, GRS.
[6] Hoffmann, A. et al. (2016) *Solar Energy*, submitted.

⭕ ARTICLES (PEER-REVIEWED)

⭕ ORAL PRESENTATIONS

⭕ THESES

◯ Articles (peer-reviewed)

Ander, M.; Subramaniam, S.; Fahmy, K.;
Stewart, F.; Schäffer, E.
**A single-strand annealing protein clamps
DNA to detect and secure homology**
PLOS Biology 13, A018 (2015).

Aoyagi, N.; Shinha, Y.; Ikeda-Ohno, A.; Haga, Y.;
Shimojo, K.; Brooks, N. R.; Izuoka, A.;
Naganawa, H.; Kimura, T.; Binnemans, K.
**Photophysical Property of Catena-
Bis(thiocyanato)aurate(I) Complexes in Ionic
Liquids**
*Crystal Growth & Design 15, 1422–1429
(2015).*

Bauer, K.; Kulenkampff, J.; Henninges, J.;
Spangenberg, E.
**Lithological control on gas hydrate saturation
as revealed by signal classification of NMR
logging data**
*Journal of Geophysical Research B – Solid
Earth 120, 6001–6017 (2015).*

Bilodid, Y.; Kotlyar, D.; Margulis, M.; Fridman, E.;
Shwageraus, E.
**Spectral history model in DYN3D:
Verification against coupled Monte-Carlo
thermal-hydraulic code BGCore**
Annals of Nuclear Energy 81, 34–40 (2015).

Chanaron, B.; Ahnert, C.; Crouzet, N.; Sanchez, V.;
Kolev, N.; Marchand, O.; Kliem, S.;
Papukchiev, A.
**Advanced multi-physics simulation for
reactor safety in the framework of the
NURESAFE project**
Annals of Nuclear Energy 84, 166–177 (2015).

Drobot, B.; Steudtner, R.; Raff, J.; Geipel, G.;
Brendler, V.; Tsushima, S.
**Combining Luminescence Spectroscopy,
Parallel Factor Analysis and Quantum
Chemistry to Reveal Metal Speciation –
A Case Study of Uranyl (VI) Hydrolysis**
Chemical Science 6, 964–972 (2015).

Dulnee, S.; Scheinost, A. C.
**Interfacial Reaction of SnII on Mackinawite
(FeS)**
*Journal of Contaminant Hydrology 177–178,
183–193 (2015).*

Falaise, C.; Volkringer, C.; Hennig, C.; Loiseau, T.
**Ex-Situ Kinetic Investigations of the
Formation of the Poly-Oxo Cluster U_{38}**
*Chemistry – A European Journal 21, 16664–
16654 (2015).*

Foroutan-Nejad, C.; Vícha, J.; Marek, R.;
Patzschke, M.; Straka, M.
**Unwilling U–U bonding in $U_2@C_{80}$: cage-
driven metal–metal bonds in di-uranium
fullerenes**
*Physical Chemistry, Chemical Physics 17,
24182–24192 (2015).*

Franzen, Ch.; Kretzschmar, J.; Franzen, C.;
Weiss, S.
**Staining on heritage building stone identified
by NMR spectroscopy**
*Environmental Earth Sciences 74, 5275–5282
(2015).*

Fröhlich, D. R.; Skerencak-Frech, A.; Bauer, N.;
Rossberg, A.; Panak, P. J.
**The pH dependence of Am(III) complexation
with acetate: an EXAFS study**
*Journal of Synchrotron Radiation 22, 1–6
(2015).*

Fröhlich, D. R.; Skerencak-Frech, A.; Kaplan, U.;
Koke, C.; Rossberg, A.; Panak, P. J.
**An EXAFS spectroscopic study of Am(III)
complexation with lactate**
*Journal of Synchrotron Radiation 22, 1469–
1474 (2015).*

Gaillard, C.; Boltoeva, M.; Billard, I.; Georg, S.;
Mazan, V.; Ouadi, A.; Ternova, D.; Hennig, C.
**Insights into the Mechanism of Extraction of
Uranium (VI) from Nitric Acid Solution into
an Ionic Liquid by using Trin-butyl
phosphate**
ChemPhysChem 16, 2653–2662 (2015).

Geipel, G.; Viehweger, K.
**Speciation of uranium in compartments of
living cells**
BioMetals 28, 529–539 (2015).

Grahn, A.; Kliem, S.; Rohde, U.
**Coupling of the 3D neutron kinetic core
model DYN3D with the CFD software
ANSYS CFX**
Annals of Nuclear Energy 84, 197–203 (2015).

Hildebrand, H.; Schymura, S.; Holzwarth, U.;
Gibson, N.; Dalmiglio, M.; Franke, K.
**Strategies for radiolabeling of commercial
TiO_2 nanopowder as a tool for sensitive
nanoparticle detection in complex matrices**
*Journal of Nanoparticle Research 17, 278
(2015).*

Holt, L.; Rohde, U.; Seidl, M.; Schubert, A.; van Uffelen, P.
Development of a general coupling interface for the fuel performance code TRANSURANUS tested with the reactor dynamics code DYN3D
Annals of Nuclear Energy 84, 73–85 (2015).

Husar, R.; Hübner, R.; Hennig, C.; Martin, P. M.; Chollet, M.; Weiss, S.; Zänker, H.; Stumpf, T.; Ikeda-Ohno, A.
Intrinsic formation of nanocrystalline neptunium dioxide under neutral aqueous conditions relevant to deep geological repositories
Chemical Communications 51, 1301–1304 (2015).

Husar, R.; Weiss, S.; Hennig, C.; Hübner, R.; Ikeda-Ohno, A.; Zänker, H.
Formation of neptunium(IV)-silica colloids at near-neutral and slightly alkaline pH
Environmental Science & Technology 49, 665–671 (2015).

Iglesias, L.; Walther, C.; Medina, F.; Holzer, A.; Neumann, A.; Lozano-Rodriguez, M. J.; Alvarez, M. G.; Torapava, N.
A comprehensive study on iodine uptake by selected LDH phases via coprecipitation, anionic exchange and reconstruction
Journal of Radioanalytical and Nuclear Chemistry (2015).

Jain, R.; Jordan, N.; Schild, D.; van Hullebusch, E. D.; Weiss, S.; Franzen, C.; Farges, F.; Hübner, R.; Lens, P. N. L.
Adsorption of zinc by biogenic elemental selenium nanoparticles
Chemical Engineering Journal 260, 855–863 (2015).

Jain, R.; Jordan, N.; Weiss, S.; Foerstendorf, H.; Heim, K.; Kacker, R.; Hübner, R.; Kramer, H.; van Hullebusch, E. D.; Farges, F.; Lens, P. N. L.
Extracellular polymeric substances govern the surface charge of biogenic elemental selenium nanoparticles
Environmental Science & Technology 49, 1713–1720 (2015).

Jain, R.; Seder-Colomina, M.; Jordan, N.; Dessi, P.; Cosmidis, J.; van Hullebusch, E. D.; Weiss, S.; Farges, F.; Lens, P. N. L.
Entrapped elemental selenium nanoparticles affect physicochemical properties of selenium fed activated sludge
Journal of Hazardous Materials 295, 193–200 (2015).

Jimenez, G.; Herrero, J.; Gommlich, A.; Kliem, S.; Cuervo, D.; Jimenez, J.
Boron dilution transient simulation analyses in a PWR with neutronics/thermal-hydraulics coupled codes in the NURISP project
Annals of Nuclear Energy 84, 86–97 (2015).

Kotlyar, D.; Fridman, E.; Shwageraus, E.
One-Group Cross-Section Generation for Monte Carlo Burnup Codes: Multigroup Method Extension and Verification
Nuclear Science and Engineering 179 (2015).

Kozmenkov, Y.; Kliem, S.; Rohde, U.
Validation and verification of the coupled neutron kinetic/thermalhydraulic system code DYN3D/ATHLET
Annals of Nuclear Energy 84, 153–165 (2015).

Krawczyk-Bärsch, E.; Lütke, L.; Moll, H.; Bok, F.; Steudtner, R.; Rossberg, A.
A spectroscopic study on U(VI) biomineralization in cultivated *Pseudomonas fluorescens* biofilms isolated from granitic aquifers
Environmental Science and Pollution Research 22, 4555–4565 (2015).

Kretzschmar, J.; Jordan, N.; Brendler, E.; Tsushima, S.; Franzen, C.; Foerstendorf, H.; Stockmann, M.; Heim, K.; Brendler, V.
Spectroscopic evidence for selenium(IV) dimerization in aqueous solution
Dalton Transactions 44, 10508 (2015).

Kutschke, S.; Guézennec, A. G.; Hedrich, S.; Schippers, A.; Borg, G.; Kamradt, A.; Gouin, J.; Giebner, F.; Schopf, S.; Schlömann, M.; Rahfeld, A.; Gutzmer, J.; D'Hugues, P.; Pollmann, K.; Dirlich, S.; Bodénan, F.
Bioleaching of Kupferschiefer blackshale – A review including perspectives of the Ecometals project
Minerals Engineering 75, 116–125 (2015).

Lakatos, M.; Matys, S.; Raff, J.; Pompe, W.
Colorimetric As (V) Detection Based on S-Layer Functionalized Gold Nanoparticles
Talanta 144, 241–246 (2015).

Lebreton, F.; Horlait, D.; Caraballo, R.; Martin, P.; Scheinost, A. C.; Rossberg, A.; Jégou, C.; Delahaye, T.
Peculiar behavior of (U,Am)O$_2$−δ compounds for high americium contents evidenced by XRD, XAS, and Raman spectroscopy
Inorganic Chemistry 54, 9749–9760 (2015).

Lopez-Fernandez, M.; Cherkouk, A.; Vílchez-Vargas, R.; Sandoval, R.; Pieper, D.; Boon, N.; Sánchez-Castro, I.; Merroun, M.
Bacterial diversity in bentonites, engineered barrier for deep geological disposal of radioactive wastes
Microbial Ecology 70, 922–935 (2015).

Mansel, A.; Franke, K.
Production of no-carrier-added ^{135}La at an 18 MeV cyclotron and its purification for investigations at a concentration range down to 10–15 mol/L
Radiochimica Acta 103, 759–763 (2015).

Merk, B.; Litskevich, D.
Is transmutation of all German transuranium in the frame of the nuclear phase out feasible?
PlosOne 10, e0145652 (2015).

Merk, B.; Litskevich, D.
On the burning of Plutonium originating from Light Water Reactor use in a fast molten salt reactor – A neutron physical study
Energies 8, 12557–12572 (2015).

Merk, B.; Stanculescu, A.; Chellapandi, P.; Hill, R.
Progress in fast reactor operation and new trends to increased inherent safety
Applied Energy 147, 104–116 (2015).

Mesbah, A.; Szenknect, S.; Clavier, N.; Lozano-Rodriguez, J.; Poinssot, C.; Den Auwer, C.; Ewing, R. C.; Dacheux, N.
Coffinite, USiO$_4$, Is Abundant in Nature: So Why Is It So Difficult To Synthesize?
Inorganic Chemistry 54, 6687–6696 (2015).

Moog, H. C.; Bok, F.; Marquardt, C. M.; Brendler, V.
Disposal of nuclear waste in host rock formations featuring high-saline solutions – Implementation of a thermodynamic reference database (THEREDA)
Applied Geochemistry 55, 72–84 (2015).

Müller, K.; Gröschel, A.; Rossberg, A.; Bok, F.; Franzen, C.; Brendler, V.; Foerstendorf, H.
In situ spectroscopic identification of neptunium(V) inner-sphere complexes on the hematite-water interface
Environmental Science & Technology 49, 2560–2567 (2015).

Nikitin, E.; Fridman, E.; Mikityuk, K.
On the use of the SPH method in nodal diffusion analyses of SFR cores
Annals of Nuclear Energy 85, 544–551 (2015).

Nikitin, E.; Fridman, E.; Mikityuk, K.
Solution of the OECD/NEA neutronic SFR benchmark with Serpent-DYN3D and Serpent-PARCS code systems
Annals of Nuclear Energy 75, 492–497 (2015).

Oberta, P.; Kittler, M.; Áč, V.; Hrdý, J.; Iragashi, N.; Scheinost, A. C.; Uchida, Y.
The influence of metallic brazing materials on the strain formation of internally water-cooled X-ray optics
Journal of Synchrotron Radiation 22, 342–347 (2015).

Osman, A. A. A.; Geipel, G.; Barkleit, A.; Bernhard, G.
Uranium(VI) Binding Forms in Selected Human Body Fluids: Thermodynamic Calculations versus Spectroscopic Measurements
Chemical Research in Toxicology 28, 238–247 (2015).

Prieur, D.; Belin, R. C.; Manara, D.; Staicu, D.; Richaud, J. C.; Vigier, J. F.; Scheinost, A. C.; Somers, J.; Martin, P.
Linear thermal expansion, thermal diffusivity and melting temperature of Am-MOX and Np-MOX
Journal of Alloys and Compounds 637, 326–331 (2015).

Prieur, D.; Lebreton, F.; Martin, P. M.; Caisso, M.; Butzbach, R.; Somers, J.; Delahaye, T.
Comparative XRPD and XAS study of the impact of the synthesis process on the electronic and structural environments of uranium-americium mixed oxides
Journal of Solid State Chemistry 230, 8–13 (2015).

Rachamin, R.; Fridman, E.; Galperin, A.
Feasibility assessment of the once-through Thorium fuel cycle for the PTVM LWR concept
Annals of Nuclear Energy 85, 1119–1130 (2015).

Reitz, T.; Rossberg, A.; Barkleit, A.; Steudtner, R.; Selenska-Pobell, S.; Merroun, M. L.
Spectroscopic study on uranyl carboxylate complexes formed at the surface layer of *Sulfolobus acidocaldarius*
Dalton Transactions 44, 2684–2692 (2015).

Sachs, S.; Heller, A.; Weiss, S.; Bok, F.;
Bernhard, G.
**Interaction of Eu(III) with mammalian cells:
Cytotoxicity, uptake and speciation as a
function of Eu(III) concentration and
nutrient composition**
Toxicology In Vitro 29, 1555–1568 (2015).

Satchanska, G.; Topalova, Y.; Dimkov, R.;
Groudeva, V.; Petrov, P.; Tsvetanov, C.;
Selenska-Pobell, S.; Golovinsky, E.
**Phenol degradation by environmental
bacteria entrapped in cryogels**
*Biotechnology & Biotechnological Equipment
29, 514–521 (2015).*

Schmid, M.; Ona-Burgos, P.; Guillaume, S. M.;
Roesky, P. W.
**(Iminophosphoranyl)(thiophosphoranyl)
methane Rare-Earth Borohydride
Complexes: Synthesis, Structures and
Polymerization Catalysis**
Dalton Transactions 44, 12338–12348 (2015).

Schmidt, M.; Hellebrandt, S.; Knope, K. E.;
Lee, S. S.; Stubbs, J. E.; Eng, P. J.;
Soderholm, L.; Fenter, P.
**Effects of the Background Electrolyte on
Th(IV) Sorption to Muscovite Mica**
*Geochimica et Cosmochimica Acta 165, 280–
293 (2015).*

Schott, J.; Kretzschmar, J.; Tsushima, S.; Drobot, B.;
Acker, M.; Barkleit, A.; Taut, S.; Brendler, V.;
Stumpf, T.
**The interaction of Eu(III) with organoborates
– a further approach to understand the
complexation in the An/Ln(III)–borate
system**
Dalton Transactions 44, 11095–11108 (2015).

Smith, A. L.; Raison, P. E.; Martel, L.; Prieur, D.;
Charpentier, T.; Wallez, G.; Suard, E.;
Scheinost, A. C.; Hennig, C.; Martin, P.;
Kvashnina, K. O.; Cheetham, A. K.;
Konings, R. J. M.
**A new look at the structural properties of
trisodium uranate Na_3UO_4**
Inorganic Chemistry 54, 3552–3562 (2015).

Tits, J.; Walther, C.; Stumpf, T.; Mace, N.;
Wieland, E.
**A luminescence line-narrowing spectroscopic
study of the uranium(VI) interaction with
cementitious materials and titanium dioxide**
Dalton Trans. 44, 966–976 (2015).

Tusheva, P.; Altstadt, E.; Willschütz, H. G.;
Fridman, E.; Weiß, F. P.
**Investigations on in-vessel melt retention by
external cooling for a generic VVER-1000
reactor**
Annals of Nuclear Energy 75, 249–260 (2015).

Tusheva, P.; Schäfer, F.; Kozmenkov, Y.; Kliem, S.;
Hollands, T.; Trometer, A.; Buck, M.
**WASA-BOSS: ATHLET-CD model for
severe accident analysis for a generic
KONVOI reactor**
atw 60, 442–447 (2015).

Valero, E.; Martín, M.; Gálvez, N.; Sánchez, P.;
Raff, J.; Merroun, M. L.; Dominguez-
Vera, J. M.
**Nanopatterning of Magnetic CrNi Prussian
Blue Nanoparticles Using a Bacterial S-layer
as Biotemplate**
Inorganic Chemistry 54, 6758–6762 (2015).

Vauchy, R.; Robisson, A. C.; Belin, R.; Martin, P.;
Scheinost, A.; Hodaj, F.
**Room-temperature oxidation of
hypostoichiometric uranium-plutonium
mixed oxides $U_{1-y}Pu_yO_{2-x}$ – a depth-selective
approach**
*Journal of Nuclear Materials 465, 349–357
(2015).*

Vauchy, R.; Robisson, A. C.; Martin, P. M.;
Belin, R. C.; Aufore, L.; Scheinost, A. C.;
Hodaj, F.
**Impact of the cation distribution homogeneity
on the americium oxidation state in the
$(U_{0.54}Pu_{0.45}Am_{0.01})O_{2-x}$ mixed oxide**
*Journal of Nuclear Materials 456, 115–119
(2015).*

Vigier, J. F.; Martin, P. M.; Martel, L.; Prieur, D.;
Scheinost, A. C.; Somers, J.
**Structural investigation of $(U_{0.7}Pu_{0.3})O_{2-x}$
mixed oxides**
Inorganic Chemistry 54, 5358–5365 (2015).

Weinert, U.; Pollmann, K.; Barkleit, A.; Vogel, M.;
Günther, T.; Raff, J.
**Synthesis of S-Layer Conjugates and
Evaluation of Their Modifiability as a Tool
for the Functionalization and Patterning of
Technical Surfaces**
Molecules 20, 9847–9861 (2015).

Weinert, U.; Vogel, M.; Reinemann, C.;
Strehlitz, B.; Pollmann, K.; Raff, J.
**S-layer proteins as an immobilization matrix
for aptamers on different sensor surfaces**
*Engineering in Life Sciences 15, 710–720
(2015).*

Wu, H.; Ikeda-Ohno, A.; Wang, Y.; Waite, T. D.
Iron and phosphorus speciation in Fe-conditioned membrane bioreactor activated sludge
Water Research 76, 213–226 (2015).

Xiong, Q.; Joseph, C.; Schmeide, K.; Jivkov, A. P.
Measurement and modelling of reactive transport in geological barriers for nuclear waste containment
Physical Chemistry, Chemical Physics 17, 30577–30589 (2015).

Yalcintas, E.; Gaona, X.; Scheinost, A. C.; Kobayashi, T.; Altmaier, M.; Geckeis, H.
Redox chemistry of Tc(VII)/Tc(IV) in dilute to concentrated NaCl and MgCl$_2$ solutions
Radiochimica Acta 103, 57–72 (2015).

◯ ORAL PRESENTATIONS

Bader, M.; Drobot, B.; Müller, K.; Stumpf, T.; Cherkouk, A.
Biosorption of uranium on the cells of the halophilic archaea *Halobacterium noricense* DSM-15987 under highly saline conditions
Workshop on Actinide-Brine-Chemistry (ABC-Salt 4), April 14–15, 2015, Heidelberg, Germany (2015).

Bader, M.; Drobot, B.; Müller, K.; Stumpf, T.; Cherkouk, A.
Interactions between a halophilic archaeon and uranium regarding the final disposal of radioactive waste in salt rock
Petrus PhD Conference 2015, Radioactive waste management and disposal, June 22–26, 2015, Nancy, France (2015).

Bilodid, Y.; Kotlyar, D.; Shwageraus, E.; Fridman, E.; Kliem, S.
Accounting for spectral history effects with improved microscopic depletion in DYN3D code
25th Symposium of AER on VVER Reactor Physics and Reactor Safety, October 13–16, 2015, Balatongyörök, Hungary (2015).

Bok, F.; Richter, A.; Brendler, V.; Altmaier, M.
A new set of Pitzer parameters for dissolved oxygen and its implication on the U(IV)/U(VI) system
Workshop on Actinide-Brine-Chemistry (ABC-Salt 4), April 14–15, 2015, Heidelberg, Germany (2015).

Brachem, C.; Konheiser, J.; Hampel, U.
On the Feasibility of using Ex-core Neutron Instrumentation for Reactor State Diagnosis during Accidents
23rd International Conference on Nuclear Engineering (ICONE), May 17–21, 2015, Chiba, Japan (2015).

Brachem, C.; Schmidt, S.; Konheiser, J.; Hampel, U.
Simulation of the Gamma Radiation Distribution Emitted from a PWR Core under Severe Accident-Like Conditions
46th Annual Meeting on Nuclear Technology, May 05–07, 2015, Berlin, Germany (2015).

Cherkouk, A.; Bader, M.; Drobot, B.; Müller, K.; Stumpf, T.
Biosorption of U(VI) at highly saline conditions
Goldschmidt 2015, August 16–21, 2015, Prague, Czech Republic (2015).

Chotkowski, M.; Weiss, S.; Scheinost, A. C.
Interaction of technetium with neptunium in acidic media
3rd Academic Symposium on Nuclear Fuel Cycle, December 02–05, 2015, Tokyo, Japan (2015).

Drobot, B.; Raff, J.
Interaction of trivalent lanthanides and actinides with calcium binding proteins
Meeting with the Natrajan Group (The University of Manchester), October 26, 2015, Manchester, U.K. (2015).

Drobot, B.; Tsushima, S.; Steudtner, R.; Raff, J.;
Geipel, G.; Brendler, V.
**Speciation studies of uranyl(VI) using an
advanced combination of theoretical and
luminescence spectroscopic methods**
*Anakon 2015, March 23–26, 2015, Graz,
Austria (2015).*

Eichelbaum, S.; Lippmann-Pipke, J.; Korn, N.;
Kulenkampff, J.
**Quantifying 3D tracer velocity and porosity
on core scale from 3D GeoPET image
sequences**
*IAMG 2015, The 17th Annual Conference of the
International Association for Mathematical
Geosciences, September 05–13, 2015, Freiberg,
Germany (2015).*

Ferrari, A.; Konheiser, J.; Müller, S. E.
**Shielding and activation analysis status for
the MYRRHA research reactor**
*MAXSIMA Work Package 2 – Technical
Meeting, April 20, 2015, Mol, Belgium (2015).*

Ferrari, A.; Konheiser, J.; Müller, S. E.
Status of the Task 11.1 from HZDR: Part 1
*CHANDA Work Package 11 Meeting, February
20, 2015, Dresden, Germany (2015).*

Foerstendorf, H.
**Identifizierung der Oberflächenkomplexe von
Radionukliden an Mineralphasen –
Schwingungsspektroskopische
Echtzeitexperimente**
*Institutsseminar des Instituts für Kernchemie,
Universität Mainz, February 02, 2015, Mainz,
Germany (2015).*

Foerstendorf, H.; Heim, K.; Franzen, C.; Jordan, N.
**The surface complexes of the oxoanions of
Se(VI) and Tc(VII) at mineral-water
interfaces**
*Goldschmidt 2015, August 16–21, 2015, Prague,
Czech Republic (2015).*

Franke, K.; Hildebrand, H.; Schymura, S.
**Use of a Cyclone 18/9 for Radiolabelling of
Nanoparticles**
*International Conference on Nuclear Analytical
Methods in the Life Science (NAMLS11), August
23–28, 2015, Delft, The Netherlands (2015).*

Fritsch, K.; Schmeide, K.
**U(VI) retention by montmorillonite at high
salinities: surface complexation modeling**
*Workshop on Actinide-Brine-Chemistry (ABC-
Salt 4), April 14–15, 2015, Heidelberg,
Germany (2015).*

Geipel, G.; Viehweger, K.
**Laser-Induced Spectroscopy of Actinides –
From simple metal systems to species in living
cells**
*ACS Annual Spring Meeting, March 22–26,
2015, Denver, U.S.A. (2015).*

Gerber, U.; Krawczyk-Bärsch, E.; Arnold, T.
**Investigations of the interactions of
subsurface living microorganisms with
uranium**
*3. Workshop – TransAqua, April 20–21, 2015,
Bremen, Germany (2015).*

Gerber, U.; Krawczyk-Bärsch, E.; Arnold, T.;
Kothe, E.
**Investigations of the interactions of
subsurface living microorganisms with
uranium**
*2. Projektstatusgespräch zu BMBF-geförderten
Forschungs- und Entwicklungsvorhaben auf
dem Gebiet der "Nuklearen Sicherheits- und
Entsorgungsforschung sowie
Strahlenforschung", March 25–26, 2015,
Dresden, Germany (2015).*

Gerber, U.; Krawczyk-Bärsch, E.; Arnold, T.;
Merroun, M. L.
**Interactions of natural occurring eukaryotic
microorganisms isolated from the uranium
mine Königstein (Saxony, Germany) with
U(VI)**
*Remediation Symposium 2015, September 30–
October 01, 2015, Jena, Germany (2015).*

Gerber, U.; Röder, G.; Krawczyk-Bärsch, E.;
Arnold, T.
**Reduction of U(VI) by anaerobic
microorganisms within the flooding water of
Königstein**
*2. Workshop TP5 TransAqua, November 16–17,
2015, Jena, Germany (2015).*

Hampel, U.; Brachem, C.; Lange, C.; Kratzsch, A.;
Schmidt, S.; Fiß, D.; Härtel, S.; Konheiser, J.
**Nichtinvasive Zustandsüberwachung von
Kernreaktoren zur Detektion von
Füllstandsänderungen und Deformationen
des Kerns**
*Projektstatusgespräch zu BMBF-geförderten
FuE-Arbeiten auf dem Gebiet der Nuklearen
Sicherheits- und Entsorgungsforschung sowie
Strahlenforschung, March 25, 2015, Dresden,
Germany (2015).*

Hellebrandt, S.; Schmidt, M.; Knope, K. E.;
Lee, S. S.; Stubbs, J. E.; Eng, P. J.;
Soderholm, L.; Fenter, P.
**Influence of background electrolyte on
Th(IV) sorption behavior**
*GDCh-Wissenschaftsforum Chemie 2015 –
Chemie verbindet, August 30–September 02,
2015, Dresden, Germany (2015).*

Hellebrandt, S. E.; Hofman, S.; Stubbs, J. E.;
Eng, P. J.; Stumpf, T.; Schmidt, M.
**Sorption of trivalent rare earth elements on
calcite**
*Goldschmidt 2015, August 16–21, 2015, Prague,
Czech Republic (2015).
GDCh-Wissenschaftsforum Chemie 2015 –
Chemie verbindet, August 30–September 02,
2015, Dresden, Germany (2015).
Migration 2015 – 15th International Conference
on the Chemistry and Migration Behaviour of
Actinides and Fission Products in the
Geosphere, September 13–18, 2015, Santa Fe,
U.S.A. (2015).*

Hennig, C.
**Formation of solution species and
nanoparticles of tetravalent metal ions in
aqueous solution**
*Vortrag im Rahmen des Schwerpunktprogramms
„Understanding of Metal Oxide/Water Systems
at the Molecular Scale: Structural Evolution,
Interfaces, and Dissolution", October 15, 2015,
Berlin, Germany (2015).*

Hennig, C.
**The Rossendorf Beamline at ESRF –
dedicated to investigate radionuclides with
X-ray absorption spectroscopy**
*Laboratoire d'Electrochimie et de
Physicochimie des Matériaux et des Interfaces,
CNRS, Grenoble, February 13, 2015, Grenoble,
France (2015).*

Hennig, C.; Ikeda-Ohno, A.; Takao, S.; Takao, K.;
Kraus, W.; Scheinost, A. C.
**Complex formation of tetravalent actindies
with small carboxylate ligands**
*Migration 2015 – 15th International Conference
on the Chemistry and Migration Behaviour of
Actinides and Fission Products in the
Geosphere, September 13–18, 2015, Santa Fe,
U.S.A. (2015).*

Hildebrand, H.; Schymura, S.; Holzwarth, U.;
Bellido, E.; Ojea-Jimènez, I.; Dalmiglio, M.;
Cotogno, G.; Gibson, N.; Franke, K.
**Measuring at relevant concentrations –
Radiolabelling as a versatile tool for sensitive
nanoparticle detection in complex systems**
*ICCE 2015, 15th EuCheMS International
Conference on Chemistry and the Environment,
September 20–24, 2015, Leipzig, Germany
(2015).*

Huittinen, N.; Arinicheva, Y.; Holthausen, J.;
Neumeier, S.; Stumpf, T.
**Incorporation of Cm^{3+} and Eu^{3+} in LnPO$_4$
ceramics – a site-selective TRLFS study**
*Scientific Basis for Nuclear Waste Management
XXXIX, November 02–06, 2015, Montpellier,
France (2015).*

Huittinen, N.; Arinicheva, Y.; Holthausen, J.;
Schmidt, M.; Neumeier, S.; Stumpf, T.
**Curium(III) and europium(III) incorporation
in lanthanide phosphate ceramics for
conditioning of radioactive wastes**
*Migration 2015 – 15th International Conference
on the Chemistry and Migration Behaviour of
Actinides and Fission Products in the
Geosphere, September 13–18, 2015, Santa Fe,
U.S.A. (2015).*

Ikeda-Ohno, A.
**Coordination chemistry for separation of
nuclear-related metals**
*LEPMI-CNRS internal seminar, February 13,
2015, Grenoble, France (2015).*

Ikeda-Ohno, A.
**Development of selective ligands for
f-elements separation**
*Microsymposium on Coordination Chemistry,
March 26, 2015, TU Dresden, Dresden,
Germany (2015).*

Ikeda-Ohno, A.
**Polymer and cluster chemistry of f-elements
in aqueous solutions**
*Internal seminar, Institut für Radioökologie und
Strahlenschutz, Leibnitz Universität Hannover,
April 30, 2015, Hannover, Germany (2015).*

Ikeda-Ohno, A.
**X-ray Absorption Spectroscopy for Actinide
Chemistry – Basics, Experiments and
Applications**
*The ThUL School in Actinide Chemistry,
September 28–October 02, 2015, Karlsruhe,
Germany (2015).*

Ikeda-Ohno, A.; Weiss, S.; Hennig, C.
Polymer and cluster chemistry of tetravalent cerium in aqueous solutions – Comparison with tetravalent actinides
The 9th International Conference on f-Elements (ICfE 9), September 08, 2015, Oxford, U.K. (2015).

Karimzadeh, L.; Lippmann-Pipke, J.
Porosity, particle velocity, and diffusion coefficient evolution due to kinetic mineral dissolution – application of iCP (interface COMSOL PHREEQC) for reactive transport modelling
6th Workshop of the PhD Network on Reactive Transport - Modeling and Experiments, November 30–December 01, 2015, Jülich, Germany (2015).

Kliem, S.
AER Working Group D on VVER Safety Analysis – Report of the 2015 Meeting
25th Symposium of AER on VVER Reactor Physics and Reactor Safety, October 13–16, 2015, Balatongyörök, Hungary (2015).

Kliem, S.
The HZDR reactor dynamics code DYN3D
1st Sino-German Symposium on Fundamentals of Advanced Nuclear Safety Technology, March 09–12, 2015, Shanghai, China (2015).

Kostudis, S.
Biologie meets Bergbau: Biotechnologie für die Gewinnung von Kupfer
Nacht der Wissenschaft und Wirtschaft zum Jubiläum, June 20, 2015, Freiberg, Germany (2015).

Kotlyar, D.; Shwageraus, E.; Fridman, E.
Multi Group Geometrical Correction for Coupled Monte Carlo Codes: Multi-Regional Thermal System
Joint International Conference on Mathematics and Computation, Supercomputing in Nuclear Applications and the Monte Carlo Method 2015, April 19–23, 2015, Nashville, TN, U.S.A. (2015).

Krawczyk-Bärsch, E.
The influence of microorganisms on the immobilization of radionuclide in subsurface crystalline rock environments
Teaching module: Interactions of heavy metals with bacteria for bioremediation purposes, June 16, 2015, Granada, Spain (2015).

Krawczyk-Bärsch, E.; Gerber, U.; Steudtner, R.; Arnold, T.
Use of spectroscopic and microscopic methods to reveal the evidence of U(VI) sorption on *Acidovorax facilis* isolated from subsurface environments
Environmental Radioactivity 2015 Conference, September 21–25, 2015, Thessaloniki, Greece (2015).

Krawczyk-Bärsch, E.; Gerber, U.; Steudtner, R.; Lünsdorf, H.; Arnold, T.
Evidence of U(VI) sorption on *Acidovorax facilis* by TRLFS and EF-TEM/EELS
Goldschmidt 2015, August 16–21, 2015, Prague, Czech Republic (2015).

Kulenkampff, J.
Spatiotemporal monitoring of geochemical transport processes with Positron Emission Tomography (PET) – a useful tool for CEBAMA partners
IGD-TP 6th Exchange Forum, November 03–04, 2015, London, U.K. (2015).

Kulenkampff, J.; Gründig, M.; Zakhnini, A.; Schikora, J.; Gerasch, R.; Lippmann-Pipke, J.
Visualization of Heterogeneous Diffusion Processes with PET aligned with 3D FE simulation results
7th International Symposium on Process Tomography, September 01–03, 2015, Dresden, Germany (2015).

Lozano-Rodriguez, M. J.; Arinicheva, Y.; Holthausen, J.; Neumeier, S.; Scheinost, A. C.
Structural stability study of the mixed $La_{0.7-x}Lu_xEu_{0.3}PO_4$ solid solutions by Extended X-ray Absorption Spectroscopy
Scientific Basis for Nuclear Waste Management XXXIX, November 02–06, 2015, Montpellier, France (2015).

Lozano-Rodriguez, M. J.; Arinicheva, Y.; Heuser, J.; Kvashnina, K.; Neumeier, S.; Scheinost, A. C.
Determination of local structure in mixed lanthanoid phosphate solid solutions by X-ray absorption spectroscopy
E-MRS Spring Meeting 2015, May 11–15, 2015, Lille, France (2015).

Martin, P. M.; Bes, R.; Prieur, D.; Vathonne, E.;
Carlot, G.; Delorme, R.; Sabathier, C.;
Freyss, M.; Garcia, P.; Bertolus, M.;
Lebreton, F.; Caisso, M.; Delahaye, T.;
Strach, M.; Belin, R.; Martel, L.; Vigier, J. F.;
Somers, J.; Prussmanns, T.; Vitova, T.;
Rothe, J.; Dardenne, K.; Solari, P. L.;
Kvashnina, K.; Glatzel, P.; Scheinost, A. C.;
Proux, O.
Application of HERFD and in-situ XAS to study oxide nuclear fuel and fission product behavior
XAFS16 – 16th International Conference on X-ray Absorption Fine Structure, August 23–28, 2015, Karlsruhe, Germany (2015).

Merk, B.
On the use of a molten salt fast reactor for transmutation fulfilling the requests of the nuclear phase out decision
Annual Meeting on Nuclear Technology, May 05–07, 2015, Berlin, Germany (2015).

Merk, B.; Geist, A.; Modolo, G.; Knebel, J.
Results and conclusions from the German P&T study – a view of the contributing Helmholtz research centres
Annual Meeting on Nuclear Technology, May 05–07, 2015, Berlin, Germany (2015).

Moors, H.; Cherkouk, A.; Mysara, M.; Bleyen, N.;
Smets, S.; Schwyn, B.; Albrecht, A.;
Wittebroodt, C.; Small, J.; de Cannière, P.;
Stroes-Gascoyne, S.; Valcke, E.; Leys, N.
The Bitumen-Nitrate-Clay Interaction Experiment at the Mont Terri Rock Laboratory, Switzerland: Response of Microbial Communities to Additions of Nitrate and Acetate
Clays in natural and engineered barriers for radioactive waste confinement, March 23–26, 2015, Bruessels, Belgium (2015).

Müller, K.; Steudtner, R.; Huittinen, N.; Bok, F.;
Rossberg, A.
Spectroscopic identification of Np(V) sorption complexes at the mineral oxide-water interface
Goldschmidt 2015, August 16–21, 2015, Prague, Czech Republic (2015).

Neumeier, S.; Arinicheva, Y.; Huittinen, N.;
Lozano-Rodriguez, M. J.; Holthausen, J.;
Modolo, G.; Scheinost, A. C.; Stumpf, T.;
Bosbach, D.
Spectroscopic studies on monazite-type ceramics for the conditioning of radioactive waste: Infrared, Raman, X-ray Absorption and Site-Selective Time Resolved Laser Fluorescence Spectroscopy
E-MRS Spring Meeting 2015, May 11–15, 2015, Lille, France (2015).

Prieur, D.; Martin, P.; Bes, R.; Lebreton, F.;
Caisso, M.; Delahaye, T.; Strach, M.; Belin, R.;
Martel, L.; Vigier, J. F.; Prussmann, T.;
Vitova, T.; Solari, P.; Kvashnina, K.;
Scheinost, A. C.; Somers, J.
Electronic and structural changes induced by the incorporation of aliovalent cation in UO₂
XAFS16 – 16th International Conference on X-ray Absorption Fine Structure, August 23–28, 2015, Karlsruhe, Germany (2015).

Raff, J.; Günther, A.; Moll, H.; Vogel, M.;
Drobot, B.; Stumpf, T.
Wechselwirkung von Radiometallen mit biologischen Systemen
GDCh-Wissenschaftsforum Chemie 2015 – Chemie verbindet, August 30–September 02, 2015, Dresden, Germany (2015)

Raff, J.; Günther, A.; Moll, H.; Vogel, M.; Suhr, M.;
Drobot, B.; Li, B.; Foerstendorf, H.; Stumpf, T.
Interaction of radionuclides with the biosphere
Institute seminar School of Chemistry, University of Manchester, October 26, 2015, Manchester, U. K. (2015).

Raff, J.; Günther, T.; Weinert, U.; Vogel, M.;
Suhr, M.; Matys, S.; Drobot, B.; Pollmann, K.
Using nature's genius for the functionalization of surfaces
Euro BioMAT 2015, April 21–22, 2015, Weimar, Germany (2015).

Raff, J.; Weinert, U.; Matys, S.; Vogel, M.;
Suhr, M.; Günther, T.; Drobot, B.; Lehmann, F.;
Kutschke, S.; Pollmann, K.
How radio-ecological research helps to develop innovative nanobiomaterials
Arbeitskreisseminar Technische Chemie, July 03, 2015, Paderborn, Germany (2015).

Raff, J.; Weinert, U.; Matys, S.; Vogel, M.;
Suhr, M.; Günther, T.; Hofinger, J.; Drobot, B.;
Lehmann, F.; Kutschke, S.; Pollmann, K.
Specific binding biomolecules
Professur-Seminar Biomaterialien, July 01, 2015, Dresden, Germany (2015).

Reichenbach, P.; Kämpfe, T.; Haußmann, A.; Steudtner, R.; Woike, T.; Eng, L. M.
Multiphoton-induced luminescence and its domain contrast in Mg-doped LiNbO₃ and LiTaO₃
DPG Frühjahrstagung, March 15–20, 2015, Berlin, Germany (2015).

Richter, C.
Influence of calcium onto the sorption of uranium(VI) in the far-field of nuclear waste repositories
Petrus PhD Conference 2015, June 22–26, 2015, Nancy, France (2015).

Richter, C.
Sorption of environmentally relevant radionuclides (U(VI), Np(V)) and lanthanides (Nd(III)) on feldspar and mica
Kompetenzzentrum Ost für Kerntechnik (KOMPOST) 10. Doktorandenseminar, December 08, 2015, Dresden, Germany (2015).

Richter, C.
Sorption of environmentally relevant radionuclides (UO_2^{2+}, NpO_2^+) and lanthanides (Nd^{3+}) on feldspar and mica
Abteilungsseminar der Abteilung Hydrogeochemie und Hydrogeologie, Institut für Geowissenschaften, Universität Heidelberg, December 03, 2015, Heidelberg, Germany (2015).

Sallat, M.; Schwarzmann, Y.; Weinert, U.; Günther, T.; Raff, J.
Proteins as new components for funktionalizing textile surfaces
Aachen-Dresden International Textile Conference, November 26–27, 2015, Aachen, Germany (2015).

Schmeide, K.; Fritsch, K.; Lippold, H.; Poetsch, M.; Kulenkampff, J.; Jordan, N.; Moll, H.; Cherkouk, A.
Wechselwirkung von Actiniden/Lanthaniden mit Ton, Tonorganika und Mikroorganismen
Abschlussworkshop des Verbundprojekts "Rückhaltung endlagerrelevanter Radionuklide im natürlichen Tongestein und in salinaren Systemen", May 12–13, 2015, Mainz, Germany (2015).

Schymura, S.; Hildebrand, H.; Fricke, T.; Holzwarth, U.; Bellido, E.; Ojea-Jiménez, I.; Cydzik, I.; Kulenkampff, J.; Kozempel, J.; Dalmiglio, M.; Bulgheroni, A.; Cotogno, G.; Simonelli, F.; Gibson, N.; Franke, K.; Lippmann-Pipke, J.
Radiolabelling – A versatile tool for tracking nanoparticle release, uptake and transport
10th International Conference on the Environmental Effects of Nanoparticles and Nanomaterials, September 06–10, 2015, Wien, Austria (2015).

Steudtner, R.; Hübner, R.; Müller, K.; Weiss, S.; Scheinost, A. C.
Neptunium Redox Reactions at the Iron Mineral – Water Interface
Goldschmidt 2015, August 16–21, 2015, Prague, Czech Republic (2015).

Stockmann, M.; Brendler, V.; Schikora, J.; Flügge, J.; Noseck, U.
A new methodology for utilizing multidimensional smart K_d-matrices in transport programs for long-term safety assessment
Migration 2015 – 15th International Conference on the Chemistry and Migration Behaviour of Actinides and Fission Products in the Geosphere, September 13–18, 2015, Santa Fe, U.S.A. (2015).

Tits, J.; Rojo, H.; Scheinost, A. C.; Lothenbach, B.; Wieland, E.
Selenium uptake by cementitious materials: Effect of the redox state
Migration 2015 – 15th International Conference on the Chemistry and Migration Behaviour of Actinides and Fission Products in the Geosphere, September 13–18, 2015, Santa Fe, U.S.A. (2015).

Tsushima, S.
Exploring photochemistry of uranyl(VI)
The International Chemical Congress of Pacific Basin Societies (PACIFICHEM 2015), Symposium on Experimental and Theoretical Actinide Chemistry: From Fundamental Systems to Practical Applications, December 15–20, 2015, Honolulu, Hawaii, U.S.A. (2015).

Tsushima, S.
Uranium interaction with DNA and protein
Workshop on Fragment Molecular Orbital Method (FMO) Application to Actinide Research, December 10–11, 2015, Ochanomizu University, Tokyo, Japan (2015).

Tusheva, P.; Schäfer, F.; Altstadt, E.; Kliem, S.
Severe accident management research at HZDR
1ˢᵗ Sino-German Symposium on Fundamentals of Advanced Nuclear Safety Technology, March 09–12, 2015, Shanghai, China (2015).

Tusheva, P.; Schäfer, F.; Kozmenkov, Y.; Kliem, S.; Hollands, T.; Trometer, A.; Buck, M.
WASA-BOSS: ATHLET-CD model for severe accident analysis for a generic KONVOI reactor
Jahrestagung Kerntechnik/Annual Meeting on Nuclear Technology, May 05–07, 2015, Berlin, Germany (2015).

Wieland, E.; Rojo, H.; Scheinost, A. C.; Lothenbach, B.; Tits, J.
Redox transformations and the disposal of radioactive waste: Influence on Se immobilization
Goldschmidt 2015, August 16–21, 2015, Prague, Czech Republic (2015).

Wilke, C.; Barkleit, A.; Stumpf, T.
Spectroscopic investigation of the complexation of trivalent actinides/lanthanides in body fluids
Workshop zum Verbund "Transfer von Radionukliden in aquatischen Ökosystemen", April 20–21, 2015, Bremen, Germany (2015).

In addition, more than 30 posters were presented at international conferences and workshops.

⭘ Theses

Doctoral Theses

Abu Sharkh, S. E.
Spectroscopic & thermodynamic investigations of the physical basis of anhydrobiosis in *caenorhabditis elegans dauer larvae*
Technische Universität Dresden, Dresden, Germany (2015).

Dulnee, S.
Sorption and interfacial reaction of Sn^{II} onto magnetite ($Fe^{II}Fe^{III}_2O_4$), goethite (α-$Fe^{III}OOH$), and mackinawite ($Fe^{II}S$)
Technische Universität Dresden, Dresden, Germany (2015).

Fischermeier, E.
Protein–Lipid interactions and the functional role of intra-membrane protein hydration in the PIB-type ATPase CopA from *Legionella pneumophila*
Technische Universität Dresden, Dresden, Germany (2015).

Gagell, C.
Dynamik der zeitlichen Veränderung der mikrobiellen Diversität in gefluteten Uranbergwerken und deren Auswirkungen auf die Uranimmobilisierung
Technische Universität Dresden, Dresden, Germany (2015).

Günther, T.
S-Layer als Technologieplattform – Selbstorganisierende Proteine zur Herstellung funktionaler Beschichtungen
Technische Universität Dresden, Dresden, Germany (2015).

Hofmann, S.
Der Einfluss endlagerrelvanter Elektrolyte auf die Wechselwirkung dreiwertiger Lanthanide und Actinide mit Calcit
KIT, Karlsruhe, Germany (2015).

Husar, R.
Investigation into the formation of nanoparticles of tetravalent neptunium in slightly alkaline aqueous solution
Technische Universität Dresden, Dresden, Germany (2015).

Rachamin, R.
Conceptual design of pressure tube light water reactor with variable moderator control
Ben-Gurion-University, Beer-Sheva, Israel (2015).

Sabau, A.
Interaction mechanisms of europium and nickel with calcite
University Nice Sophia Antipolis, Nice, France (2015).

Sayed, A. M. T.
  Spectroscopic investigation of conformational transitions in the copper-transporting P1B-ATPase CopA from *Legionella pneumophila*
  Technische Universität Dresden, Dresden, Germany (2015).

Suhr, M.
  Isolierung und Charakterisierung von Zellwandkomponenten der gram-positiven Bakterienstämme *Lysinibacillus sphaericus* JG-A12 und JG-B53 und deren Wechselwirkungen mit ausgewählten relevanten Metallen und Metalloiden
  Technische Universität Dresden, Dresden, Germany (2015).

Zirnstein, I.
  Charakterisierung der Mikroorganismen im sauren Grubenwasser des ehemaligen Uranbergwerks Königstein
  Technische Universität Dresden, Dresden, Germany (2015).

DIPLOMA THESES

Luthard, P.
  Untersuchungen zur Wechselwirkung ausgewählter Bakterien mit Selen-Oxyanionen
  Technische Universität Dresden, Dresden, Germany (2015).

MASTER THESES

Gerasch, R.
  Simulation und Parameterschätzung von ^{22}Na-Diffusion in einem Opalinuston-Bohrkern mittels COMSOL Multiphysics und GeoPET-Datenabgleich
  Brandenburg University of Technology, Cottbus-Senftenberg, Germany (2015).

BACHELOR THESES

Hildebrand, P.
  Urantolerante Pflanzen – Wechselwirkung mit Exsudaten und Nährmedien
  Brandenburg University of Technology, Cottbus-Senftenberg, Germany (2015).

Spranger, F.
  Immobilisierung von Tc(VII)/Tc(IV) an Eisenphasen
  Technische Universität Dresden, Dresden, Germany (2015).

.

○ SEMINARS (TALKS OF VISITORS)

○ WORKSHOPS & SESSIONS

○ APPOINTMENT

○ AWARDS

○ TEACHING ACTIVITIES

○ FURTHER EVENTS

○ Seminars

Itävaara, Merja
VTT Technical Research Centre of Finland, Espoo, Finland
From deep biosphere to geological disposal of nuclear wastes – Finnish microbiology research of Fennoscandian shield
February 05, 2015

Vikman, Minna
VTT Technical Research Centre of Finland, Espoo, Finland
Biodegradation of low level radioactive waste in final disposal
February 05, 2015

Montavon, Gilles
Subatech, Nantes, France
Research activities of the radiochemistry group at SUBATECH
February 25, 2015

Chapon, Virginie
CEA Cadarache, Institut de Biologie Environnementale et Biotechnologie (iBEB), St. Paul-lez-Durance, France
Microorganisms of radionuclides-contaminated soils of Chernobyl: in depth analysis of diversity and study of uranium-bacteria interactions
March 03, 2015

Den Auwer, Christophe
Université de Nice Sophia Antipolis, Department de chimie, France
Chemical mechanisms in human nuclear toxicology, the use of combined spectroscopies
April 01, 2015

Rowland, Darren
JESS database, Murdoch University, Australia
Lessons learned from large-scale Pitzer parameter optimizations
April 08, 2015

Swanson, Julie
Los Alamos National Laboratory, Carlsbad Operations, U.S.A.
Influence of microorganisms on salt-based nuclear waste repositories: the waste isolation pilot plant
April 17, 2015

Hesemann, Peter
Institut Charles Gerhardt, Montpellier, France
Ionosilicas for anion exchange reactions
May 11, 2015

Schlömann, Michael
TU Bergakademie Freiberg, Institut für Biowissenschaft, Germany
Aktivitäten der Umweltmikrobiologie in Freiberg rund um mikrobielle Laugung und Behandlung von Bergbauwässern
July 03, 2015

Brulfert, Florian
Insitut de Physique Nucléaire d Orsay Université Paris-Sud, France
Interaction mechanisms between actinides and a protein: the calmodulin
July 15, 2015

Morris, Katherine
University of Manchester, United Kingdom
Radionuclide speciation and fate in environmental systems – why do we need to know?
August 25, 2015

Spijker, Peter
Aalto University Helsinki, Finland
Interactions at the solid-liquid interface from a molecular simulation perspective
September 03, 2015

Leigh, Christi
Sandia National Laboratories, Carlsbad, U.S.A.
The geochemical model for the waste isolation pilot plant (WIPP)
September 10, 2015

Bruno Salgot, Jordi
CEO Amphos 21 Group, Spain
Scientific challenges in the nuclear cycle
October 14, 2015

Payne, Timothy E.
Australian Nuclear Science and Technology Organisation (ANSTO), Australia
Migration mechanisms of plutonium, other actinides and fission products at a legacy trench disposal site
November 05, 2015

Walter, Olaf & Magnani, Nicola
Institute for Transuranium Elements, Karlsruhe, Germany
Synthesis and characterisation of actinide complexes: actual research at the ITU (O.W.)

Magnetic properties of selected actinide complexes (N.M.)
November 25, 2015

⭘ WORKSHOPS & SESSIONS; (CO)-ORGANIZED BY THE IRE

Trilateral meeting

Institute for Nuclear Waste Disposal (INE) *KIT, Karlsruhe*	Institute of Resource Ecology (IRE) *HZDR, Dresden*	Institute of Energy and Climate Research (IEK-6) *FZJ, Jülich*

FZ Jülich, Jülich, Germany, March 04–05, 2015.

Bok, F.
Databases & Surface complexation modelling at HZDR/IRE

Deißmann, G.
Research activities in reactive transport modelling at FZJ/IEK-6

Heberling, F.
Radionuclide retention by secondary phases: from fundamental studies towards reactive transport modelling

Kowalski, P.
An overview of atomistic modelling activities at IEK-6

Lippmann-Pipke, J.
Enhanced reactive transport process understanding by means of experiments and modelling at HZDR/IRE

Montoya, V.
Application of reactive transport modelling to laboratory scale experiments

Patzschke, M.
Planned Projects of the New Theory Group in Rossendorf

Trumm, M.
Computational actinide chemistry at INE: An overview

Weber, J.
Ra retention by uptake into barite – nanoanalytical characterization of the $(Ba,Ra)SO_4$ solid solution by APT and TEM

Goldschmidt 2015 – Sessions coorganized by IRE

Prague, Czech Republic, August 16–21, 2015.

Scheinost, A. C.; Zavarin, M.; Morris, K.; Marques Fernandes, M.
Session 13e:
Biogeochemical Redox Processes and Radiocontaminants

Catalano, J.; Boily, J.-F.; Stack, A.; Müller, K.
Session 15a:
Structure, Dynamics, and Reactivity of Mineral-Water and Mineral-Gas Interfaces

Bilateral meeting

| Nuclear Energy and Safety Research Department, Laboratory for Waste Management (LES)
PSI, Villigen, Switzerland | Institute of Resource Ecology (IRE)
HZDR, Dresden, Germany |

HZDR, Dresden, Germany, August 27–28, 2015.

Bok, F.
Databases & Modelling: Surfaces & Brines

Churakov, S.
Status of the Swiss waste disposal program and the LES contribution

Fahmy, K.
Perspectives of X-FEL-based Structural Biology for metal-binding proteins

Gimmi, T.
Experimental study of cement-clay interaction

Hildebrand, H.
Ausbau einer Deutsch-Tschechischen Kooperation auf dem Gebiet der Nuklearen Endlagerforschung (NuWaMa)

Kaden, P.
NMR spectroscopy at HZDR-IRE

Patzschke, M.
How theory can probe the chemical bond: The case of caged U_2

Prasianakis, N.
Multi-Scale Reactive Transport Modelling at LES

Schmeide, K.
Einfluss hoher Salinitäten auf die U(VI)-Sorption an Montmorillonit und zukünftige Forschung im Projekt "Geochemische Radionuklidrückhaltung an Zementalterationsphasen (GRaZ)"

Steudtner, R.
Neptunium Reactions at the Iron Mineral – Water Interface

Stumpf, T.
Remarks about future plans at the Institute of Resource Ecology

Thoenen, T.
Temperaturextrapolation mit isocoulombischen Reaktionen

Wieland, E.
C-14 release during anoxic corrosion of activated steel: Status of LES research

Bilateral meeting

| Working Group Lüttge
MARUM/University of Bremen, Germany | Institute of Resource Ecology (IRE)
HZDR, Dresden, Germany |

HZDR, Dresden, Germany, September 10, 2015.

Arvidson, R. S.
Cement Hydration Kinetiks – in situ, real time and KMC studies

Bok, F.
Databases & modelling: Surfaces & brines

Fischer, C.
Prediction of Porosity in Polycrystalline Material: A KMC Study using the Rate SpectraConcept

Foerstendorf, H.
Mineral surface species of dissolved actinides and fission products probed by vibrational spectroscopy

Huittinen, N.
Eu(III) and Cm(III) incorporation in ceramic materials for conditioning of radioactive wastes

Lüttge, A.
Probleme gekoppelter Reaktionskinetik – Auflösungs-Kristallisationsprozesse

Moll, H.
U(VI), Cm(III), and Eu(III) interaction studies with a typical bacterial isolate from Mont Terri Opalinus Clay

Scheinost, A. C.
Molecular redox processes of fission products with steel-corrosion and cement minerals

⭘ Appointment

Merk, B.
Chair "Computational Modelling for Nuclear Engineering"
National Nuclear Laboratory and Royal Academy of Engineering, University of Liverpool, Liverpool, U.K.

⭘ Awards

Best Paper

Tusheva, P.; Schäfer, F.; Kozmenkov, Y.; Kliem, S.; Hollands, T.; Trometer, A.; Buck, M.
WASA-BOSS: ATHLET-CD model for severe accident analysis for a generic KONVOI reactor
Annual Meeting on Nuclear Technology, May 05–07, 2015, Berlin, Germany (2015).

Poster Awards

Wilke, C.
Spectroscopic investigation of the complexation of trivalent actinides/lanthanides in body fluids
GDCh-Wissenschaftsforum Chemie 2015 – Chemie verbindet, August 30–September 02, 2015, Dresden, Germany (2015).

Drobot, B.
Analysis of mononuclear uranyl(VI) hydroxo complexes using TRLFS and PARAFAC
GDCh-Wissenschaftsforum Chemie 2015 – Chemie verbindet, August 30–September 02, 2015, Dresden, Germany (2015).

◯ TEACHING ACTIVITIES

(Winter term: WT; Summer term: ST)

Lectures

Bilodid, Y.
> *University of Cambridge , ST 2015*
> **Nodal methods in reactor simulations**

Brendler, V.; Huittinen, N.
> *Dresden University of Applied Sciences, ST 2015*
> **Radiochemie**

Fahmy, K.
> *Technische Universität Dresden, WT 2014/15*
> **Optical and vibrational spectroscopy**
> *BIOTEC-Master-Course,*
>
> *ST 2015*
> **Biophysical methods**
> **Biological thermodynamics**

Franzen, C.
> *Technische Universität Dresden, ST 2015*
> **Environmental chemistry**

Lippold, H.
> *Leipzig University, ST 2015*
> **Radiochemistry and radiopharmacology –**
> **Part II: origin, properties and applications of**
> **ionising radiation**
>
> **Radioanalytics**

Raff, J.
> *Dresden University of Applied Sciences, WT 2014/15, WT 2015/16*
> **Mikrobiologie**
>
> *Technische Universität Dresden, WT 2015/16*
> **Mikrobielle Laugung**

Schmidt, M.
> *Technische Universität Dresden, WT 2015/16*
> **Chemistry of f-elements**

Stumpf, T.
> *Technische Universität Dresden, ST 2015*
> **Radiochemistry**

Courses

♻ The laboratory course "Radiochemistry" was provided from August 31th to September 4th and from September 7th to 11th, 2015, as a part of a module of the chemistry master degree program at the Technische Universität Dresden.

Advisers:

Barthen, R.	Hellebrandt, S.	Lehmann, S.
Bauer, A.	Hellebrandt, S.E.	Dr. Patzschke, M.
Franze, M.	Dr. Huittinen, N.	Dr. Schmidt, M.
Gerber, U.	Dr. Kaden, P.	Weiss, S.
Hopfe, S.	Kostudis, S.	

♻ The IRE provided two experiments "Alpha spectrometric isotope dilution analysis of uranium" and "Technetium in Nuclear Medicine" (WT 2014/15 only) of the laboratory course "Instrumental Analysis" held by the Institute for Analytical Chemistry, Technische Universität Dresden.

Advisers:

WT 2014/15		WT 2015/16
Barthen, R.	Dr. Hofmann, S.*	Bader, M.
Drobot, B.	Richter, C.	Bauer, A.
Dr. Franzen, C.	Taube, F.§	Brinkmann, H.
Hellebrandt, S.	Weiss, S.	Franze, M.
Hellebrandt, S.E.	Wilke, C.	Weiss, S.

*: Karlsruhe Institute of Technology;
§: Technische Universität Dresden

♻ Biophysics course of the Dresden-International-Graduate School.

Advisers:

WT 2014/15 & WT 2015/16	
Prof. Dr. Fahmy, K.	Philipp, J.
Dr. Oertel, J.	Sayed, A. (WT 2014/15)

♻ Reactor simulations with DYN3D course at the University of Cambridge, WT 2014/15, advised by Dr Y. Bilodid.

⭘ Further Events

A Flock of Happenings by Florian Dombois

Dresden, May 30th, 2015

TURNING TIME BACK INTO THE FUTURE. In early 2015, a 'Flock of Happenings' was initiated by the artist Florian Dombois who invited scientific institutions in Dresden to participate in performances for the public. His special interest was the phenomena of backward running time. Scientists from the Institute of Resource Ecology related to this theme by considering the disposal of radioactive waste. Suitable repositories have to protect the biosphere from these substances for one million years. To materialize such an enormous period of time, the scientists and the artist developed a 'time rope'. At the Postplatz in the inner city of Dresden, one million years were initially projected into the past on a 200 meter long rope on the basis of historical events; then into the future via notional points in time and the decay rate of radioactive isotopes. In this way, the rope stretches right back to the beginnings of human life and simultaneously points out how long radioactive waste will need to decay to a natural level.

Link: https://www.researchcatalogue.net/view/133556/145408

Fotos by: Kristina Berndt, Florian Dombois, Alena Drahokoupilová, Thomas Eller, Konrad Kästner, Sophia Mix, Jonas Müller, Steffen Werner.

Excursion – The Konrad mine

Salzgitter, June 23rd, 2015

The Konrad mine, an abandoned iron ore mine located in the area of the city of Salzgitter is currently being converted to a repository for radioactive waste with negligible heat generation.

Fotos by: Ronny Berndt.

Summer party

HZDR, July, 2nd, 2015

Fotos by: Evelyn Krawczyk-Bärsch, Anke Richter.

Seminar of the PhD students

Scheffau, Austria, September 20–26, 2015

Young scientists of the IRE met in conclave in the Austrian Alps for a week.

Fotos by: Björn Drobot, Juliane März.

Miscellaneous (Fotos by: Jana Grämer, Evelyn Krawczyk-Bärsch, Anke Richter, Mathias Suhr)

Bike excursion
(Dresden surroundings, July 16th, 2015).

REWE-Team race.
(Dresden, June 3rd, 2015).

Amateur athletes and members of HZDR and HIF at the Dragon boat competition on the ELBE river (Dresden, June 27th, 2015).

Skiing week (Austrian Alps, March, 2015).

Institute of Resource Ecology

HZDR e.V.

- Biogeochemistry
- Biophysics
- Chemistry of the f-Elements
- Molecular Structures
- Reactive Transport
- Reactor Safety
- Surface Processes
- Radiation Protection Techniques
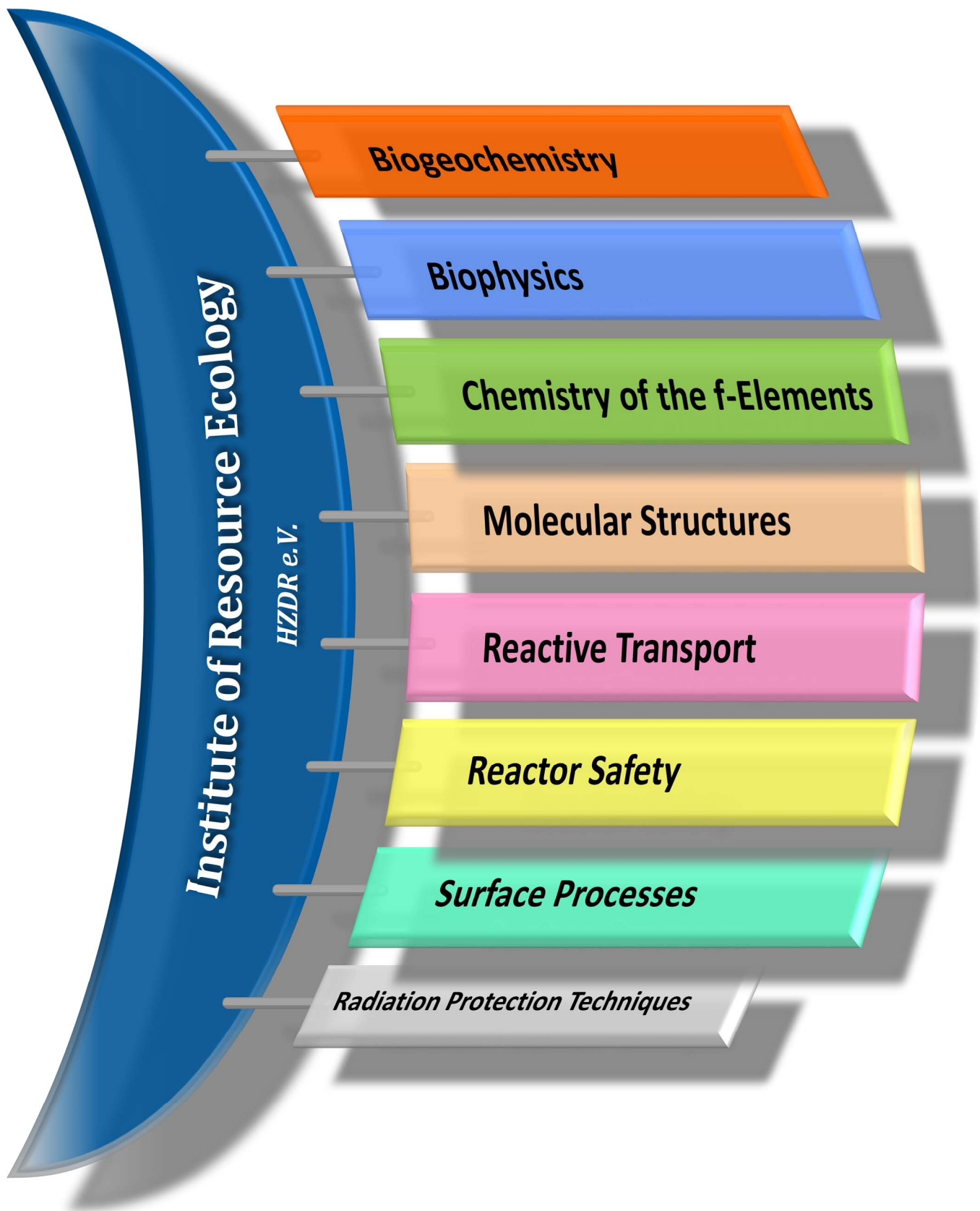
Prof. Dr. Thorsten Stumpf
(HEAD OF INSTITUTE)

ADMINISTRATION:
Office Dresden: Gorzitze, Jana; Kovacs, Jenny;
Kurde, Kerstin; Lauke, Regina
Office ESRF: Glückert, Marion
Office Leipzig: Gerstner, Katrin
Sysad: Berndt, Ronny

PROJECT COORDINATION:
Office Dresden: Dr. Arnold, Thuro

RADIATION PROTECTION:
Heim, Heidemarie; Falkenberg, Dirk; Henke, Steffen;
Nebe, Katrin; Rumpel, Annette

BIOGEOCHEMISTRY
Dr. Geipel, Gerhard

Dr. Baumann, Nils	Dr. Krawczyk-Bärsch, Evelyn
Brinkmann, Hannes	Dr. Moll, Henry
Drobot, Björn	Müller, Manuela
Dudek, Monika	Dr. Raff, Johannes
Flemming, Katrin	Ramisch, Alexander
Gerber, Ulrike	Dr. Sachs, Susanne
Dr. Günther, Alix	Seibt, Jana
Dr. Heller, Anne	Dr. Vogel, Manja
Heller, Sylvia	

HZDR Young Investigator Group
Dr. Cherkouk, Andrea
Bader, Miriam   Franze, Madlen

BIOPHYSICS
Prof. Dr. Fahmy, Karim

Fischermeier, Elisabeth	Philipp, Jenny
Obeid, Muhammad H.	Dr. Tsushima, Satoru
Dr. Oertel, Jana	

CHEMISTRY OF THE F-ELEMENTS
Dr. Ikeda-Ohno, Atsushi

Dr. Barkleit, Astrid	Dr. Patzschke, Michael
Dr. Kaden, Peter	Dr. Schmid, Matthias
Dr. März, Juliane	Wilke, Claudia

MOLECULAR STRUCTURES
Dr. habil. Scheinost, Andreas C.

Dr. Butzbach, Randolf	Dr. Kvashnina, Kristina
Dräger, Eric	Dr. Lozano Rodriguez, Janeth
Exner, Jörg	Dr. Rossberg, André
Dr. Hennig, Christoph	

REACTIVE TRANSPORT
Dr. Lippmann-Pipke, Johanna

Barthen, Robert	Dr. Kulenkampff, Johannes
Becker, Michael	Dr. Lippold, Holger
Dr. Eichelbaum, Sebastian	Lösel, Dagmar
Dr. Franke, Karsten	Dr. Mansel, Alexander
Gründig, Marion	Poetsch, Maria
Gruhne, Stefan	Schößler, Claudia
Dr. Hildebrand, Heike	Dr. Schymura, Stefan
Dr. Karimzadeh, Lotfallah	

REACTOR SAFETY
Dr. Kliem, Sören

Dr. Baier, Silvio	Litskevich, Dzianis
Dr. Bilodid, Yurii	Dr. Merk, Bruno
Dr. Fridman, Emil	Dr. Müller, Stefan
Gommlich, André	Nikitin, Evgeny
Dr. Grahn, Alexander	Rachamin, Reuven
Hoffmann, Alexander	Sporn, Michael
Jobst, Matthias	Dr. Schäfer, Frank
Konheiser, Jörg	Dr. Wilhelm, Polina
Kozmenkov, Yaroslav	

SURFACE PROCESSES
Dr. Brendler, Vinzenz

Bauer, Anne	Lehmann, Susanne
Dr. Bok, Frank	Müller, Christa
Eckardt, Carola	Dr. Müller, Katharina
Fischer, Sarah	Neubert, Heidrun
Dr. Foerstendorf, Harald	Philipp, Thimo
Dr. Franzen, Carola	Dr. Richter, Anke
Fritsch, Katharina	Richter, Constanze
Dr. Großmann, Kay	Ritter, Aline
Gürtler, Sylvia	Dr. Schmeide, Katja
Gurlit, Sabrina	Schubert, Stefanie
Heim, Karsten	Dr. Steudtner, Robin
Dr. Huittinen, Nina	Dr. Stockmann, Madlen
Dr. Jordan, Norbert	Weiss, Stephan
Kappler, Ina	Wolter, Jan-Martin
Kretzschmar, Jérôme	

HGF Young Investigator Group
Dr. Schmidt, Moritz
Hellebrandt, Sophia   Hofmann, Sascha
Hellebrandt, Stefan   Dr. Johnstone, Erik

GUEST SCIENTISTS

Bernhard, Gert	*Radiochemie, Technische Universität Dresden,* *Dresden, Germany*
Bilodid, Ievgen	*Scientific-technical Centre for Nuclear and Radiation Safety of the Ukraine,* *Kiew, Ukraine*
Brulfert, Florian	*Université Paris Sud, Institut de Physique Nucléaire,* *Orsay, France*
Comarmond, Josick	*Institute for Environmental Research,* *Australian Nuclear Science and Technology Organisation, Menai, Australia*
Chotkowski, Maciej	*Faculty of Chemistry, University of Warsaw,* *Warsaw, Poland*
Fricke, Thomas	*Vita 34 AG,* *Leipzig, Germany*
Jain, Rohan	*UNESCO-IHE, Institute for Water Education,* *Delft, The Netherlands*
Martin, Nicolas	*Unité de Catalyse et Chimie du Solide, Université de Lille,* *Lille, France*
Mayordomo Herranz, Natalia	*Centro de Investigaciones Energéticas, Medioambientales y Tecnológicas,* *Madrid, Spain*
Navitskaya, Roza	*Belarusian State University,* *Minsk, Belarus*
Elo, Outi	*Laboratory of Radiochemistry, University of Helsinki,* *Helsinki, Finland*
Ovdiienko, Iurii	*Scientific-technical Centre for Nuclear and Radiation Safety of the Ukraine,* *Kiew, Ukraine*
Shrestha, Rojina	*Technical University Liberec,* *Liberec, Czech Republic*
Virtanen, Sinikka	*Laboratory of Radiochemistry, University of Helsinki,* *Helsinki, Finland*
Volkringer, Christoph	*Unité de Catalyse et Chimie du Solide, Université de Lille,* *Lille, France*
Wilden, Andreas	*Forschungszentrum Jülich* *Jülich, Germany*
Wu, Shijun	*Guangzhou Institute of Geochemistry, Chinese Academy of Sciences,* *Guangzhou, China*

MASTER/DIPLOMA/BACHELOR

Gerasch, Robert	Lehrich, Jana	Röder, Grit	
Haubitz, Toni	Luthard, Paula	Spranger, Felix	Wollenberg, Anne

GRADUATE ASSISTANTS, STUDENT ASSISTANTS, TRAINEES

Bauditz, Maria	Junghans, Hannes	Schöne, Sebastian	Wolke, Florian
Eibl, Manuel	Kermes, Sissi	Plytyn, Maximilian	Zakhnini, Abdelhamid
Gabernet Garriga, Gisela	Lösch, Henry	Radoske, Thomas	Zechel, Susanne
John, Fabian	Nucke, Lisa	Wendisch, Marc	

FUNDING ORGANIZATION / COMPANY	PROJECT TITLE	CONTRACT NO. (if applicable)
	Verbundprojekt: Rückhaltung endlagerrelevanter Radionuklide im natürlichen Tongestein und in salinaren Systemen – Geochemisches Verhalten und Transport von Radionukliden (Np, U, Pu und weitere RN) in salinaren Systemen in Gegenwart endlagerrelevanter Organika	02E10971
	ThermAc – Verbundprojekt: Aufklärung von Thermodynamik und Speziation von Actiniden bei höheren Temperaturen in Kombination von Schätzmethoden, spektroskopischen und quantenmechanischen Methoden, Teilprojekt B	02NUK039B
	TransAqua – Teil A: Untersuchungen zu den Wechselwirkungen zwischen unter Tage lebenden Mikroorganismen mit Uran Teil B: Spektroskopische Bestimmung der Bindungsform (Speziation) trivalenter Actinide/Lanthanide in Biofluiden des menschlichen Gastrointestinaltraktes und im Blut	02NUK030F
	UMB – Verbundprojekt: Umwandlungsmechanismen in Bentonitbarrieren, Teilprojekt B	02E11344B
	WASA-BOSS – Verbundprojekt: Weiterentwicklung und Anwendung von Severe Accident Codes - Bewertung und Optimierung von Störfallmaßnahmen	02NUK028B
	WEIMAR – Weiterentwicklung des Smart K_d-Konzepts für Langzeitsicherheitsanalysen	02 E 11072B
	WTZ Russland – Transientenanalysen für schnelle Reaktoren	1501462
Deutsche Forschungsgemeinschaft (DFG)	Transport von CNP	FR 1643/3-1
Gesellschaft für Chemische Technik und Biotechnologie e.V. (DECHEMA)	Cryo-Fluoreszenzspektroskopie	3342
Gesellschaft für Anlagen- und Reaktorsicherheit gGmbH (GRS)	THEREDA III	
Helmholtz-Gemeinschaft Deutscher Forschungszentren e.V. (HGF)	HGF-Nachwuchsgruppe Dr. Schmidt	VH-NG-942
AREVA	Experimente PKL3	
E.ON Energie Deutschland GmbH	MCNP Rechnungen für einen DWR	
	Datensatzerstellung für DWR-Anlagen	
	Datenpflege ATHLET-Datensatz für 2013/2014	
	Potenzialstudie Nuklidabsorbierende Pilze	6021141113
Mont Terri consortium swisstopo	MA experiment – Microbiological analysis of BFE-A11 drillcores	62 2114 22 20
NRG Petten	ROCOM-PTS	
TÜV SÜD	Datenbibliotheken für WWER-1000-Reaktoren	500601247
UJV Rez, a.s.	DYN3D für UJV Wartung 2013/2014	150178
Wismut, GmbH	Spezialanalytik WISMUT II	3164929-U02/1

INDEX OF AUTHORS